Severe weather nowcasting and model evaluation using differential reflectivity

Chun Hay Brian Lo

Department of Meteorology

University of Reading

A thesis presented for the degree of

Doctor of Philosophy

February 2024

Declaration

I confirm that this is my own work and the use of all material from other sources has been properly and fully acknowledged.

Chun Hay Brian Lo

Acknowledgements

First of all, I would like to thank my main supervisors, Thorwald Stein and Chris Westbrook, for their guidance and support throughout the past few years. Completing the work and this thesis would not have been possible without the many insightful discussions in our weekly meetings, and more importantly, the much-needed reminders to take enough breaks!

I would also like to thank my supervisors at the Met Office, Timothy Darlington, Robert Scovell, and Humphrey Lean for their contributions towards more specific areas of my work making arrangements for me to spend time working at the Met Office. Special thanks to Paul Field, Kalli Furtado and Jonathan Wilkinson, who taught me the many ways of running and implementing code within the Met Office Unified Model. I am so very grateful to have such a diverse and complementary team of experts as my supervisors and collaborators.

Thank you also to members of my Monitoring Committee, Chris Holloway and Sue Gray for encouraging me to think about my research from other perspectives and providing invaluable advice on how one could navigate the world of academia.

To Caleb and Blair, my 1U09 office mates - I really appreciated our random chats (and "picasso plots"), whether that be about radars, fog or Venus' atmosphere.

To all of radar group, thanks for making Thursday afternoons the highlight of my working week. The quirky ideas exchanged in these meetings have been one of my best sources of inspiration. The provision of biscuits probably made all the difference too.

To Hannah, Izzy, Charlie, Harriet, Alanna, Natalie, Helen and others, thank you for making my time at the department so enjoyable and for sharing many memorable moments along my PhD journey.

To my sister, Karina - Thank you for bearing with my long "lectures" about meteorology trivia and always lending an ear during tough times. Finally, to my parents, Lisa and Peter - Thank you for always nurturing my curiousity about the universe, for your unwavering support to my path in pursuing scientific research, and for believing in my special interests in maths and physics when you took me to the Hong Kong Observatory at the age of seven.

Abstract

Columns of enhanced differential reflectivity (Z_{DR}) are indicative of the suspension and lofting of large raindrops and hence can be used as a proxy for intense updrafts in radar observations. The UK operational weather radars were upgraded since January 2018 to measure Z_{DR}. The Met Office has introduced a new double moment microphysics scheme. Both allow the study of Z_{DR} columns for nowcasting and forecasting, respectively. The primary aims of the thesis are to assess the potential of Z_{DR} columns in predicting severe convection within the UK and to evaluate simulated Z_{DR} columns within the UK's operational weather model.

A 3D composite of Z_{DR} is produced from the operational radar data. Evaluation against research radar data indicates that Z_{DR} columns can reliably be detected in the composite at a horizontal resolution of 1 km.

A Z_{DR} column detection algorithm for the composite is developed. Detected columns are found to precede severe convection in tracked convective cells with lead times up to 20 minutes for three case days. The variety in thresholds giving optimal performance and skill in the early detection of severe convection across case days can be explained by the presence of hail in the cell.

A polarimetric radar forward operator is constructed for the simulation of rain contribution to Z_{DR} within the Met Office Unified Model (MetUM). The implemented T-matrix scattering method accounts for non-Rayleigh scattering.

Simulated Z_{DR} within the single moment (Wilson-Ballard) and the double moment (CASIM) microphysics schemes within MetUM simulations of 300-metre grid length are evaluated with radar observations. Simulated Z_{DR} columns are wide, deep, and intense within Wilson-Ballard simulations, whereas such columns are rare in CASIM simulations, in contrast with the abundance of Z_{DR} columns in observations. Although CASIM captures well the Z_{DR}-Z_{H} relationship for rain, updrafts in simulations coupled to CASIM are considerably weaker.

List of Figures

1.1 Tephigram showing radiosonde ascent data from Herstmonceux . . . 5
1.2 Schematic model of the lifecycle of a typical thunderstorm 7
1.3 Schematic showing the operation of conventional and dual-polarisation radars 10
1.4 Vertical cross section through a convective storm 11
1.5 Development of Z_{DR} column and bounded weak echo region 14
1.6 Evolution of a simulated Z_{DR} column 15

2.1 Overview of UK Met Office C-band radar locations 20
2.2 Radar beam heights of C-band radar plan position indicator scans at various elevations 21
2.3 Vertical maximum plots from the UK 3D radar composite 22
2.4 The 25 m antenna of the Chilbolton Advanced Meteorological Radar . 25
2.5 Model domain of the 1.5 km and 300 m resolution Met Office Unified Model simulations 27
2.6 Model height against model level number 28
2.7 Joint distributions of rain drop number concentration and rain mass fraction from model simulations 36

3.1 RHI plots of Z_{H} scanned by CAMRa with corresponding azimuthally uncorrected and corrected pseudo-RHIs 40
3.2 RHI plots of Z_{DR} scanned by CAMRa with corresponding pseudo-RHIs and maximum reflectivity plan views from the radar composite 42
3.3 RHI plots of Z_{DR} scanned by CAMRa at azimuth angles tenths of degrees apart 43
3.4 Example of a regridded RHI plot of Z_{DR} scanned by CAMRa 44
3.5 Joint distributions of Z_{H} and Z_{DR} for regridded CAMRa data and composite-generated pseudo-RHI data 46
3.6 Median, 10 and 90-th percentile Z_{DR} values for each Z_{H} bin 47

4.1 Conceptual diagrams showing developmental stages of a convective cell 51
4.2 Tephigrams showing reported sounding data for three case days . . . 55

4.3 An overview of UK Met Office C-band radar locations and names . . 57
4.4 Overview of MAXDBZ over eastern England and a series of MAXDBZ showing convective storm development 60
4.5 Maximum Z_{H} and Z_{DR} plan vieew plots with vertical cross sections showing a Z_{DR} column 61
4.6 Time series of accumulated MAXDBZ pixels and accumulated Z_{DR} column detections within tracked storms 63
4.7 Box plots showing tracked storms that have met an accumulated Z_{DR} column pixel threshold and later lead to severe storm development . . 65
4.8 Verification metrics for verifying the effectiveness of Z_{DR} column appearance prior to severe convection for tracked storms 67
4.9 Maps of accumulated detections of Z_{DR} columns and hail diagnostic for three case days 70
4.10 Schematic explaining the convective cell detection algorithm 72
4.11 Example of an identified cell using the implemented cell identification algorithm 73
4.12 MAXDBZ field with Z_{DR} column detections illustrating the effect of a secondary threshold 74

5.1 Plot of sensing wavelength and particle size illustrating size parameters and scattering regimes 76
5.2 Forward modelled reflectivity Z_{H} against rain mass fraction for spherical raindrops 83
5.3 Aspect ratio against equivalent raindrop diameter for various aspect ratio models 84
5.4 Forward modelled differential reflectivity Z_{DR} against rain mass fraction for different scattering theory and aspect ratio model configurations 85
5.5 Forward modelled differential reflectivity Z_{DR} against rain mass fraction for T-matrix method with various canting angle distribution widths 86
5.6 Simulated Z_{DR} for given inputs from the CASIM microphysics scheme 87
5.7 Simulated radar reflectivity fields at 1km model height and their difference 89
5.8 Median, 10 and 90-th percentile differences of rain Z_{H} between forward operators 90
5.9 Simulated rain mass fraction, Z_{H} and Z_{DR} fields at 1km model height for domains covering 33 km × 33 km 90

6.1 Surface synoptic chart and 300 hPa vorticity fields on 01 October 2019 96
6.2 Time series of domain-averaged rainfall rate between three model simulations and radar observations 97

6.3 MAXDBZ field from the 3D radar composite and corresponding Z_{DR} column detections . . . 98
6.4 Fields of observed rainfall rates derived from the Nimrod system at various times of day . . . 99
6.5 Observed and simulated maximum reflectivity fields covering Southern England . . . 100
6.6 Joint distributions of observed and simulated Z_{H} and Z_{DR} values . . . 101
6.7 Joint distributions of observed and simulated Z_{H} and Z_{DR} values at 1 km height . . . 102
6.8 Joint distributions of observed and simulated Z_{H} and Z_{DR} values at 3 km height . . . 103
6.9 Chosen cross sections showing Z_{H} and Z_{DR} for observed and simulated convective cells . . . 105
6.10 Contour altitude by frequency diagrams of observed and simulated differential reflectivity Z_{DR} . . . 106
6.11 Plots relating terminal velocity, diameter of a raindrop and its simulated Z_{DR} . . . 108
6.12 Histograms of upward air velocities for model grid points above the freezing height . . . 108
6.13 Cumulative histograms of upward air velocities for model grid points above the freezing height . . . 109
6.14 Upward air velocity values at 99, 99.9 and 99.99-th percentiles for each model height . . . 110
6.15 Contour altitude by frequency diagrams of rain mass fraction for model grid points within columns containing updraft maximum exceeding $8\,\mathrm{m\,s^{-1}}$ . . . 112
6.16 Contour altitude by frequency diagrams of graupel mass fraction for model grid points within columns containing updraft maximum exceeding $8\,\mathrm{m\,s^{-1}}$ . . . 113

List of Tables

2.1 A table detailing model grid point numbers and extent 27

5.1 A table detailing Met Office Unified Model parameters for simulating rain reflectivity 78

List of Abbreviations

2D two-dimensional

3D three-dimensional

BWER bounded weak echo region

CAMRa Chilbolton Advanced Meteorological Radar

CAPE convective available potential energy

CASIM Cloud AeroSol Interacting Microphysics

CFAD contour frequency by altitude diagrams

CIN convective inhibition

CSI critical success index

FAR false alarm ratio

MAXDBZ maximum radar reflectivity in a column

MetUM Met Office Unified Model

NWP numerical weather prediction

POD probability of detection

PPI plan-position indicator

RHI range-height indicator

Contents

Declaration iii

Acknowledgements v

Abstract vii

List of Figures ix

List of Tables xiii

List of Abbreviations xv

Contents xvii

1 Introduction 1

1.1 Severe convective storms and updrafts . . . 3

1.1.1 What are severe convective storms? . . . 3

1.1.2 How do severe convective storms form? . . . 3

1.2 Radar observations of severe storms . . . 6

1.2.1 How do radars observe severe storms? . . . 6

1.2.2 What is dual-polarisation? How is Z_{DR} observed? . . . 9

1.2.3 What are Z_{DR} columns? . . . 10

1.3 Predicting severe convection using Z_{DR} columns . . . 13

1.3.1 Nowcasting using Z_{DR} columns . . . 13

1.3.2 Model simulations . . . 13

1.4 Thesis outline . . . 16

2 Data and Methodology 19

2.1 UK Weather Radar Network . . . 19

2.2 3D Radar Composite . . . 21

2.3 CAMRa . . . 24

2.4 Unified Model . . . 24

2.4.1 Global Model . . . 26

2.4.2 Regional Model . . . 26
2.4.3 Wilson-Ballard Microphysics . . . 28
2.4.4 CASIM . . . 29
2.4.5 Comparing rain processes in Wilson-Ballard with CASIM . . . 30
2.4.6 Rain microphysical variables . . . 35

3 Verifying $Z_{\mathbf{DR}}$ in the 3D radar composite against CAMRa RHIs 37
3.1 Introduction and aims . . . 37
3.2 Vertical cross sections of the radar composite . . . 38
3.2.1 Correction of spatial location of radar beams in compositing software . . . 39
3.2.2 Visual comparison of Z_{DR} . . . 39
3.3 Comparing regridded CAMRa data with radar composite . . . 41
3.4 Summary and conclusions . . . 45

4 Use of $Z_{\mathbf{DR}}$ columns for early detection of severe convection within the operational radar network of the United Kingdom 49
4.1 Introduction . . . 50
4.2 Cases of Severe Convection . . . 52
4.2.1 Radar-based definition of severe convection in the United Kingdom . . . 52
4.2.2 Cases . . . 53
4.3 Data and Methodology . . . 54
4.3.1 UK 3D radar composite . . . 54
4.3.2 Cell identification . . . 56
4.3.3 Z_{DR} column detection algorithm . . . 58
4.3.4 Example of Z_{DR} column detection . . . 59
4.4 Results . . . 59
4.4.1 Time series analysis . . . 59
4.4.2 Nowcasting verification . . . 64
4.5 Discussion and Conclusions . . . 69
4.6 Supplementary Information . . . 72
4.6.1 Explaining the Otsu image thresholding algorithm . . . 72
4.6.2 The effect of using a secondary threshold in Z_{DR} column detection . . . 73

5 Forward Operator for $Z_{\mathbf{DR}}$ 75
5.1 Introduction . . . 75
5.1.1 Pre-exisiting radar forward operator . . . 77
5.1.2 Wilson-Ballard . . . 77

5.1.3 CASIM . . . 79
5.2 Forward Operator Design . . . 80
5.2.1 Scattering Calculations . . . 81
5.2.2 Comparison between Rayleigh and non-Rayleigh . . . 81
5.2.3 Aspect Ratio . . . 82
5.2.4 Canting Angle . . . 84
5.2.5 Double Moment Microphysics . . . 85
5.3 Implementation . . . 86
5.4 Online Testing . . . 88
5.5 Summary and Conclusions . . . 91

6 Evaluation of $Z_{\mathbf{DR}}$ in the Unified Model 93
6.1 Introduction . . . 93
6.2 Case Overview . . . 94
6.3 Comparing radar variables . . . 95
6.4 Presence of Z_{DR} columns . . . 101
6.5 Updrafts . . . 104
6.6 Microphysics . . . 107
6.7 Summary and conclusions . . . 111

7 Summary and future work 117
7.1 Overview . . . 117
7.2 How reliably are Z_{DR} signatures represented within the 3D radar composite? . . . 118
7.2.1 Summary . . . 118
7.2.2 Limitations and future work . . . 119
7.3 How effectively could Z_{DR} columns be used for the early detection of severe convection within the United Kingdom? . . . 120
7.3.1 Summary . . . 120
7.3.2 Limitations and future work . . . 120
7.4 How could Z_{DR} be simulated within the Met Office Unified Model? . 121
7.4.1 Summary . . . 121
7.4.2 Limitations and future work . . . 122
7.5 How is Z_{DR} represented within the Met Office Unified Model coupled to different microphysics schemes? . . . 123
7.5.1 Summary . . . 123
7.5.2 Limitations and future work . . . 124
7.6 Concluding remarks . . . 125

Bibliography 127

They call it that good ol' Z_{DR};
Them that refuse it get a star.
I will hush up my mug if they'll just
  pull the plug
On that good ol' Z_{DR}.

Chorus of "The Differential Reflectivity Blues"
Paul L. Smith (1984)

Chapter 1

Introduction

Intense updrafts within severe convective storms have been known to play a contributing role to their growth. The presence of intense updrafts can have a substantial impact on whether convective cells develop into severe storms. Updrafts of sufficient magnitude support and loft hydrometeors into higher parts of a convective cell allowing for enhanced growth via collision and collection processes. Although there is abundant evidence of intense updrafts from previous in-situ and remote sensing studies using research radars, their potential for use within the operational short range forecast setting has yet to be explored. This is complicated by difficulties in efficiently detecting updrafts and hydrometeors within cells over the range of scales at which they can be observed.

In recent years, radar networks have been upgraded to have dual-polarisation capability. Unlike conventional single-polarisation radars, radars with dual-polarisation emit and receive radio waves in the horizontal and vertical polarisations. This allows them to measure the ratio of backscatter intensity between both polarisations, giving differential reflectivity (Z_{DR}), which is usually used as an indication for the oblateness of radar targets. Alongside radar reflectivity (Z), both quantities used together, provide operational and research meteorologists with new information on the phase and distributions of hydrometeors within precipitating systems. For instance, a high Z and low Z_{DR} hints the presence of large tumbling hail, whereas high values for both quantities could hint at a high concentration of large raindrops instead. More details about dual-polarisation radars can be found in Section 1.2.2. However, such new data from the UK operational radar network have not been utilised thus far for the prediction of severe convective storms.

To improve both the understanding of updrafts in observed convective clouds and inform the development of the microphysical scheme in numerical weather prediction (NWP) models, we require multiple observations of hydrometeors within many clouds. By exploiting data from a composite derived from multiple radars, a high-temporal frequency of cloud observations can be made across a large domain.

This has clear benefits over using methods such as in-situ aircraft measurements, or radiosonde ascents which can only collect meteorological data from a single point in space at a time. The coverage of a single radar is also much smaller compared to using multiple radars. A three-dimensional radar composite derived from a dense radar network also permits neighbouring radars to fill in regions of space that would be missing if only a single radar was utilised. Previous studies have demonstrated the usefulness of 2D and 3D gridded multi-radar reflectivity products with more recent works investigating dual-polarisation radar measurements for hazard warning products.

Although the general approach to observing Z_{DR} using dual-polarisation radars is well established, past radar observation studies generally focus only on single storm cases. The use of a 3D radar composite with Z_{DR} allows for a range of case days to be studied. By developing an objective detection algorithm that works in the composite, consistent identifications of an intense updraft proxy, a Z_{DR} column, could be made within convective cells. The extension of the composite to output Z_{DR} provides another way to evaluate the microphysics parametrisations and dynamics of an NWP model.

The work chapters in this thesis explores the following research questions.

1. How reliably are Z_{DR} signatures represented within the 3D radar composite?

2. How effectively could Z_{DR} columns be used for the early detection of severe convection within the United Kingdom?

3. How could Z_{DR} be simulated within the Met Office Unified Model?

4. How is Z_{DR} represented within the Met Office Unified Model coupled to different microphysics schemes?

In this thesis, the reliability of the Met Office 3D radar composite is assessed by comparing reflectivity (Z_{H}) and differential reflectivity (Z_{DR}) from the Chilbolton Advanced Meteorological Radar (CAMRa), which is a very high resolution research radar. Please see Section 2.3 for more details. A Z_{DR} column detection algorithm is implemented for use with the composite to study its potential in nowcasting severe convection. A forward operator is written to simulate Z_{DR} within the Met Office Unified Model (MetUM), thus allowing radar observations to be compared to MetUM output. Statistics from a case day are used to evaluate the microphysics schemes in MetUM simulations.

1.1 Severe convective storms and updrafts

1.1.1 What are severe convective storms?

Convection is the movement within a fluid driven by differences in fluid buoyancy. When a buoyant parcel of air is lifted via convective ascent, it is cooled by adiabatic expansion. By the Clausius-Clapeyron relation for water, saturation vapour pressure decreases with decreasing temperature. Cloud formation occurs when the saturation vapor pressure becomes smaller than the actual partial pressure of water vapour in the air.

A cumulonimbus cloud is a convective cloud or system of clouds that produces rainfall and lightning (Cotton et al., 2011). Such a cloud often produces large hail, severe wind gusts, tornadoes and heavy rainfall. The US National Weather Service defines severe thunderstorms as storms producing a tornado, or having winds of at least 58 mph, or producing hail of at least 1 inch in diameter (National Weather Service, 2017). In the United Kingdom, the Met Office issues weather warnings through the National Severe Weather Warning Service depending on a combination of the impact of the severe weather and the likelihood of impacts (Suri and Davies, 2021). Severe convective storms affecting any part of the UK could trigger rain, thunderstorms, wind, lightning warnings, or any combination of the above.

Severe convective storms can result in damage to property, travel delays and cancellations, loss of water supplies, power cuts and, in the most severe of cases, bring danger to life. It is thus important for meteorologists to better nowcast and understand how such storms form, develop and evolve.

1.1.2 How do severe convective storms form?

The development of a thunderstorm requires suitable vertical temperature and moisture profiles and a mechanism of triggering or destabilisation.

The temperature profile should be conditionally unstable, where the lapse rate is between the moist adiabatic lapse rate and the dry adiabatic lapse rate. Sufficient boundary layer moisture should also be present. Both factors contribute to convective available potential energy (CAPE), which is defined as the energy released when a parcel that is lifted above its level of free convection experiences an upward buoyancy force. The reference parcel for computing CAPE is usually lifted from the surface or is representative of the mean temperature and humidity of the boundary layer.

CAPE is defined as integrating buoyancy of an air parcel in the vertical from the level of free convection (LFC) to the level of neutral buoyancy (LNB) as in

Equation (1.1) (Ambaum, 2020).

$$\text{CAPE} = \int_{\text{LFC}}^{\text{LNB}} b \; dz \tag{1.1}$$

$$\approx R_d \int_{\text{LNB}}^{\text{LFC}} (T_p - T_e) \; \frac{dp}{p} \tag{1.2}$$

Assuming that the surrounding atmosphere is hydrostatically balanced and using the ideal gas law, CAPE can be derived by integrating the difference in parcel temperature T_p and environmental temperature T_e through pressure levels p (Equation (1.2)). R_d is the specific gas constant for dry air.

If it were common for parcels to easily reach the LFC and realise the release of energy from convective instability, CAPE would never build up to values sufficient to support updrafts needed in vigorous deep convection. Hence, convection has to be inhibited by a stable layer or inversion at the top of the boundary layer, such that convective inhibition (CIN) is non-zero but not too large, so as to preclude any possibility of deep convection. Figure 1.1 is an example of a profile with some CIN and little surface-based CAPE. High surface temperature values that were present later during the day led to more CAPE and less CIN.

For the CAPE inherent in the vertical atmospheric profile to be realised, the environmental air needs to be destabilized by lifting. Lifting destabilises the environmental sounding by weakening the inversion that caps the mixed boundary layer so that buoyant air parcels from below can break through it. Air parcels within this destabilised air mass will also need to be lifted up to their LFC. Destabilising the environmental sounding is often associated with synoptic scale forcing such as middle or upper level mesoscale vortices and dry intrusions leading to split-frontal structures. In addition to frontal boundaries, upper level features such as areas downstream of an upper level trough and the left exit of a jet promote rising motion in the lower troposphere (Groenemeijer et al., 2005). In contrast, the lifting of an air parcel within the destabilised airmass could be associated with a more local forcing such as a sea-breeze front, orography or cold pool outflows from pre-existing convective systems (Bennett et al., 2006). The discussion here, especially on triggering mechanisms, is focused on extratropical convection.

An environment with vertical wind shear, where there is an increase in wind speed with height, is conducive for convective storm development since it aids the organisation of the updraft-downdraft couplet inside a storm as seen in severe hailstorms (Cotton et al., 2011). However, vertical shear of the horizontal wind could also increase the rates of entrainment into a cloud system that is generally unfavourable for convective development.

With the correct conditions, the evolution of a thunderstorm can be classified into

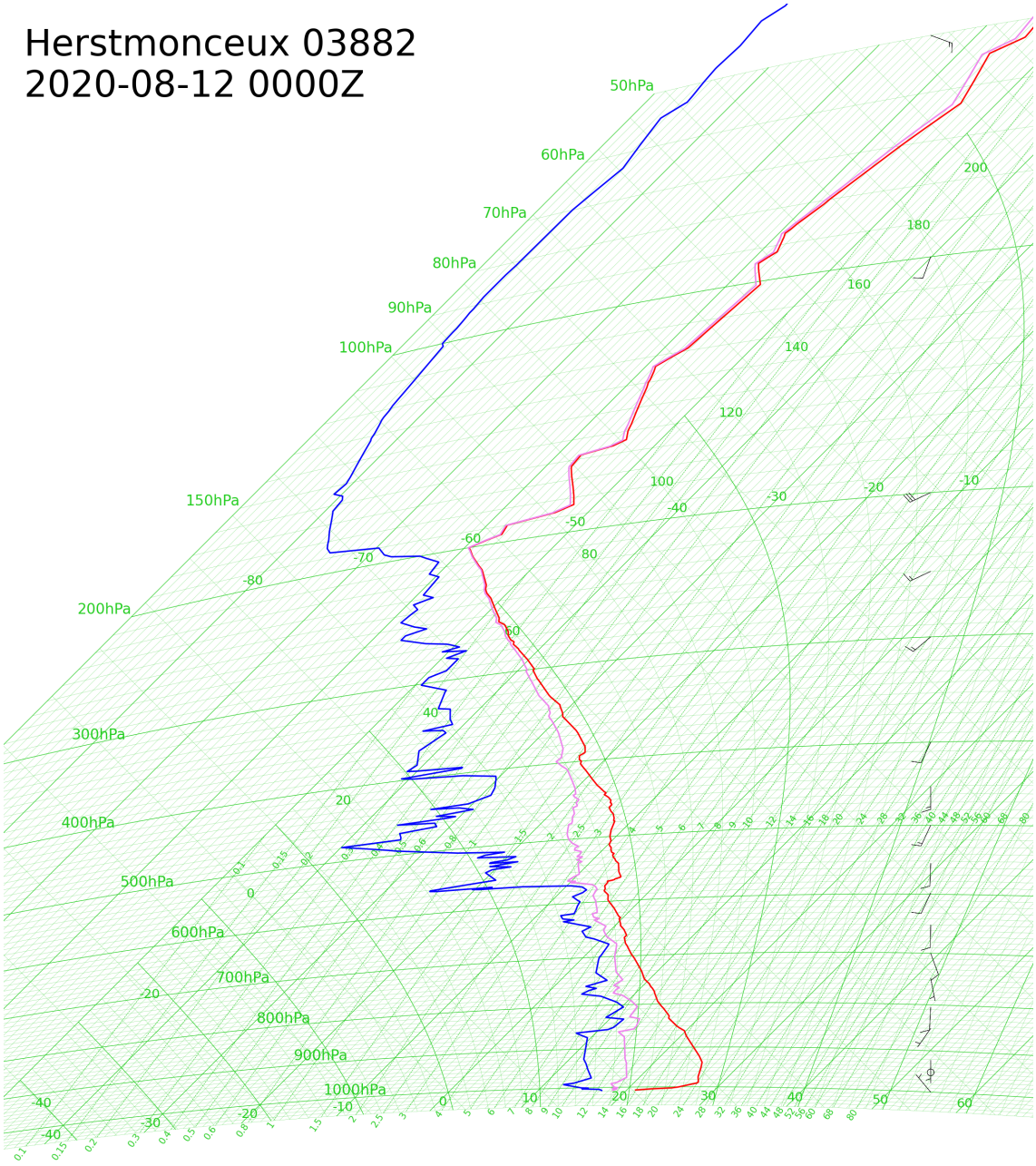

Figure 1.1: Tephigram showing radiosonde ascent data from Herstmonceux for 12 August 2020 at 0000Z. The blue, magenta and red lines are the dew-point temperature, wet-bulb temperature and air temperature respectively. Data from University of Wyoming.

three stages: cumulus, mature, and dissipating (Cotton et al., 2011). As illustrated in Figure 1.2a, the cumulus stage is characterised by one or multiple cumulus towers that are fed by low-level convergence of moist air. While updrafts dominate, there are also penetrative downdrafts near cloud tops and on the downshear flank of the cumuli. Precipitation may also begin to form at cloud tops. The transition from the cumulus to mature phase is marked by the presence of precipitation below the cloud base associated with the merger of cumuli into a larger system. Shown in Figure 1.2b, updrafts may extend to the whole depth of the troposphere forming overshooting cloud tops and anvils when the updraft diverges. Just above the surface, the cold downdrafts chilled by evaporating precipitation spreads out to form a gust front. In the dissipating stage, downdrafts dominate. As seen in Figure 1.2c, the cloud dome caused by intense updrafts disappears. The cold pool at the surface advances far from the cloud, so any updrafts triggered by the gust front can no longer feed the original storm updrafts. Stratiform precipitation prevails at the trailing edge of the cell.

In order to efficiently observe hydrometeors within storm systems in three spatial dimensions and study storm evolution, we require a remote sensing instrument to peer into such storms.

1.2 Radar observations of severe storms

1.2.1 How do radars observe severe storms?

Radar, an acronym for RAdio Detection And Ranging, is an instrument that emits high power electromagnetic waves in the microwave region and then measures the echoes when these waves reflect off a target, such as raindrops or hail.

Weather radars operate in different bands that use different wavelengths. The S, C and X-bands describe radio wave wavelengths of around 10, 5 and 3 cm respectively. There are several benefits and drawbacks to choosing wavelengths for a radar. In terms of hardware, radars using shorter wavelengths permit a more compact and thus portable antenna for a given beamwidth. However, shorter wavelengths are affected more strongly by attenuation, whereas longer wavelengths produce data with larger random uncertainties for a given sampling time. The shorter the wavelength, the more frequently the scattering from hydrometeor targets will occur outside the Rayleigh regime, which is alluded to later in Equation (1.5) and a factor which I investigate in detail in Chapter 5. For operational networks, S-band is typically used by meteorological services in areas where heavy convective rain is common. C-band radars are common in mid and high latitude regions where such storms are more infrequent. The portability of X-band radars makes them beneficial for filling gaps

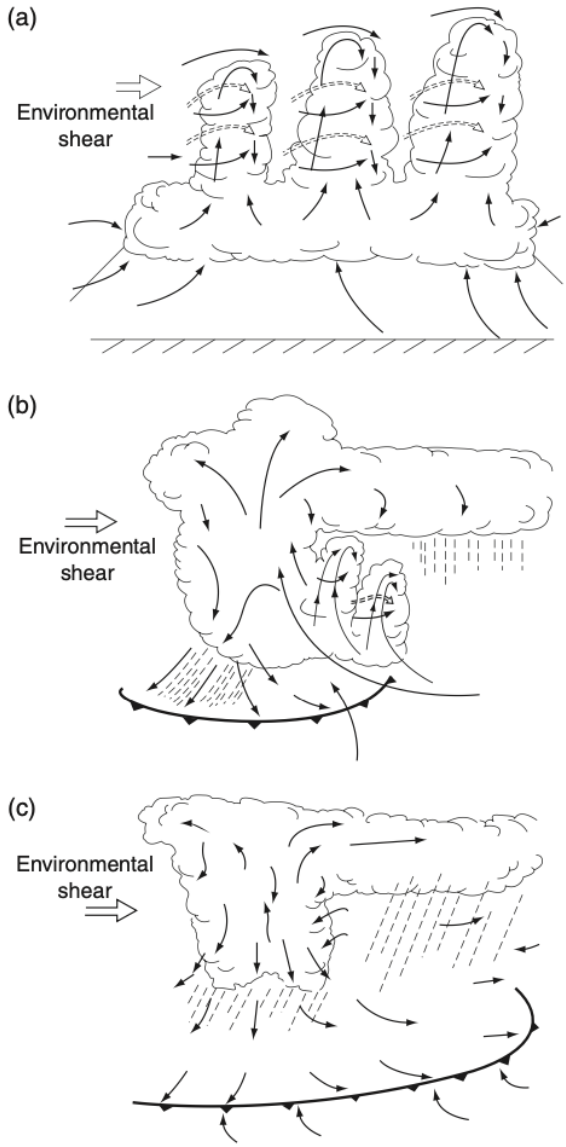

Figure 1.2: A schematic model of the lifecycle of a typical thunderstorm. Figure from Cotton et al. (2011).

in networks, temporary deployment for field campaigns, or deployment in difficult to access regions such as mountain ranges.

A conventional single polarisation radar operates by transmitting polarised (oscillation could be in a plane parallel to the ground) electromagnetic radiation radially outwards in one direction, then detects faint echoes from radiation backscattered by targets. Targets can include precipitation, dust, and smoke scatterers, where the latter two items are non-meteorological targets. The amount of scattered radiation from a target depends on its size, shape, orientation and physical composition, which affects scattering through the target's complex refractive index. Since the single polarisation radar only emits and receives signals in a single plane, radar reflectivity η is measured.

$$\eta = \int_0^\infty N\left(\sigma_b\right) \sigma_b \, d\sigma_b \tag{1.3}$$

This quantity is a sum of all radar cross section (σ_b) contributions of N individual targets each having a certain backscatter cross section.

If one assumes Rayleigh scattering regime, such that the size of scatterers is considerably smaller than the radar's wavelength, then η is approximated as

$$\eta = \frac{\pi^5}{\lambda^4} \left| \frac{n^2(\lambda) - 1}{n^2(\lambda) + 2} \right|^2 \int_0^\infty N(D) D^6 \, dD \tag{1.4}$$

From this, radar reflectivity factor Z is derived:

$$Z = \int_0^\infty N(D) D^6 \, dD \tag{1.5}$$

where $N(D)$ is the number of particles of diameter between D and $D + dD$ per unit volume and Z having units of $\mathrm{mm^6 m^{-3}}$. Since Z in $\mathrm{mm^6 m^{-3}}$ units can take a large range of values under different meteorological situations, Z can be transformed into logarithmic units dBZ.

$$Z\,[\mathrm{dBZ}] = 10 \log_{10} Z \left[\mathrm{mm^6 m^{-3}}\right] \tag{1.6}$$

A network of operational weather radars, such as the one in the UK, permits a larger observation space of radar reflectivity Z that would normally contain regions of missing observations if only a single radar was available. Data from multiple radars can be composited to a 3D grid. Scovell and al-Sakka (2016) found that such a 3D composite provides important information for aviation meteorology where pilots navigate to avoid areas of severe convective development. More details about the UK radar network and the 3D composite are in Sections 2.1 and 2.2.

1.2.2 What is dual-polarisation? How is Z_{DR} observed?

Dual polarisation (also called polarimetric) radars transmit electromagnetic radiation in both the horizontal and vertical planes as shown in Figure 1.3. The interaction of the electromagnetic wave with hydrometeors occurs via the electric field of the wave, as the field in the air induces a field within the hydrometeor. Due to the higher refractive index of the hydrometeor, the field in the hydrometeor will travel slower than the field in air. The axes of polarisation are modified by the hydrometeor's shape, size and refractive index. The field in the hydrometeor interacts back with the field in the air, producing a combination of the following effects: a partial reflection of the wave with a different phase delay with respect to what would be expected of a point target, partial attenuation from forward propagation of the wave and absorption, and an additional delay with respect to the case of no hydrometeor particle present (Fabry, 2015). In other words, a non-spherical hydrometeor particle acts like a microscopic antenna that scatters energy in the horizontal or vertical plane when illuminated by electromagnetic waves oscillating in the horizontal or vertical plane. Therefore, the added value of polarimetric radar variables provides the ability to glean information regarding hydrometeor particle size, shape and orientation within the radar sampling volume. Information is usually encoded in polarimetric radar variables.

Radar reflectivity factor Z could be measured by a single plane-polarised radio waves. If measured by horizontally polarised electromagnetic waves in a conventional single-polarisation radar, the quantity of radar reflectivity factor is expressed as Z_{H}. Radar reflectivity factor could also be measured by vertically polarised electromagnetic waves and expressed as the quantity Z_{V}. The measurement of radar reflectivities in both planes of polarisation is only available in dual-polarisation radars.

Seliga and Bringi (1976) first introduced the idea of using differential reflectivity Z_{DR} as a parameter for characterising rain microphysics. It is the ratio of reflectivity factors measured by horizontally polarised waves Z_{H} to the reflectivity factor measured by vertically polarised waves Z_{V}. Differential reflectivity is more conveniently expressed in its logarithmic form, as the difference in units of dB.

Z_{DR} can be interpreted as a metric for reflectivity-weighted particle axis ratio. A completely spherical particle should return equal power in the H and V polarisations, yielding zero Z_{DR}. In contrast, oblate particles with their major axis aligned along the horizontal plane produce a positive Z_{DR}. Large raindrops experience a greater drag force due to their high terminal velocity and larger surface area. The balance between this drag force and the surface tension of the raindrop gives it an oblate geometry and thus resulting in polarimetric radars measuring a positive Z_{DR}. Another factor affecting Z_{DR} comes from the weighting of refractive index of hydrometeors

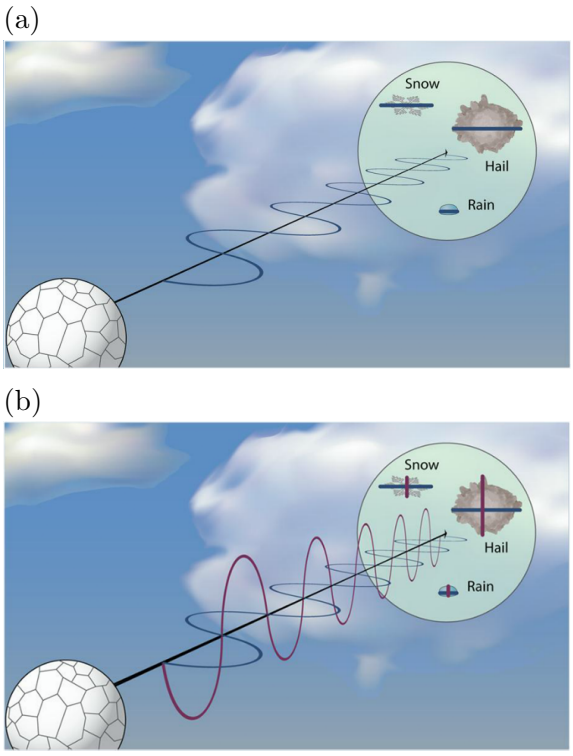

Figure 1.3: (a) An idealised schematic of the horizontally oscillating waves transmitted and detected by a conventional radar. (b) A similar schematic showing horizontally and vertically oscillating waves transmitted and detected by a dual-pol radar. Diagrams from National Weather Service.

within a radar sampling volume. The Z_{DR} value for a radar sampling volume containing a majority of oblate water droplets will be larger than that for a sampling volume containing the same number of hydrometeors where the majority are oblate ice pellets. The greater refractive index of liquid water than ice means that a larger proportion of oblate water droplets in a sampling volume weighs towards increasing Z_{H} more than Z_{V} and thus a larger Z_{DR}.

1.2.3 What are Z_{DR} columns?

One of the features of interest in convective storm development, available from differential reflectivity measurements, and the focus of this thesis are Z_{DR} columns - "columnar regions of enhanced Z_{DR} that extend above the environmental 0 °C level" (Kumjian, 2013). Although there is no explicit definition of an enhanced Z_{DR} value, Kumjian et al. (2014) and Snyder et al. (2015) use a 1 dB contour above the 0 °C level to describe a Z_{DR} column. There are also no strict criteria for the vertical extent of this 1 dB contour, although Plummer et al. (2018) requires a column to extend at least 500 m above the environmental 0 °C level.

The very first paper to document but not discuss the phenomenon is Hall et al. (1980). Later, Hall et al. (1984) observed high Z_{DR} values extending in the

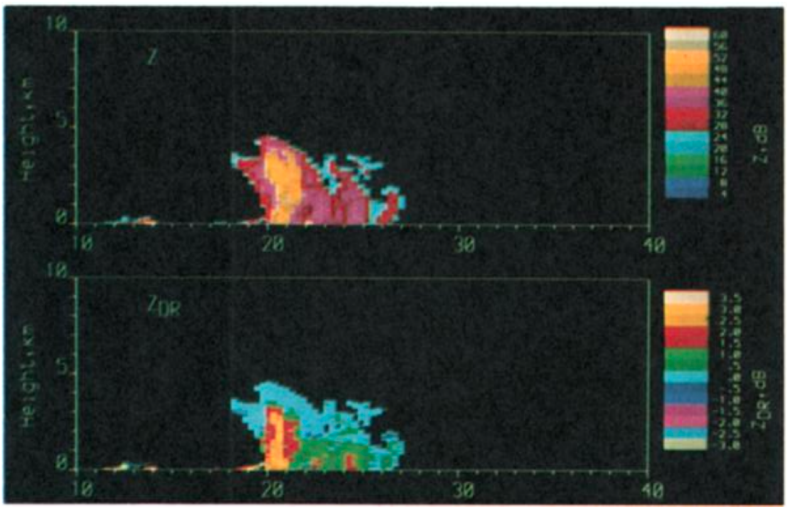

Figure 1.4: Vertical cross section through a convective storm with rain and ice obtained on 02 July 1980 at 1635Z by Hall et al. (1984). The top panel shows radar reflectivity Z_{H} in dBZ units with the colour bar ranging from 4 to 60 dBZ. The bottom panel shows differential reflectivity Z_{DR} in dB units with the colour bar ranging from -3.0 to 3.5 dB. The horizontal and vertical scales are in kilometres.

vertical using range-height indicator (RHI) scans of CAMRa. This is shown in Figure 1.4 where a column of both high Z and Z_{DR} reach up to 3.5 km in height, which is a rather prominent Z_{DR} column extending beyond the freezing level at 2.0 km on that day. They interpreted this as a column containing supercooled water carried up in an updraft. Through a detailed inspection of several case studies, Illingworth et al. (1987) suggested that large drops within Z_{DR} columns originated from condensation and coalescence growth of smaller raindrops as they descended through the updraft. The authors also noted that low Z and positive Z_{DR} above the freezing height when the cloud echo top is rapidly rising preceded high values of Z. Caylor and Illingworth (1987) hypothesised anomalously large Z_{DR} values were the presence of ultra giant large cloud condensation nuclei that eventually grow into large drops. Although their drop growth modelled Z_{DR} values that were larger than the observations, traditional coalescence growth from smaller nuclei could not be ruled out. A follow up study by Illingworth (1988) also shared similar conclusions. Tuttle et al. (1989) documented a Z_{DR} column extending more than 2 km above the freezing level and noted that the storm's first echo was below the melting level, suggesting precipitation development was through accretion and coalescence growth of liquid drops in the warm layers. The observed Z_{DR} column also coincided with Doppler-derived updraft speeds exceeding $25\,\mathrm{m\,s^{-1}}$.

As polarimetric radar observations became more common, so did the observation of Z_{DR} columns (e.g. Wakimoto and Bringi, 1988; Shupyatsky et al., 1990; Balakrishnan and Zrnić, 1990; Vivekanandan et al., 1990; Bringi et al., 1991; Meischner et al.,

1991; Herzegh and Jameson, 1992; Conway and Zrnić, 1993; Ryzhkov et al., 1994; Höller et al., 1994; Raghavan and Chandrasekar, 1994; Yuter and Houze, 1995). In particular, Bringi et al. (1991) combined radar observations with aircraft drop spectra measurements to analyse the life cycles of three convective storms. The aircraft penetrations revealed collocation of updraft regions with positive Z_{DR}. Although the conclusions in the study were similar to deductions in Illingworth et al. (1987) regarding Z_{DR} columns initially containing a low concentration of large drops, they were the first to point out the significance of size sorting within these columns. Conway and Zrnić (1993) focused more on the role of Z_{DR} columns in embryo production and hail growth. Using dual-doppler analysis, they were able to distinguish mature Z_{DR} columns formed by recirculation of ice particles from the Z_{DR} columns found in developing cumulus. Similar to previous literature, Z_{DR} columns were generally collocated with updrafts, although with slight offsets from the strongest updraft centres. Brandes et al. (1995) similarly observed this and surmised that the largest drops with too high of a terminal velocity would have fallen from sloping updrafts creating offsets between Z_{DR} columns and updraft cores.

Later works such as Bringi et al. (1997) documented the diminishing stage of a Z_{DR} column and attributed this to mostly downdrafts left behind by an ascending updraft maximum. The authors also found a mixture of frozen and liquid drops with other frozen hydrometeors within the updraft. Other studies also interpreted other polarimetric signatures atop of Z_{DR} columns as the growth of wet frozen drops in the presence of high cloud water content (Bringi et al., 1996; Jameson et al., 1996) or the presence of wobbling freezing drops without wet growth (Bringi et al., 1997; Hubbert et al., 1998). Smith et al. (1999) agreed that freezing of raindrops near the top of Z_{DR} columns is a possible hail embryo source, which supports Kennedy et al. (2001)'s result that Z_{DR} columns preceded surface hail reports.

Jameson et al. (1996) highlighted the simultaneous appearance of glaciating radar signatures at the top of Z_{DR} columns and the electrification of small convective storms. Similar observations linking the importance of Z_{DR} column in electrification with the occurrence of lightning were also demonstrated in several other works (e.g. Goodman et al., 1988; Carey and Rutledge, 2000; Bruning et al., 2007; MacGorman et al., 2008; Woodard et al., 2012; Mattos et al., 2016, 2017).

With even more polarimetric radars in the 21st century, there is a whole library of Z_{DR} column observations within single or multicell storms (e.g. Tong et al., 1998; May et al., 2001; Zeng et al., 2001; Cifelli et al., 2002; Knight et al., 2002, 2004; Knight, 2006; Evaristo et al., 2010; Rowe et al., 2012; Homeyer and Kumjian, 2015; Kuster et al., 2016; Plummer et al., 2018) and supercells (e.g. Loney et al., 2002; Ryzhkov et al., 2005; Scharfenberg et al., 2005; Tessendorf et al., 2005; Kumjian and Ryzhkov, 2008; Kumjian et al., 2010; Tanamachi et al., 2012; Kaltenboeck and

Ryzhkov, 2013; Snyder et al., 2013; Homeyer and Kumjian, 2015; Broeke, 2017). In particular, Scharfenberg et al. (2005) suggested that deeper Z_{DR} columns indicate stronger updrafts and demonstrated their usefulness in operational forecasting of developing storms. In a study by Picca et al. (2010), Z_{DR} columns were investigated and found to temporally precede increasing precipitation and hail intensity, thus hinting even more at the operational utility of Z_{DR} columns.

1.3 Predicting severe convection using Z_{DR} columns

1.3.1 Nowcasting using Z_{DR} columns

The first known automatic Z_{DR} column detection algorithm, to my knowledge, was designed by Snyder et al. (2015) to provide additional storm diagnostic and prognostic information for storm nowcasting. This algorithm was then used by Kuster et al. (2019) and applied to rapidly updated radar volume scans, completed by a single radar every two minutes or less. They found that Z_{DR} column depths were significantly larger for severe storms compared to non-severe storms. As a follow up study to explore whether the results hold for realtime data available to and used by forecasters, Kuster et al. (2020) highlighted the importance and usefulness of Z_{DR} columns in informing forecast warning decisions, compared to only utilising reflectivity signatures. For instance, they found a Z_{DR} column developing about 10 min prior to the appearance of a bounded weak echo region (BWER) in the $-20\,^{\circ}\mathrm{C}$ Z_{H} field (Figure 1.5) with hail reports after a further six minutes. BWERs are believed to be caused by updrafts so strong that precipitation is unable to fall through them and are a signature of severe storms (Chisholm, 1973).

Previously mentioned studies have outlined the merits of Z_{DR} columns for informing conceptual models or warning decisions. It was also noted that scanning strategies and volumetric update times will affect the sampling of such columns. These works only considered the detection and use of Z_{DR} columns for nowcasting severe convection detected by single-site radar scans. Hence, there is great interest to explore the potential of Z_{DR} columns for nowcasting using a 3D radar composite that combines data from multiple C-band radars.

1.3.2 Model simulations

Regarding the simulation of Z_{DR} columns and their evaluation with observations, the use of a spectral bin microphysics scheme allows for detailed particle size distributions for studying polarimetric signatures in convective storms. Ryzhkov et al. (2011) presented simulated fields of the polarimetric variables from the Hebrew Uni-

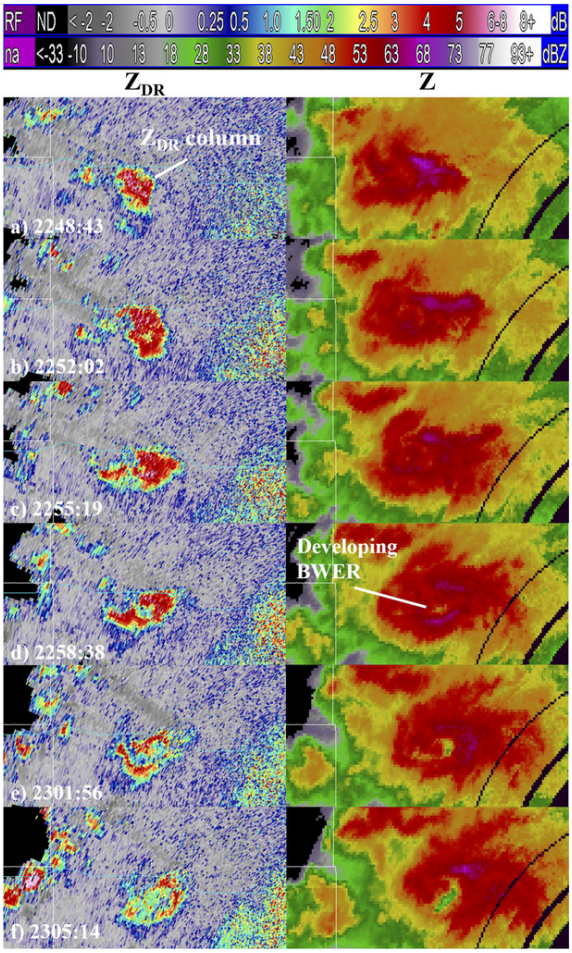

Figure 1.5: (left) Z_{DR} in dB units at 4.05° of elevation and (right) −20 °C reflectivity in dBZ units for every other volume scan between (a) 224843Z and (f) 230514Z on 31 May 2013 observed by the WSR-88D (KOUN) radar located in Norman, Oklahoma. This Z_{DR} column developed about 10 minutes prior to the development of a bounded weak echo region (BWER) in the −20 °C reflectivity field. Storm range from radar is from about 66 km in (a) to 61 km in (f). Figure from Kuster et al. (2020).

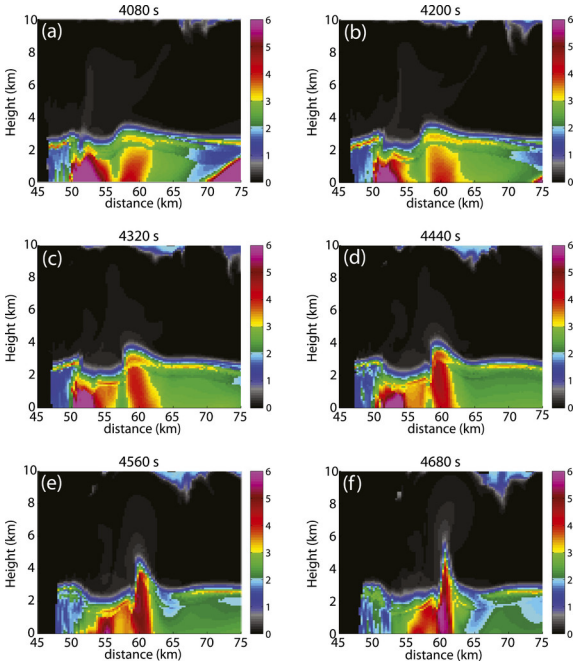

Figure 1.6: Snapshots of the evolution of the simulated Z_{DR} field over a 10 minute period from 4080 to 4680s. Figure from Kumjian et al. (2014).

versity Cloud Model, including a Z_{DR} column. Also using the same cloud model, Kumjian et al. (2014) successfully simulated the formation and subsequent life cycle of Z_{DR} columns in a deep convective continental storm as seem in Figure 1.6. The study was able to model the formation of large raindrops in the updraft by recirculation of smaller raindrops into the updraft at lower levels. The transition from supercooled liquid drops to freezing drops to hail at higher levels in the Z_{DR} column was also well modelled.

Using a bin microphysics scheme within a sub-km resolution model is rather expensive and limits the simulation to two dimensions. A bulk microphysics parametrisation scheme, although less accurate, is usually implemented in operational NWP models. Jung et al. (2010) used a two-moment bulk microphysics scheme and simulated supercell storms in an effort to reproduce Z_{DR} columns in such storms. Using a three-moment scheme and the same polarimetric radar operator, Snyder et al. (2010) noted that increased CAPE leads to larger Z_{DR} columns. In both studies, simulated columns attained a maximum vertical extent short of the observed column heights in supercells. In a later modelling study by Kumjian et al. (2014), the discrepancy in simulated and observed heights is explained by the instantaneous drop freezing in the microphysics scheme, which is in contrast to the duration of freezing taking up to several minutes in reality for millimeter-sized drops.

Many of the described studies have simulated Z_{DR} columns in various cloud models in hopes of reproducing and understanding observations. However, such cloud models are mostly designed for research purposes. Operational forecasting centres

increasingly rely on convection-permitting NWP models as an aid in forecasting convective events beyond the timescale of nowcasting methods. The ongoing evaluation of NWP model improvements is vital and normally happens through routine verification using traditional metrics on two-dimensional fields, such as a gridded plan view rainfall product. Object- and process-based evaluation can better identify specific physical mechanisms for model improvement. Stein et al. (2015) sampled more than a thousand convective storms over the southern UK using CAMRa and demonstrated that MetUM simulated storm widths to be wider than reality at 1.5 km horizontal resolution runs, and more realistic at 200 m resolution. Shrestha et al. (2022) carried out ensemble simulations within the Terrestrial Systems Modelling Platform to evaluate modelled summertime convective storms against radar measurements. Despite being able to simulate Z_{DR} columns, they found their widths and magnitudes to be underestimated compared to observations. There has yet to be a study that exploits the benefits of a 3D radar composite containing polarimetric radar measurements from multiple radars for evaluating convective storms within an operational NWP model.

1.4 Thesis outline

This thesis aims to explore the use of observed Z_{DR} from the UK's radar network which, until now, has not been included in the 3D radar composite. Thus, the radar composite is extended to Z_{DR} data. A verification of Z_{DR} signatures in the radar composite was carried out against CAMRa scans. An automatic Z_{DR} column detection algorithm was developed and applied to the radar composite. This prompted the investigation of the operational potential of Z_{DR} columns as precursors of severe convection within the UK. By creating a polarimetric radar forward operator that works within the MetUM, a statistical assessment of simulated Z_{DR} is made against observed Z_{DR} for a case day. Results from sensitivity tests performed in the Met Office Unified Model (MetUM) allows us to evaluate its microphysics schemes.

This thesis is organised as follows: Chapter 2 provides descriptions of the UK weather radar network, the three-dimensional radar composite that combines data from the radar network, CAMRa, the details of microphysical schemes, and simulations carried out in the MetUM. Chapter 3 details a comparison and verification of Z_{H} and Z_{DR} between CAMRa and the UK radar composite. Chapter 4 is an adaptation of a published paper that presents the potential of Z_{DR} columns for nowcasting severe convection within the UK for three case days. In Chapter 5, a polarimetric radar forward operator is implemented within the MetUM to simulate Z_{DR} such that model output could be compared with C-band radar observations.

Chapter 6 is a statistical comparison of various MetUM model simulations with the radar composite to evaluate both the currrently operational single moment microphysics scheme with CASIM double moment microphysics scheme. Lastly, the results and conclusions are summarised and future work is proposed in Chapter 7.

Chapter 2

Data and Methodology

This section details the specifications of the UK weather radar network followed by how data from the network is used in constructing a three-dimensional radar composite. This is followed by an overview of the Chilbolton Advanced Meteorological Radar (CAMRa), which was used to evaluate Z_{DR} features observed in the radar composite. The evaluation of such features is detailed in Chapter 3. Finally, the Met Office Unified Model (MetUM) will be introduced, including specific model parameters suitable for simulating convection.

2.1 UK Weather Radar Network

The Met Office operational weather radar network consists of 15 C-band radars located in various parts of the United Kingdom shown in Figure 2.1. Since January 2018, all radars have been upgraded to have dual-polarisation capability. The radars have a pulse repetition frequency of 300 Hz and a scan velocity of $8.4\,^{\circ}\,\mathrm{s}^{-1}$ for the lowest two elevations and $15\,^{\circ}\,\mathrm{s}^{-1}$ for the higher elevations. Depending on the rotation rate, a variable number of pulses are integrated and averaged for every 1° of azimuth. Each plan position indicator (PPI) scan covers a range of 255 km, has range resolution of 600 m and a radar beamwidth of 1.1°. Assuming a Gaussian-shaped beam pattern with the same beamwidths in the elevation and azimuthal directions, the sampling volume is

$$V = \frac{\pi R^2 (\delta\theta)^2 \delta r}{8 \ln 2} \tag{2.1}$$

where R is the distance from the radar antenna to the centre of the sampling volume, $\delta\theta$ is the angular beamwidth in radians, and δr is the length of the range direction of the sampling volume. With a 3 dB angular beamwidth of 1.1°, each C-band radar would have a beamwidth of 0.96, 1.9 and 3.8 km corresponding to a sampling volume of 0.31, 1.3 and 5.0 km^3 for 50, 100 and 200 km of radar range respectively.

Each radar carries out several PPI scans at five low elevations of 0.5, 1.0, 2.0, 3.0 and 4.0°. Radar beam heights for each elevation are shown in Figure 2.2. Approximately five minutes is required for one complete cycle of these scans.

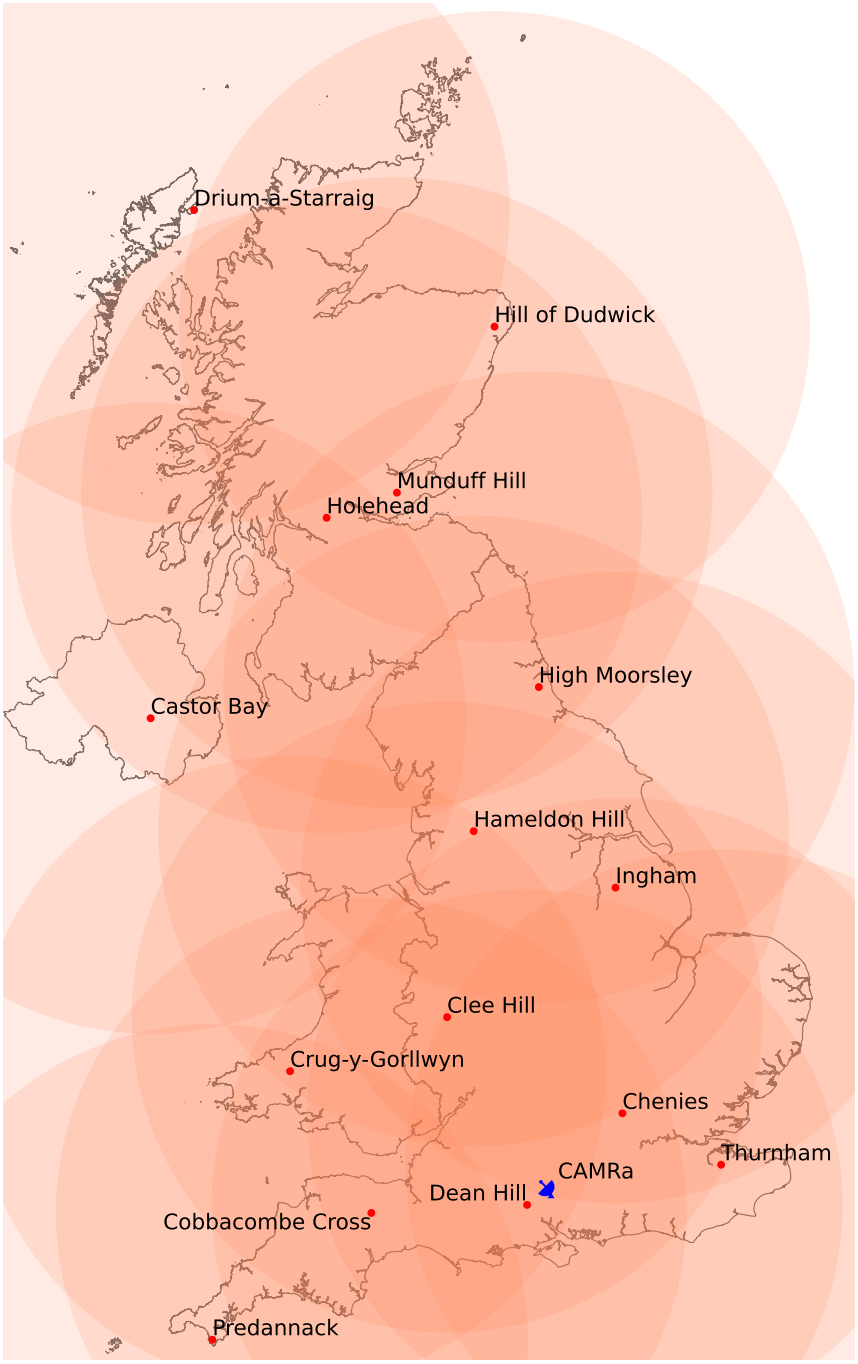

Figure 2.1: An overview of UK Met Office C-band radar locations and names. Range rings of 255 km are included around each radar site. The blue radar dish marks the location of the Chilbolton Advanced Meteorological Radar (CAMRa).

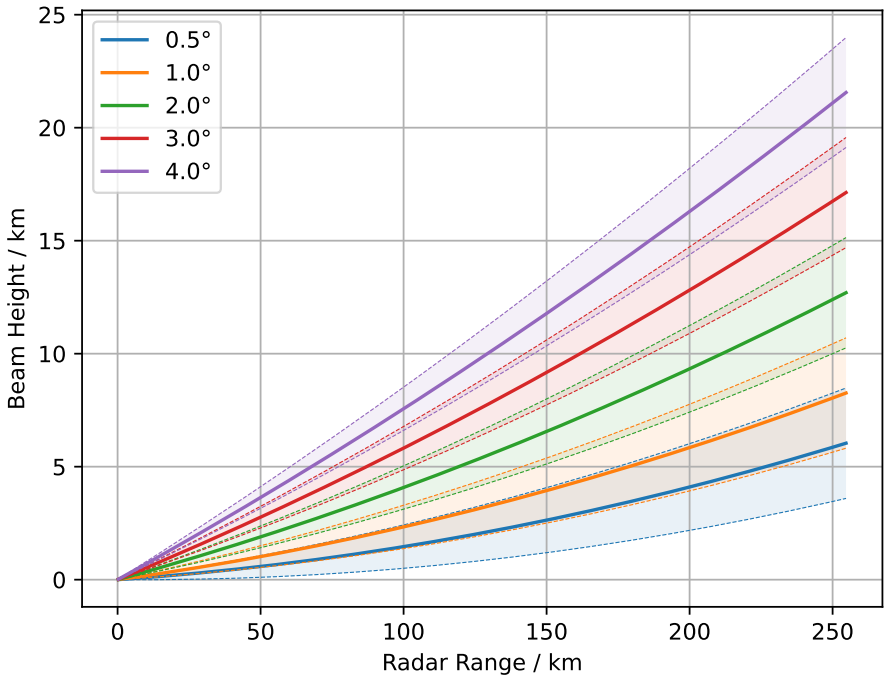

Figure 2.2: Radar beam heights relative to the antenna of C-band radar plan position indicator scans at various elevations. The colour shading indicates the beamwidth of the radar. An effective radius of $\frac{4}{3}$ the Earth's radius is assumed.

2.2 3D Radar Composite

The use of multiple radars in a dense network compensates for the missing coverage of a single radar. The operational systems used by meteorological agenceies have demonstrated the usefulness of three-dimensional gridded multi-radar reflectivity products. For instance, the continental United States mosaic (Zhang et al., 2011) is produced every two and a half minutes on a 3D domain covering the entire contiguous United States at approximately 1 km horizontal resolution for 31 vertical levels of variable spacing. Another example is the Météo-France system, which provides Doppler wind and reflectivity analyses every 15 minutes for nearly the entirety of mainland France at 2.5 km horizontal resolution, with 24 vertical levels spaced at 500 m intervals (Bousquet and Tabary, 2014).

Some areas of the UK could be covered by up to 19 unique radar observations. In order to exploit the benefits of data from a network of radars, Scovell and al-Sakka (2016) formulated procedures to combine radar measurements from single radar sites into a three-dimensional Cartesian grid. The k-d tree algorithm combined with interpolation methods described in the study is sufficiently efficient for real-time applications for the production of 3D multipixel, multi-radar composites. This would allow real-time hydrometeor classification (e.g. Al-Sakka et al. (2013)) products in 3D space and creation of better hazard products such as those suggested in Williams

(a) Radar composite reflectivity Z_{H}

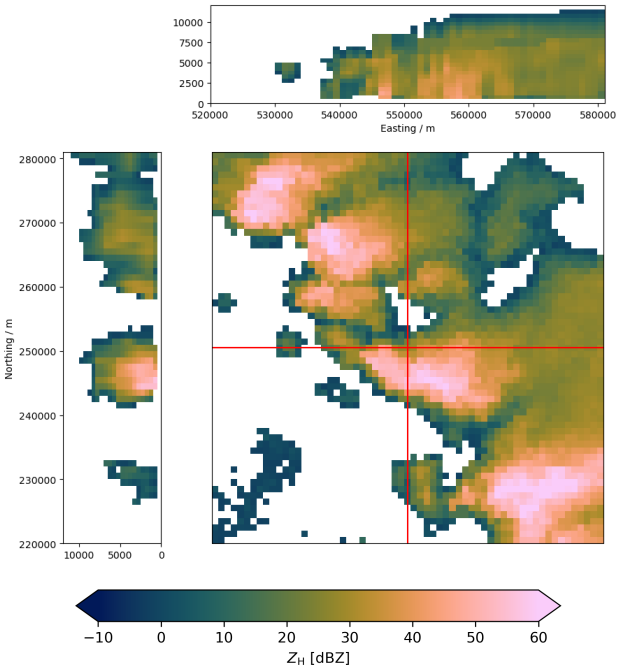

(b) Radar composite differential reflectivity Z_{DR}

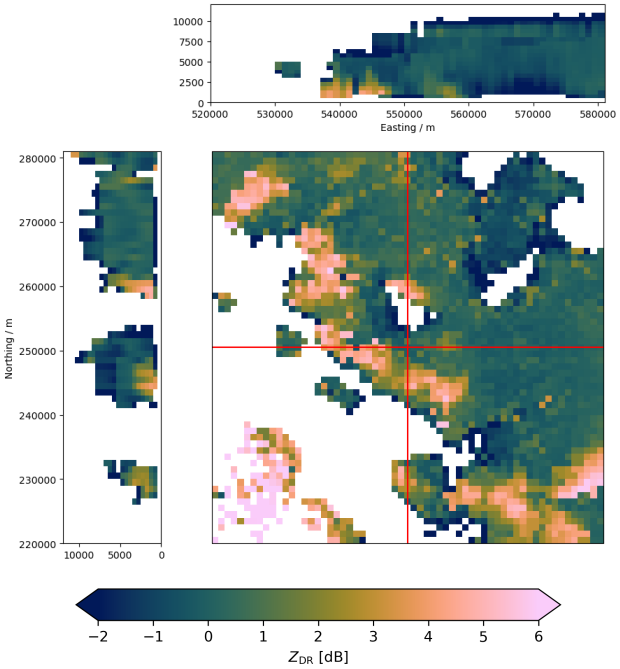

Figure 2.3: Vertical maximum plots from the three-dimensional UK radar composite for a 60×60 km area on 20 July 2021 at 1500 UTC. Side panel plots are vertical transects taken from red lines cutting across the radar composite.

et al. (2011). Derived 3D composite products could also be used for evaluating the representation of convective storms in NWP models. Stein et al. (2020) demonstrated the reliability of the 3D radar composite data in evaluating the morphology of modelled convective storms within the Met Office Unified Model. Such analysis was only possible due to the extensive spatial coverage and high temporal frequency

provided by the UK 3D radar composite. Studies of the evolution and organisation of convective storms over the region could benefit from the operational nature of the network.

To generate a radar composite for a five-minute time period, radar scans within that time period are considered. If the same set of data (same radar, same elevation angle) are available at multiple times, the scan with the time closest to the specified validity time is used. Temporal synchronization is first applied to the observation points. This is the process of advecting radar observation points using horizontal motion vectors derived from the two most recent composites. Afterwards, the three-dimensional interpolation method of Zhang et al. (2005) is applied to observation points. For each grid column on the radar composite grid, the Zhang method searches for the nearest-neighbour radar observation points within a search radius for each PPI scan. The horizontal nearest-neighbour is used to form the column on each horizontal grid point. Then, vertical interpolation (the VI method of Zhang et al. (2005)) is used on each column to derive reflectivity values at 3D composite grid levels for each radar. The interpolated values for each radar, in dBZ, are then averaged on the 3D grid points where they overlap using a Gaussian weighting dependent on the radar's range to the composite grid point.

Figure 2.3a shows an example cutout of this composite for radar reflectivity Z_{H}. The main plot depicts the maximum reflectivity for each vertical column in the composite and clearly highlights intense convective cells at the leading edge of a developing mesoscale convective system. The side panels are cross sections taken along transects marked on the cutout. The meridional cross section shows an area of reflectivity exceeding 40 dBZ within the first few kilometres from the surface, which most likely indicative of heavy precipitation. The zonal cross section presents moderate reflectivities of around 30 dBZ especially in the eastern part covering a more stratiform region. This is an example that demonstrates the ability of the composite in capturing features of interest in both the horizontal and vertical.

Stein et al. (2020) hinted at the propspect of including Z_{DR} to improve the detection of convective cores from enhanced values of Z_{DR}, such as those observed in the COPE field campaign (Plummer et al., 2018). At the time of writing, there is only a 3D radar composite of Z_{H} for experimental purposes, and has not yet become operational within the UK Met Office. In this thesis, the radar composite was extended to include Z_{DR}. Chapters 3, 4 and 6 all rely on the Z_{DR} composite. Similar to Z_{H}, the interpolation of Z_{DR} onto the composite grid was also carried out in dB. Although Warren and Protat (2019) found that interpolation in linear space is more accurate on average for reflectivity Z_{H}, there were no significant differences in resultant values of Z_{DR} when interpolating in linear space compared to interpolating in logarithmic space in my work. Hence, we chose to interpolate Z_{DR} in logarithmic

space. Similar to reflectivity, Figure 2.3b provides the same example but for the vertical maximum of Z_{DR} at each horizontal grid point location and vertical cross sections. In the process of testing the radar composite and extending it to include Z_{DR}, an azimuthal correction was applied on all radars to ensure continuity of featues in the vertical when interpolated onto the composite grid. More details of this will be provided in the next chapter (Chapter 3) of this thesis.

2.3 CAMRa

CAMRa was used to verify Z_{DR} features seen within the radar composite. CAMRa is a 3 GHz S-band weather research radar located at the Chilbolton Observatory in Hampshire, UK. It has dual-polarisation capability in that it alternates between horizontal and vertical polarisation transmissions, while receiving signals in both polarisations simultaneously. CAMRa has an antenna diameter of 25 m, which makes it the largest fully steerable meteorological radar in the world (Figure 2.4). The large antenna allows for a half-power beam width of 0.28°, which provides a resolution of 100 m at 20 km range and 500 m at 100 km range. In contrast to the C-band operational radars, CAMRa has a sampling volume of 0.0025, 0.010 and 0.041 km^3 for 50, 100 and 200 km of range respectively. The C-band radar sampling volumes are more than 120 times the size compared to CAMRa's sampling volumes. Details regarding CAMRa's hardware and signal processing can be found in Goddard et al. (1994). Chapter 3 will compare the detection of Z_{DR} columns and its properties between CAMRa and the C-band 3D radar composite.

The radar reflectivity Z from CAMRa is calibrated to within an accuracy of 0.5 dB. Its narrow beamwidth and high range resolution of 75 m justifies its use in validating Z_{DR} with the 3D radar composite. Range-height indicator (RHI) scans from CAMRa will be used to capture the small-scale and near-instantaneous variations in convective cores.

2.4 Unified Model

The Unified Model (MetUM) is the operational weather forecast model created by the UK Met Office. The MetUM operates with a nonhydrostatic, deep-atmosphere dynamical core and uses a semi-Lagrangian dynamical formulation (Cullen et al., 1997; Davies et al., 2005). It can be run with a range of resolutions and spatial domains for climate simulations or numerical weather predictions. The model uses a staggered regular latitude-longitude Arakawa C-grid in the horizontal, although this grid is rotated in regional runs such that the model domain is centred on the

Figure 2.4: The 25 m antenna of the Chilbolton Advanced Meteorological Radar (CAMRa) located at the Chilbolton Observatory.

equator of the grid for maintaining a consistent grid length. In the vertical, the model employs Charney-Phillips staggering (Charney and Phillips, 1953) implemented on a terrain-following height coordinate system.

The MetUM uses a set of parametrisations, including the radiation scheme from Edwards and Slingo (1996), the single moment microphysics scheme from Wilson and Ballard (1999), the Joint UK Land Environment Simulator (JULES) surface exchange scheme (Best et al., 2011), and a scale-aware non-local one-dimensional boundary-layer scheme (Boutle et al., 2014a; Lock et al., 2000) that treats vertical mixing in turbulence. Radiative impact of cloud water and total ice and snow is handled by the radiation scheme (Manners et al., 2018).

2.4.1 Global Model

In Chapters 3 and 4, we use outputs of the global configuration of the MetUM (Met Office, 2016) in determining the environmental freezing level used in the detection of Z_{DR} columns from the radar composite. With a spatial resolution of approximately $0.234^\circ \times 0.153^\circ$ of latitude and longitude, the available global model output provides available three-hourly forecasts at standard pressure levels initialised every 12 hours. The initial state of each run of the global model is determined using a hybrid 4D-Var data assimilation scheme.

Mittermaier and Illingworth (2003) showed that the MetUM predicts the freezing height with a root-mean-square error of 147 m and a bias of 15 m by verification with a vertically pointing cloud radar. This makes the MetUM appropriate for determining the freezing height for use in the detection of vertical features within the 3D radar composite with a vertical resolution of 500 m.

2.4.2 Regional Model

For the regional simulations used in this project, the mass-flux convection scheme by Gregory and Rowntree (1990) is switched off to allow explicit convection. Although the regional simulations are kilometre and sub-kilometre scale, the MetUM employs one of several cloud fraction schemes to represent subgrid humidity and carry out condensation of liquid. The regional model also implements a subgrid mixing scheme described in Hanley et al. (2019).

A modelling suite was set up to perform regional MetUM simulations. In a Rose suite[1] running version 13.0 of the MetUM, using the ENDGame formulation for the dynamical core and running on the Met Office XC40 Cray supercomputer. The suite will first use archived global model data to drive a 1.5km horizontal resolution run covering most of England. This is then used to initialise a simuation of 300m horizontal resolution covering a smaller domain nested within the 1.5km simulation. Lateral boundary conditions for the nested simulation are derived from the preceding resolution at hourly intervals. In other words, the driving model updates boundary conditions for the 1.5km simulation, in turn updating the boundary conditions for the 300m simulation. Despite only utilising 300m simulation outputs in this study for the purposes of understanding Z_{DR} representation, the 1.5km runs are needed to provide appropriate boundary conditions in such a one-way nested suite. It would also be computationally infeasible to significantly extend the 300m domain to cover the entirety of the UK. Figure 2.5 shows the locations of these nested domains and their coverage of England. These simulations are run with 70 vertical levels and a

[1]Developed by the Met Office, Rose is a group of utilities which provide a way to manage the development and running of scientific application suites in research and production environments.

fixed model lid at 40 km above sea level. 61 levels are below 18 km with heights that depend on the model orography. The topmost 9 levels are flat. Figure 2.6 shows the heights of the model levels above the land or sea surface of the model. Table 2.1 details the two model resolutions, domain sizes and number of grid points.

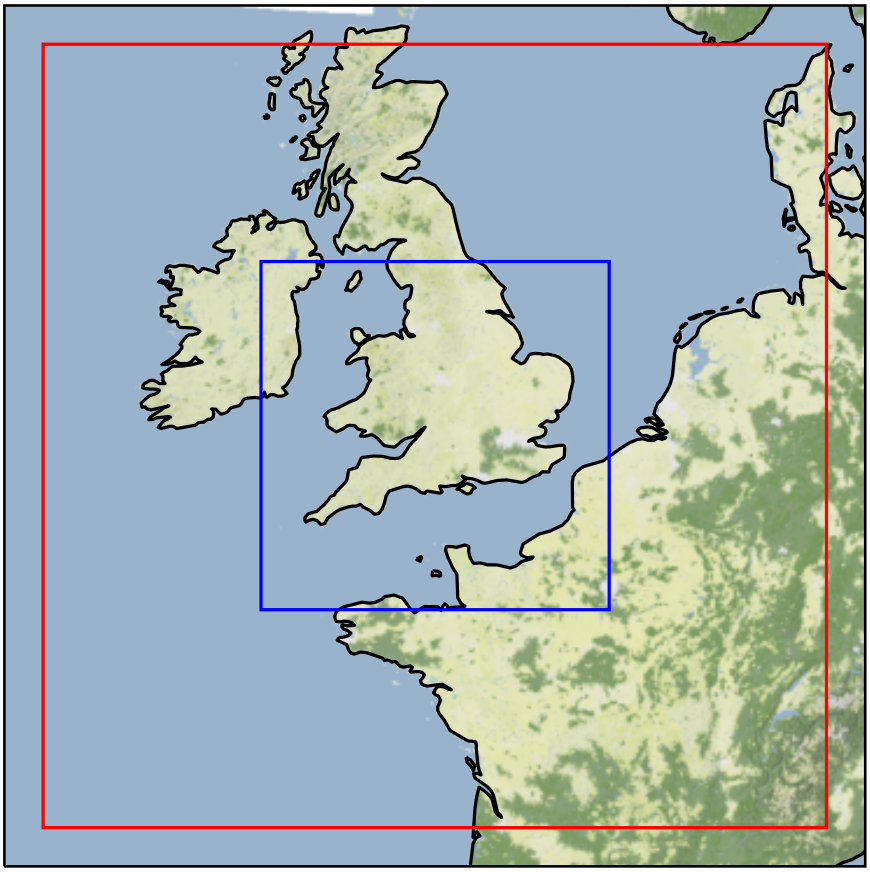

Figure 2.5: Model domain of the 1.5 km (red) and 300 m (blue) resolution MetUM simulations. Background colour on land depicts crowd-sourced terrain data by Stamen Design. Map tiles by Stamen Design, under CC BY 4.0. Data by OpenStreetMap, under ODbL.

Model	Latitude-longitude grid points	Domain size
1.5 km	2000 × 2000	3000 × 3000 km
300 m	2000 × 2000	600 × 600 km

Table 2.1: Overview of the model grid points and domain sizes for the model domains displayed in Figure 2.5.

In Chapter 6, a number of regional atmosphere model configurations will be evaluated. The first configuration implements the RA2M configuration used in the operational high-resolution NWP model (UKV) and the other implements the RAL3.1

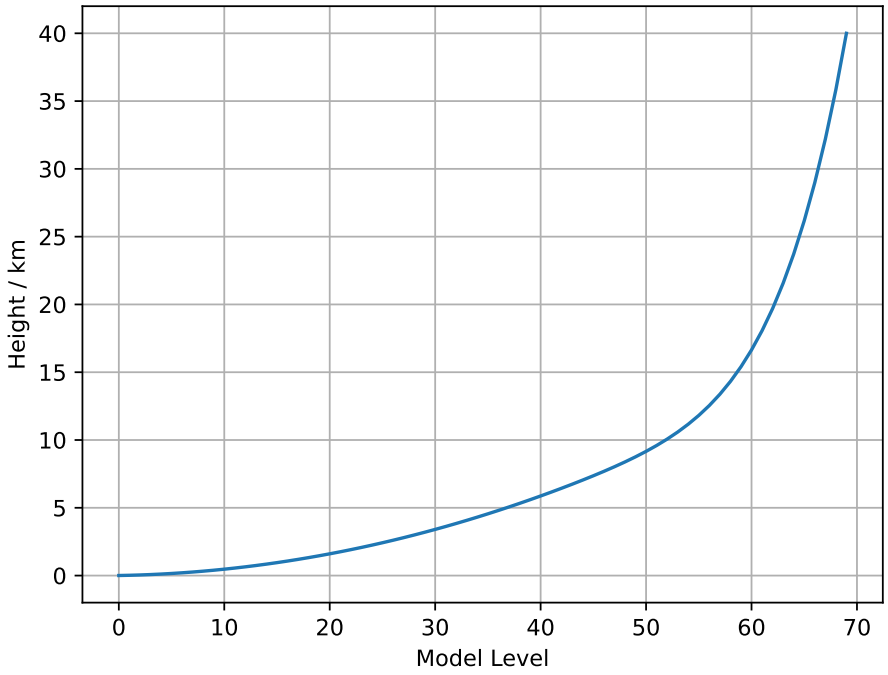

Figure 2.6: Model height against model level number. The lowest level of the model, level zero, is five metres above the surface. The highest model level is at 40km.

near-operational configuration. RA2M uses the Smith (1990) cloud scheme with other model physics already described above. RAL3.1 is a new physics configuration that implements double moment microphysics and uses a BiModal diagnostic partial cloud cover scheme. Some other major differences include the use of a unified mid-latitude and tropical configuration for turbulent mixing and the removal of stochastic boundary later perturbations, in contrast to RA2M. A major research question in this thesis regards the sensitivity of representation of Z_{DR} columns to choices of microphysics configuration. Therefore, principal processes are further described next.

2.4.3 Wilson-Ballard Microphysics

The current operational MetUM cloud microphysics scheme is a single moment scheme with four phases, which are cloud water and three hydrometeor classes. In the liquid phase, cloud water q_{cl} and rain q_R mass mixing ratio are prognosed. Frozen hydrometeors are represented by ice water content in a grid box, which is split into aggregates and ice crystal categories. These categories are treated separately when carrying out the microphysical transfers. The option of including graupel as a separate prognostic variable is usually available in higher resolution simulations of the MetUM and operationally since 2013.

The transfer of moisture from one species to another occurs through parametrised

microphysical processes. The focus of this thesis is on the contribution of rain to Z_{DR} columns. The source and sink terms for rain mass mixing ratio is shown in the transfer equation, Equation (2.2). The operator $\frac{D}{Dt}$ is the material derivative following an air parcel, i.e. $\frac{D}{Dt} \equiv \frac{\partial}{\partial t} + u_j^a \frac{\partial}{\partial x_j}$, where u_j^a is the j-th component of velocity of the air parcel. The superscript a explicitly denotes that the velocity is of the air parcel and not of the hydrometeor classes. The first term $SEDR$ describes the sedimentation of rain, which is implemented as the advection of rain mass to and from grid points above and below the grid point of interest. The process of autoconversion from cloud water ($RAUT$) simulates the collision of cloud droplets with each other, which coalesce to form drizzle drops. The collection of cloud water ($RACW$) describes the process of liquid cloud being collected by rain when raindrops fall, collide with and then coalesce with cloud drops in the direct fall lines of the raindrops. The melting of snow ($SMLT$), ice ($IMLT$) and graupel ($GMLT$) into raindrops also contribute to rain mass. Loss of rain mixing ratio could be from evaporation of rain to water vapour ($REVP$) in a sub-saturated environment. Rain mass could also be decreased via raindrops captured by snow ($SACR$) or ice crystals ($IACR$). The letter "A", "C" and "G" after the hyphen denotes that the collection process contributes to snow, ice and graupel respectively. The production of graupel depends on whether the increased graupel production scheme is switched on within the microphysics scheme. To simulate homogeneous ice nucleation ($IFRR$), all rain mass is frozen into ice at temperatures instantaneously at air temperatures less than $-40\,^{\circ}\mathrm{C}$.

$$\begin{aligned}\frac{Dq_R}{Dt} =& P_{SEDR} \\ &+ P_{RAUT} + P_{RACW} + P_{SMLT} + P_{IMLT} + P_{GMLT} \\ &- (P_{REVP} + P_{SACR-A} + P_{SACR-G} + P_{IACR-C} \\ &+ P_{IACR-G} + P_{IFRR})\end{aligned} \tag{2.2}$$

2.4.4 CASIM

The cloud microphysical scheme within the RAL3.1 configuration is the Cloud AeroSol Interacting Microphysics (CASIM) scheme. CASIM within the MetUM is a bulk double moment microphysics scheme and represents microphysical processes and aerosol-cloud interactions across spatial and temporal scales. The scheme was proposed to be adopted for operational use in 2023 (Field et al., 2023).

CASIM represents cloud by using five hydrometeor species, namely cloud liquid, rain, ice, snow, and graupel. These species are all specified by two prognostic moments, namely the mass mixing ratio and species number concentration. In con-

trast with Wilson-Ballard, CASIM also represents aerosol activation, ice nucleation processes, and in-cloud mechanical processing of aerosol.

The transfer of rain mass mixing ratio and number concentration is in Equations 2.3 and (2.4) respectively. P terms describe mass mixing ratio rates, whereas N terms describe number concentration rates. The first term in both equations (sedr) describes the sedimentation of rain. The process of autoconversion from cloud water into rain is described in the (raut) terms. The collection of cloud water by rain and ice by rain are described by the (racw) and (raci) terms respectively in the mass transfer equation. The shedding of rain drops from graupel undergoing wet growth (gshd) is only included in the number concentration transfer equation. Likewise, the collection of raindrops by other raindrops (racr) is only included in the number concentration transfer equation. The melting of snow (smlt) and graupel (gmlt) into raindrops contribute to rain mass. Loss of rain mixing ratio could be from evaporation of rain to water vapour (revp) in a sub-saturated environment. Rain mass could also be decreased via raindrops captured by snow (sacr) or graupel (gacr). The (homr) term simulates immersion freezing of rain into ice.

$$\begin{aligned}\frac{Dq_{\mathrm{r}}}{Dt} =& P_{\mathrm{sedr}} + P_{\mathrm{raut}} + P_{\mathrm{racw}} + P_{\mathrm{smlt}} + P_{\mathrm{gmlt}} \\ & - P_{\mathrm{revp}} - P_{\mathrm{raci}} - P_{\mathrm{sacr}} - P_{\mathrm{gacr}} - P_{\mathrm{homr}}\end{aligned} \tag{2.3}$$

$$\begin{aligned}\frac{Dn_{\mathrm{r}}}{Dt} =& N_{\mathrm{sedr}} + N_{\mathrm{raut}} + N_{\mathrm{gshd}} + N_{\mathrm{smlt}} + N_{\mathrm{gmlt}} \\ & - N_{\mathrm{revp}} - N_{\mathrm{sacr}} - N_{\mathrm{gacr}} - N_{\mathrm{homr}} - N_{\mathrm{racr}}\end{aligned} \tag{2.4}$$

2.4.5 Comparing rain processes in Wilson-Ballard with CASIM

Sedimentation

In Wilson-Ballard, the fall of raindrops into or out of a model grid box is the flux divergence of the rain mass across the layer in each model column. The numerical solution is not straightforward because of potentially long timesteps in the model, such that rain is able to fall through several model levels in a single timestep. This is especially the case in the lower levels of the model domain because of the narrowing of level spacing in the vertical.

A modified gamma distribution weighted by a power of ratio of air density to reference density is used to describe terminal fall speeds of raindrops. The increment

for rain mass mixing ratio q_R due to rain sedimentation is

$$P_{\text{sedr}} = \frac{R_{mf}}{\rho \Delta z} - q_R \frac{\overline{V_{Rm}}}{\Delta z} \tag{2.5}$$

where ρ is air density, Δz is layer thickness, R_{mf} is the rain mass flux from above and $\overline{V_{Rm}}$ is the mass-weighted mean of terminal fall speed.

In CASIM, sedimentation of rain mass is treated the same way. The increment of rain number concentration is done similarly but by replacing the rain mass flux by rain number flux R_{nf}, and using number-weighted mean of terminal fall speed $\overline{V_{Rn}}$ instead.

$$N_{\text{sedr}} = \frac{R_{nf}}{\rho \Delta z} - n_R \frac{\overline{V_{Rn}}}{\Delta z} \tag{2.6}$$

Autoconversion

Autoconversion is the process of initiating drizzle via coalescence of small cloud drops. Wilson-Ballard implements a power-law formulation that depends on cloud water content q_{cl} and drop concentration n_{cl}. The parameters characterising the rate of autoconversion are based on Khairoutdinov and Kogan (2000), derived by applying the least-squares method to minimize the mean square error between 100,000 drop spectra obtained from four large-eddy simulations and the bulk-parametrised autoconversion rate.

$$P_{RAUT} = 1350 E\left(f_{cl}\right) q_{cl}^{2.47} n_{cl}^{-1.79} \tag{2.7}$$

where n_{cl} is in cm^{-3}. The factor E, introduced by Boutle et al. (2014b), parametrises subgrid variability, which is a function of cloud water fraction in a grid encoded within f_{cl}. There is also a minimum threshold liquid water content q_{cl0} for autoconversion to occur. The default threshold for q_{cl0} is defined as the liquid water content such that the number concentration of particles of radii 20 µm or larger is $1000\,\text{m}^{-3}$.

CASIM has the same autoconversion parametrisation. Number tendency of rain mass due to autoconversion is

$$N_{\text{raut}} = \frac{P_{\text{raut}}}{c_r \frac{\mu_{\text{aut}}}{3.0} D_{0\text{aut}}^3} \tag{2.8}$$

where c_r is $\frac{\pi}{6}\rho_w$, $D_{0\text{aut}}$ is the diameter at which drizzle drops are produced in Khairoutdinov and Kogan (2000) and μ_{aut} is a diagnostic evaluation of the cloud shape parameter based on Martin et al. (1994).

Accretion

Raindrops grow by sweeping out cloud droplets in a process termed accretion. The rate that liquid cloud is collected by rain would depend on the sweep out rate of rain, the mass concentration of liquid cloud and the collision efficiency between liquid cloud droplets and that with raindrops. Rather than considering these terms individually, the process rate in Wilson-Ballard is parametrised by the formulation of Khairoutdinov and Kogan (2000), bias corrected following Boutle et al. (2014b).

$$P_{RACW} = 67E\left(f_{cl}, f_R, \rho\right) q_{cl}^{1.15} q_R^{1.15} \tag{2.9}$$

The factor E is a function of cloud water and rain fraction in a grid encoded within f_{cl} and f_R respectively. The parameter ρ is the correlation coefficient between the cloud water content q_{cl} and rain water content q_R. CASIM treats accretion of cloud water by rain the same way.

However, the collection of ice by rain process to form graupel in CASIM is instead represented by a simple gravitational sweepout for relatively small fall speeds. If mass of ice collected by rain is smaller than $1 \times 10^{-5}\,\mathrm{kg\,kg^{-1}}$, then only snow is produced. The process is not temperature sensitive within CASIM, as ice is not usually found below the melting layer in the model.

$$P_{\mathrm{raci}} = \frac{\pi n_r a_r \Gamma\left(3 + b_r + \mu_r\right) E_{ri} q_i}{4\left(\lambda_r\right)^{3+b_r+\mu_r}} \left(\frac{\rho_0}{\rho}\right)^{g_r} \tag{2.10}$$

where n_r is the number concentration mixing ratio of rain r, q_i is the mass mixing ratio of ice, E_{ri} is the collection efficiency, a_r, b_r and g_r are parameters describing the terminal velocity of raindrops, μ_r is shape parameter of the particle size distribution of rain, and $\rho_0 = 1.22\,\mathrm{kg\,m^{-3}}$ is a reference value of air density. Values of these parameters can be found in Appendix A of Field et al. (2023).

Graupel Shedding

CASIM models the increase in raindrop concentration due to graupel shedding liquid water whenever the mass tendency of graupel accretion by cloud water is negative. In other words, the rate of wet growth is:

$$N_{\mathrm{gshd}} = \frac{P_{\mathrm{gacw}}}{c_r D_{0\mathrm{melt}}^3} \tag{2.11}$$

where c_r is a mass-dimension parameter for rain set to 522, and $D_{0\mathrm{melt}} = 1\,\mathrm{mm}$ is the assumed mean diameter of raindrops from the shedded melt water. This microphysical process is not included in Wilson-Ballard.

Melting

If the ambient temperature is warmer than frozen surface of snow, heat conduction through air and from condensation will contribute to the latent heat required for melting. In Wilson-Ballard:

$$L_f \frac{dM_{\text{melt}}}{dt} = -2\pi D K_a T_c F' + 2\pi D L_v \psi \rho \left(q - q_{0sat}\right) F' \tag{2.12}$$

where L_f and L_v are the latent heats of fusion and vapourisation respectively. D is the diameter of the snow particle. K_a and ψ are the thermal conductivity of air and the diffusivity of water vapour in air respectively. T_c is air temperature in celsius. ρ is air density. F' is the ventilation coefficient. Here, q_{0sat} is the saturation mixing ratio at 0 °C. Integrating over all particle diameters, and ignoring corrections due to the sensible heat associated with accreted liquid water, the melting of snow to form rain is

$$P_{SMLT} = \frac{1}{\rho L_f} \left(K_a T_c - L_v \psi \rho \left(q - q_{0sat}\right)\right) \times \mathcal{V}_s \tag{2.13}$$

$\mathcal{V}_s$ is the integrated ventilation factor for spherical snow particles with a generalised gamma distribution of particle sizes.

The melting of ice and graupel to form rain is similar, except with different parameter values. $\mathcal{V}_i$ and $\mathcal{V}_g$ being the integrated ventilation factor for ice and graupel respectively. The derivation of these ventilation factors can be found in Appendix A of Field et al. (2023).

$$P_{IMLT} = \frac{1}{\rho L_f} \left(K_a T_c - L_v \psi \rho \left(q - q_{0sat}\right)\right) \times \mathcal{V}_i \tag{2.14}$$

$$P_{GMLT} = \frac{1}{\rho L_f} \left(K_a T_c - L_v \psi \rho \left(q - q_{0sat}\right)\right) \times \mathcal{V}_g \tag{2.15}$$

Melting is treated similarly in CASIM, but with an extra term considering the heat contribution from other accretion processes when liquid is cooled to the freezing temperature.

$$P_{\text{smlt}} = \frac{1}{\rho L_f} \left(K_a T_c - L_v \psi \rho \left(q - q_{0sat}\right)\right) \times \mathcal{V}_s + \frac{c_w T_c}{L_f} \left(P_{\text{sacw}} + P_{\text{sacr}}\right) \tag{2.16}$$

$$P_{\text{gmlt}} = \frac{1}{\rho L_f} \left(K_a T_c - L_v \psi \rho \left(q - q_{0sat}\right)\right) \times \mathcal{V}_g + \frac{c_w T_c}{L_f} \left(P_{\text{gacw}} + P_{\text{gacr}} - P_{\text{gshd}}\right) \tag{2.17}$$

where c_w is the specific heat of liquid water. Unlike Wilson-Ballard, CASIM does not model the mass transfer of ice melting into rain.

The number concentration rates from snow or graupel to rain due to these pro-

cesses are assumed to be

$$N_{\text{smlt}} = P_{\text{smlt}} \frac{n_s}{q_s} \tag{2.18}$$

$$N_{\text{gmlt}} = P_{\text{gmlt}} \frac{n_g}{q_g} \tag{2.19}$$

Evaporation

The evaporation rate of rain occurs in air that is sub-saturated with respect to liquid water, i.e. $q < q_{wsat}$. In Wilson-Ballard,

$$P_{REVP} = \frac{\left(\frac{q}{q_{wsat}} - 1\right)}{\rho \text{AB}_{liq}} \times \mathcal{V}_r \tag{2.20}$$

where ρ is air density and $\mathcal{V}_r$ is the integrated ventilation factor for raindrops. The term in the denominator is

$$\text{AB}_{liq} = \left(\frac{L_v}{R_v T} - 1\right) \frac{L_v}{K_a T} + \frac{R_v T}{\psi e_{satliq}} \tag{2.21}$$

where L_v is the latent heat of vaporisation, R_v is the gas constant for water vapour, and e_{satliq} is saturation vapour pressure.

CASIM treats evaporation of rain the same way. In terms of number concentration, the inhomogeneous assumption is made such that

$$N_{\text{revp}} = P_{\text{revp}} \frac{n_r}{q_r} \tag{2.22}$$

In other words, the evaporation of rain maintains the mean size of raindrops.

Collection

In both Wilson-Ballard and CASIM, the rate of collision between the rain and snow categories is parametrised as a double integration, which takes into account the spectrum of sizes of particles of each category.

A similar approach is used for the number concentration tendency within CASIM.

CASIM also parametrises self-collection processes, which are process rates for the collection within a hydrometeor type. This type of collection will only impact the number concentration and will have no impact on the mass of the hydrometeor type. The self-collection of rain is

$$N_{\text{racr}} = -8 E_{rr} n_r q_r \rho \tag{2.23}$$

where E_{rr} is the collection efficiency with units $\text{m}^3\,\text{kg}^{-1}$.

Homogeneous freezing

In Wilson-Ballard, all rain at temperatures less than $-40\,^{\circ}\mathrm{C}$ is instantaneously frozen to form ice particles.

There is no homogeneous freezing of rain in CASIM. The process is instead replaced by the heterogeneous rain freezing process described below.

Heterogeneous freezing

Not considered in Wilson-Ballard, immersion freezing of raindrops to form graupel is based on Bigg (1953), who showed that the probability of a raindrop of diameter D freezing per unit time is

$$\frac{\pi}{6} D^3 B_B \left(e^{-A_B T_c} - 1\right) \tag{2.24}$$

where A_B and B_B are parameters determined from laboratory experiment, T_c is temperature in celsius. The rates of freezing of rain into graupel are in CASIM.

$$P_{\mathrm{homr}} = n_{0r} \frac{\pi B_B}{6\rho} c_r \left(e^{-A_B T_c} - 1\right) \frac{\Gamma\left(4 + d_r + \mu_r\right)}{\lambda_r^{4+d_r+\mu_r}} \tag{2.25}$$

$$N_{\mathrm{homr}} = n_{0r} \frac{\pi B_B}{6\rho} \left(e^{-A_B T_c} - 1\right) \frac{\Gamma\left(4 + \mu_r\right)}{\lambda_r^{4+\mu_r}} \tag{2.26}$$

where the drop size distribution shape parameter μ_r is 2.5, and the mass-dimension parameter d_r is 3. n_{0r} is the intercept parameter of the drop size distribution.

2.4.6 Rain microphysical variables

To explore the behaviour of both schemes, Figures 2.7a and 2.7b show joint distributions of rain mass fraction q_{rain} and rain number concentration n_{rain} for a single output from a 300 m MetUM simulation coupled to the Wilson-Ballard scheme and CASIM respectively. The relevant case study is further described in Chapter 6.

The number concentrations in the Wilson-Ballard simulation are diagnosed from the rain drop size distribution and number intercept parametrisation described in Abel and Boutle (2012), rather than prognosed by the model as in the CASIM simulations. Thus, the simulations using Wilson-Ballard single moment scheme contain grid points mostly limited to a power law relationship between n_{rain} and q_{rain}, where $n_{\mathrm{rain}} \sim q_{\mathrm{rain}}^{-\frac{2}{3}}$.

Prognosed q and n from RAL3.1 occupies a much larger amount of parameter space. The mode at around $q_{\mathrm{rain}} = 1 \times 10^{-4}\,\mathrm{kg\,kg^{-1}}$ and $n_{\mathrm{rain}} = 1 \times 10^{3}\,\mathrm{kg^{-1}}$ is mostly present for grid points in warm levels of the model. This can be explained by the melting or accretion of frozen hydrometeors into rain at temperatures warmer

than freezing. A more subtle mode of grid points is present for lower q_{rain} between 1×10^{-8} and $1 \times 10^{-6}\,\text{kg}\,\text{kg}^{-1}$. This is likely due to the autoconversion of liquid cloud to rain, where $N_{\text{raut}} \sim P_{\text{raut}}$.

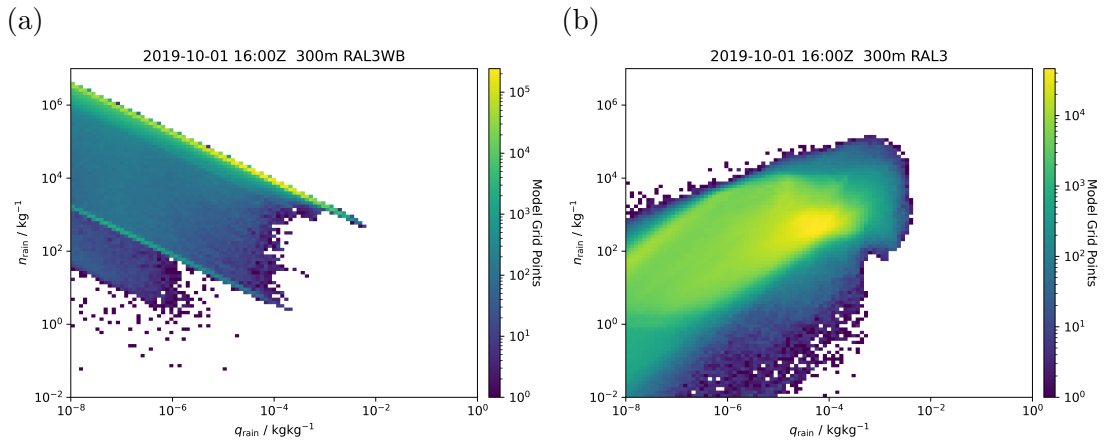

Figure 2.7: Joint distributions of rain drop number concentration per kilogram of air and rain mass fraction from simulations coupled to (a) Wilson-Ballard and (b) CASIM, valid on 01 Oct 2019 at 1600Z.

The joint distributions of microphysics variables between the microphysical schemes reflect the effect between parametrising the intercept parameter of the rain drop size distribution and prognosing it. The Wilson-Ballard runs limit grid points to a narrow n and q distribution, whereas CASIM exhibits a considerably wide spread of n and q.

Chapter 3

Verifying Z_{DR} in the 3D radar composite against CAMRa RHIs

3.1 Introduction and aims

The purpose of this work chapter is to verify Z_{H} and Z_{DR} generated by the Met Office compositing process against range-height indicator (RHI) scans from CAMRa. This is done to increase confidence that Z_{DR} signatures represented in the 3D radar composite are real, assuming CAMRa acts as truth. The radar composite has wide spatial coverage of the UK and is available every five minutes, which makes it suitable for nowcasting (Chapter 4) and model evaluation (Chapter 6). Stein et al. (2020) evaluated Z_{H} echo top heights between collocated RHIs from CAMRa and those derived from the radar composite for cases of convection, but the evaluation of Z_{DR} is yet to be explored. Z_{DR} columns are often narrow features that may challenge the limited resolution of the radar composite.

CAMRa is a suitable truth owing to it being well-calibrated to within 0.1 dB of Z_{DR}, its extremely narrow beamwidth of 0.28°, high range resolution of 75 m and high resolution elevations of 0.11° within RHIs. In contrast, the composite is made of operational radar data of low resolution and the compositing process could further degrade the accuracy of the data and thus its Z_{DR} output has to be verified. However, the pre-existing 3D composite did not include Z_{DR}, which meant that the radar composite had to be extended to include Z_{DR} as described in Chapter 2.

Another challenge is that the composite's three-dimensional output is not normally collocated with CAMRa scans. CAMRa has differing spatial resolutions and vertical coverage compared to the radar composite, but there is also the problem of temporal mismatch between the usual composite output every five minutes and the scan time of the CAMRa RHI. The mentioned issues are resolved by preparing C-band radar composites that are interpolated to grid points along the CAMRa azimuth, including all C-band radar data at each scan elevation that are within a

few minutes of the time the CAMRa scan was made. CAMRa scans also undergo a regridding to share the same spatial resolution as the composite.

To evaluate the realism of Z_{DR} representation within the radar composite to determine how accurate it is and features that it captures, a visual verification of Z_{DR} columns is carried out in Section 3.2. This analysis identified a serious misplacement between scans from different radars, which is fixed as part of the work in this thesis. Section 3.2 also briefly summarises the issue and the fix. A quantitative statistical analysis of Z_{H} and Z_{DR}, including their relationships is detailed in Section 3.3. Finally, a summary (Section 3.4) concludes this chapter.

3.2 Vertical cross sections of the radar composite

Figures 3.1a and 3.1d are RHI scans carried out by CAMRa, covering elevations from 0.02 to 10.0°. These two figures captured an evolving convective system on 7 June 2016 at 1651Z (Figure 3.2e) and on 1 October 2019 at 1526Z (Figure 3.2f). The fine range resolution of 75 m captured multiple intense reflectivity cores exceeding 40 dBZ with accompanying overshooting tops.

Figures 3.1b and 3.1e are pseudo-RHIs produced from the compositing process of the Chenies and Thurnham operational C-band radars. Both radars were chosen for the compositing process as their overlapping sampling regions offered coverage for the convective system scanned by CAMRa. Instead of generating the usual 3D composite with 1 km and 500 m of horizontal and vertical grid spacing respectively, the compositing software was modified as part of the work in this thesis to interpolate C-band radar data onto a 2D grid along the CAMRa scan azimuth with the same grid resolutions thus producing the so-called pseudo-RHI plots.

However, the preliminary inspection of the pseudo-RHI plots reveals two issues; the first being coarse spatial resolution at higher heights and the second being vertical discontinuity of interpolated data.

The first issue arises from the low elevation scan strategy employed operationally by the Met Office. Interpolated data at grid points at higher heights would have had originated from the highest elevation scans of radars at a long range. Considering the highest elevation angles are at 3.0 and 4.0°, vertically adjacent data from the same radar are separated by 2 km in the vertical at 100 km range at heights above 6 km as seen in Figure 2.2. This issue will be addressed later when CAMRa data is compared to pseudo-RHIs.

The second issue is more serious, as vertical discontinuities could disrupt the automatic detection of vertically extending signatures such as Z_{DR} columns. This problem is seen at around 70 and 100 km down range in Figure 3.1b and 90 km

down range in Figure 3.1e. The displacement observed here suggests that the spatial location of storms could be misrepresented on the order of 5 km.

3.2.1 Correction of spatial location of radar beams in compositing software

Through scrutiny of the Met Office compositing software, I found an error with how radar azimuths were used in the compositing process. In the pre-exisiting compositing software, radar ranges and beam elevations are converted to great circle distances relative to the radar antenna by assuming an equivalent Earth's radius of $\frac{4}{3}$ of the Earth's radius (Doviak and Zrnić, 1993). The great circle distances, beam heights and radar azimuths would be formulated as azimuthal equidistant projection coordinates relative to the radar site, then directly transformed onto British National Grid coordinates. However, it was overlooked that Met Office radar azimuths are recorded with respect to British National grid north, whereas azimuthal equidistant projection coordinates are relative to true north.

To fix this problem, grid convergence (Ordnance Survey, 2018) is added to all radar azimuths such that radar azimuths are adjusted with respect to true north before undergoing transformation into British National Grid coordinates. The Thurnham radar is situated at a location with a grid convergence of 2.0°, such that storms 100 km away from the radar could be displaced by 3.5 km if azimuthal correction is not applied.

The effect of implementing such a correction can be seen in Figures 3.1c and 3.1f, where reflectivity values interpolated from two separate C-band radars result in a vertically continuous intense reflectivity core. With the azimuth correction applied, the 3D radar composite is now ready for verification.

3.2.2 Visual comparison of Z_{DR}

Although it was mentioned in Chapter 2 that the complete operational network only acquired polarimetric capability in January 2018, both Chenies and Thurnham radars used for generating pseudo-RHIs were upgraded to have dual polarimetric capability since March 2013. This allows the generation of Z_{DR} pseudo-RHI plots as shown in Figures 3.2c and 3.2d, which can be qualitatively compared with CAMRa scans in Figures 3.2a and 3.2b on 7 June 2016 at 165136Z and on 1 October 2019 at 152641Z respectively. These two days selected were when CAMRa adopted a fine-scale scanning strategy, such that the RHIs were able to capture reflectivity cores and areas surrounding the cores. The two different chosen scan azimuths, at 27.1° and 325.6°, also allow testing of different areas of coverage within the radar

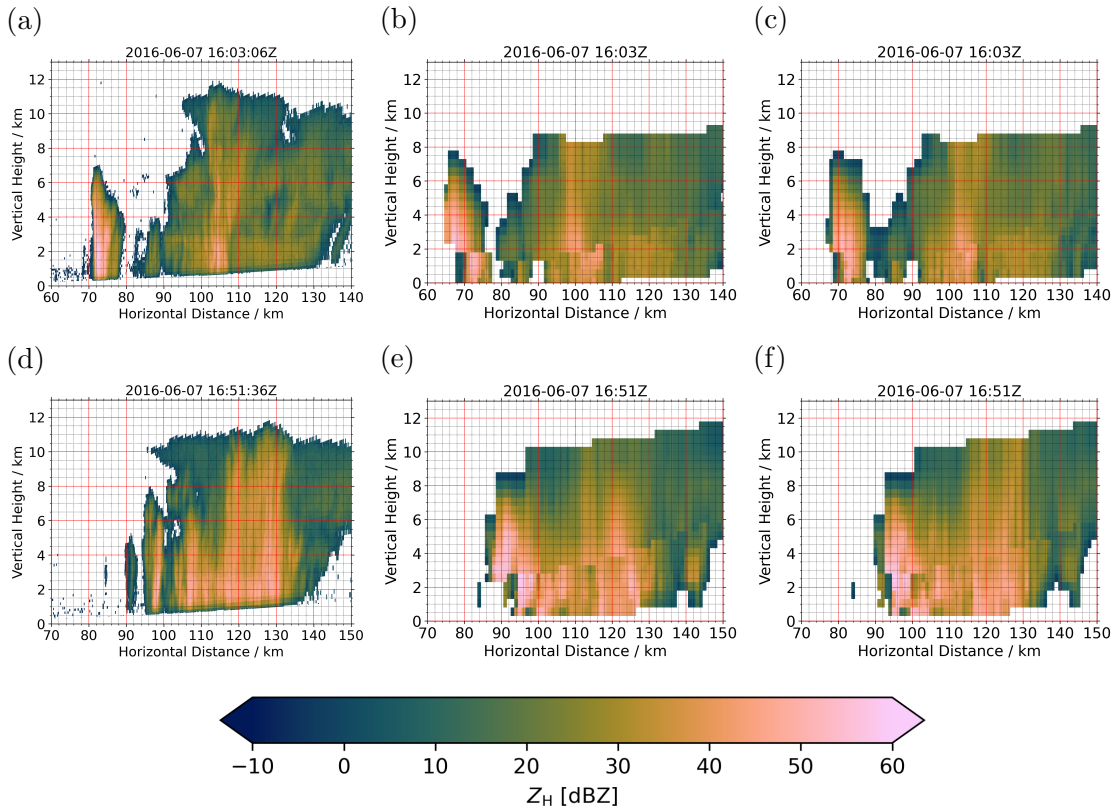

Figure 3.1: RHI plots of radar reflectivity Z_H scanned by CAMRa (a,d) and corresponding pseudo-RHI plots derived from the original Met Office radar compositing process (b,e) and with azimuthal correction applied (c,f). The top and bottom rows each corresponds to observations on 07 June 2016 but at 1603Z and 1651Z respectively.

composite.

Z_{DR} columns were observed by CAMRa at 97 and 56 km down range in Figure 3.2a and 3.2b respectively. The generated pseudo-RHIs also seem to capture the same Z_{DR} columns albeit with more intense Z_{DR} values that extend higher in height. An inspection of scans in the two minutes preceding the RHI in Figure 3.2a reveals observed Z_{DR} column properties change over relatively small scales. The first three panels in Figure 3.3 show scans taken every 30 seconds immediately before the RHI in Figure 3.2a at azimuths varying only by a few tenths of a degree. The Z_{DR} column is much more intense with a top reaching 5 km in Figures 3.3a and 3.3b scanned at 27.9 and 27.6° of azimuth respectively, similar to what is represented in the composite. This is in contrast to a much weaker column in Figure 3.3d scanned at 27.1° of azimuth. There is also some amount of differential attenuation behind the upper part of the column in the earliest scan.

Considering the observed Z_{DR} column is approximately 95 km down range from the radar, a displacement of 0.6° is 1 km of distance in the horizontal. Such a distance corresponds to the sampling resolution of the radar composite. The C-band operational radars also have a wider beamwidth of 1.1° and are unable to observe fine details unless the Z_{DR} column is situated close to one of the radars. Thus, the discrepancy in intensity and height in Figure 3.2 is expected, owing to the differences in sampling resolutions between CAMRa and the radar composite. The operational radar composite, which combines measurements from radars at various ranges, is capable of detecting Z_{DR} column features at a coarser resolution, whereas CAMRa is used to study fine details of the column structures with high precision in individual case studies.

3.3 Comparing regridded CAMRa data with radar composite

A comparison is made between high resolution CAMRa scans at the resolution of the pseudo-RHIs to see if the composite is consistent with sub-sampled data from CAMRa. Each CAMRa scan was linearly interpolated (in dB units) to the 1 km horizontal and 500 m vertical resolution grid used in the pseudo-RHI. An example of a regridded CAMRa scan is shown in Figure 3.4. The clutter within the first 40 km of CAMRa scans (not shown) is excluded from statistical analyses of Z_{H} and Z_{DR} values.

Despite having corrected C-band radar azimuths, there are still vertical discontinuities in the Z_{DR} field of the pseudo-RHIs. It is possible that there have been different amounts of Z_{DR} attenuation originating from different radars. There would

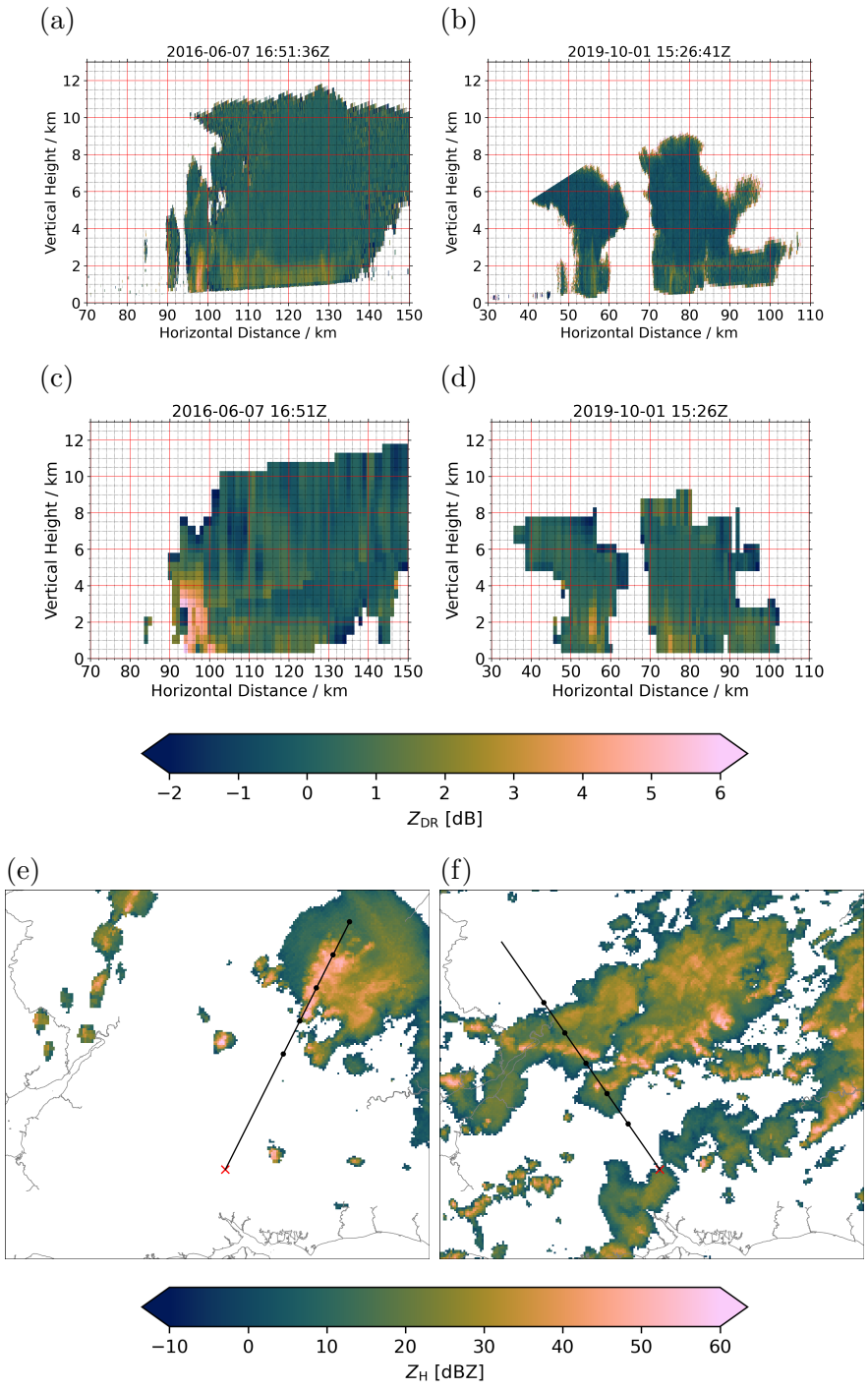

Figure 3.2: RHI plots of radar differential reflectivity Z_{DR} scanned by CAMRa (a,b), corresponding pseudo-RHI plots derived from the radar composite (c,d) and MAXDBZ plan views in (e,f). In the plan views, the red cross marks the position of CAMRa. The black line is the azimuth of CAMRa for the RHI scan. Black dots are separated by 20 km with the first and last black dot corresponding to the plotted range of the RHIs. The top and bottom rows each corresponds to observations on 07 June 2016 at 1651Z and 01 Oct 2019 at 1526Z respectively. The freezing height was 3.0 km in the June case and 2.2 km in the October case.

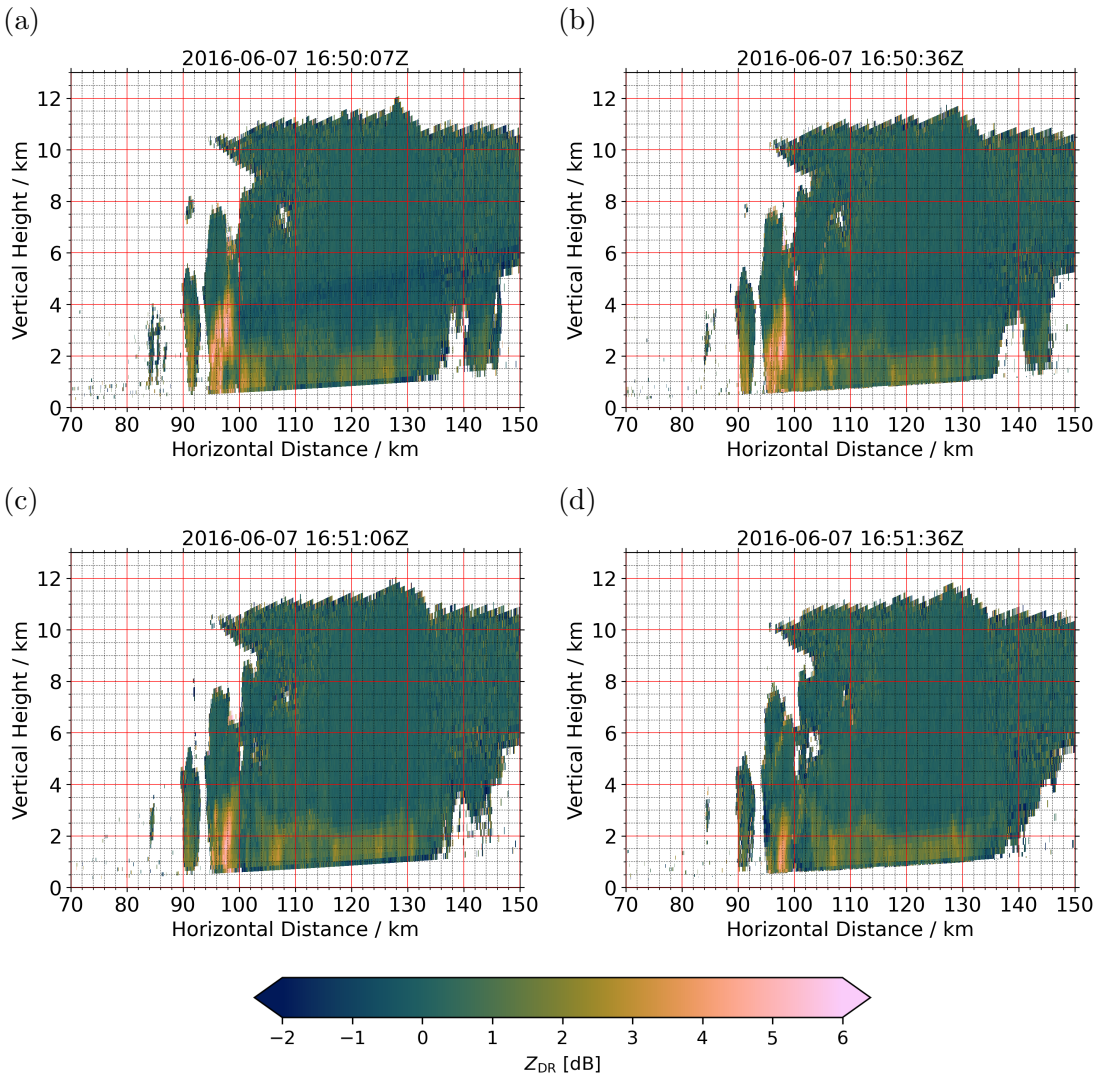

Figure 3.3: RHI plots of radar differential reflectivity Z_{DR} scanned by CAMRa on 07 June 2016 at (a) 165007Z, (b) 165036Z, (c) 165106Z, and (d) 165136Z at azimuth angles of 27.9, 27.6, 27.4 and 27.1° with respect to grid north respectively. Panel (d) is the same as Figure 3.2a and is duplicated here for easy comparison with other panels.

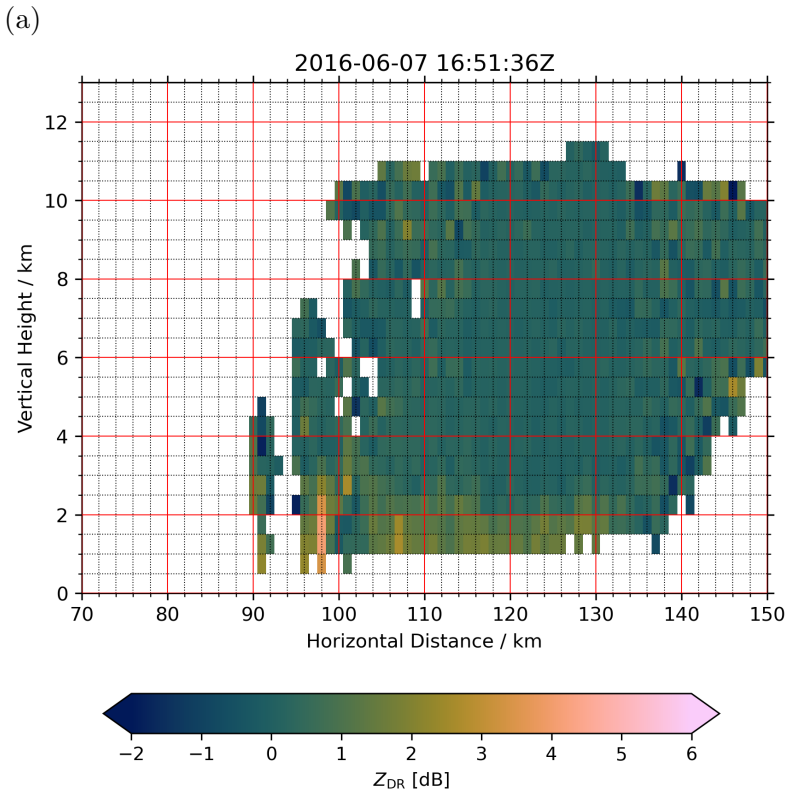

Figure 3.4: An example of a regridded RHI plot of radar differential reflectivity Z_{DR} scanned by CAMRa on 07 June 2016 at 1651Z.

also be time advection errors, which become more apparent in the Z_{DR} field where columns are narrower than Z_H cores. The cases presented cover convective storms that are rather heterogeneous in space with small scale features that will be sensitive to storm advection in time due to it being impossible for operational radar scans to occur simultaneously. In the three-dimensional version of the composite that covers a fixed domain, it is possible for time advection to be applied to reduce the error due to storm advection.

Classification of hydrometeors and a description of their microphysics can only be achieved with an accurate measurement of polarimetric radar variables. Joint distributions of Z_H and Z_{DR} will allow one to see the microphysics observed by CAMRa and pseudo-RHIs. For instance, we expect increasing oblateness with large liquid raindrops due to aerodynamic drag (e.g. Pruppacher and Beard, 1970). This corresponds to a positive correlation between Z_H and Z_{DR}. For tumbling hail, the resulting measured Z_{DR} is close to zero irrespective of hailstone size, as the stones statistically appear to be spherical (e.g. Aydin et al., 1986). This corresponds to radars sampling high Z_H but low Z_{DR}.

Figures 3.5a and 3.5c present joint distributions for 120 regridded CAMRa RHI scans on 07 June 2016 partitioned into grid points higher and lower than the freezing height respectively. This is done similarly for 120 corresponding composite-

generated pseudo-RHIs in Figures 3.5b and 3.5d. Below the freezing height, we observe similar Z_{H} and Z_{DR} distributions both in CAMRa and composite data as expected. The mode of Z_{DR} is 0 dB below Z_{H} of 25 dBZ, but this increases to 2 dB of Z_{DR} for Z_{H} above 40 dBZ. Figure 3.6b shows the median, 10 and 90th percentiles of Z_{DR} values in each Z_{H} bin for grid points below the freezing level. The positive curvature highlighted by the most populated bins resembles the microphysics of increasing oblateness of raindrops as they increase in size. Similar to the joint distributions, the median highlights a positive correlation between the two radar observables below the freezing height.

A subtle point to note is the maximum Z_{DR} values reach much higher values for the same Z_{H} in the composite compared to CAMRa. The median of CAMRa and the composite also differ by more than 1.0 dB for Z_{DR} larger than 2.0 dB. This is likely attributed to the manifestation of Mie resonance effects in C-band radars (Ryzhkov and Zrnic, 2005).

Histograms describing Z_{H} and Z_{DR} distributions above the freezing height are also of interest, as this is where we expect the occurrence of Z_{DR} columns, especially for grid points fulfilling $Z_{\mathrm{H}} \geq 10$ dBZ and $Z_{\mathrm{DR}} \geq 1.0$ dB as per the thresholds in Plummer et al. (2018). The branch of near zero Z_{DR} for large Z_{H} above the freezing level (Figures 3.5a and 3.5b) is a signature of tumbling hail and is also reflected by the near-zero median Z_{DR} for Z_{H} less than 45 dBZ (Figure 3.6a). A larger spread of Z_{DR} values at higher reflectivity in the pseudo-RHIs is possibly due to non-linear beam filling effects (Ryzhkov, 2007). At heights of 3 km, which is above the freezing level, a radar beam is at least 700 m wide. As already seen in Figure 3.2d, a shallow Z_{DR} column is broadened out to cover a greater depth of the cloud above the freezing height. This effect is much less severe in data from CAMRa, considering its beamwidth is nearly four times narrower.

3.4 Summary and conclusions

The Met Office C-band radar composite was verified against RHI scans carried out by CAMRa. Vertical discontinuities of approximately 5 km within composite-derived pseudo-RHIs revealed inconsistencies in the usage of grid north in describing C-band radar azimuths, which had to be corrected by adding grid convergence to radar azimuths respective to each individual radar site before compositing was done. The implemented correction was required for the verification work carried out in this chapter and the successful detection of Z_{DR} columns in later work chapters of this thesis. This bug has now been fixed in the operational 3D composite and will eventually be applied to nowcasting and radar data assimilation systems in the Met

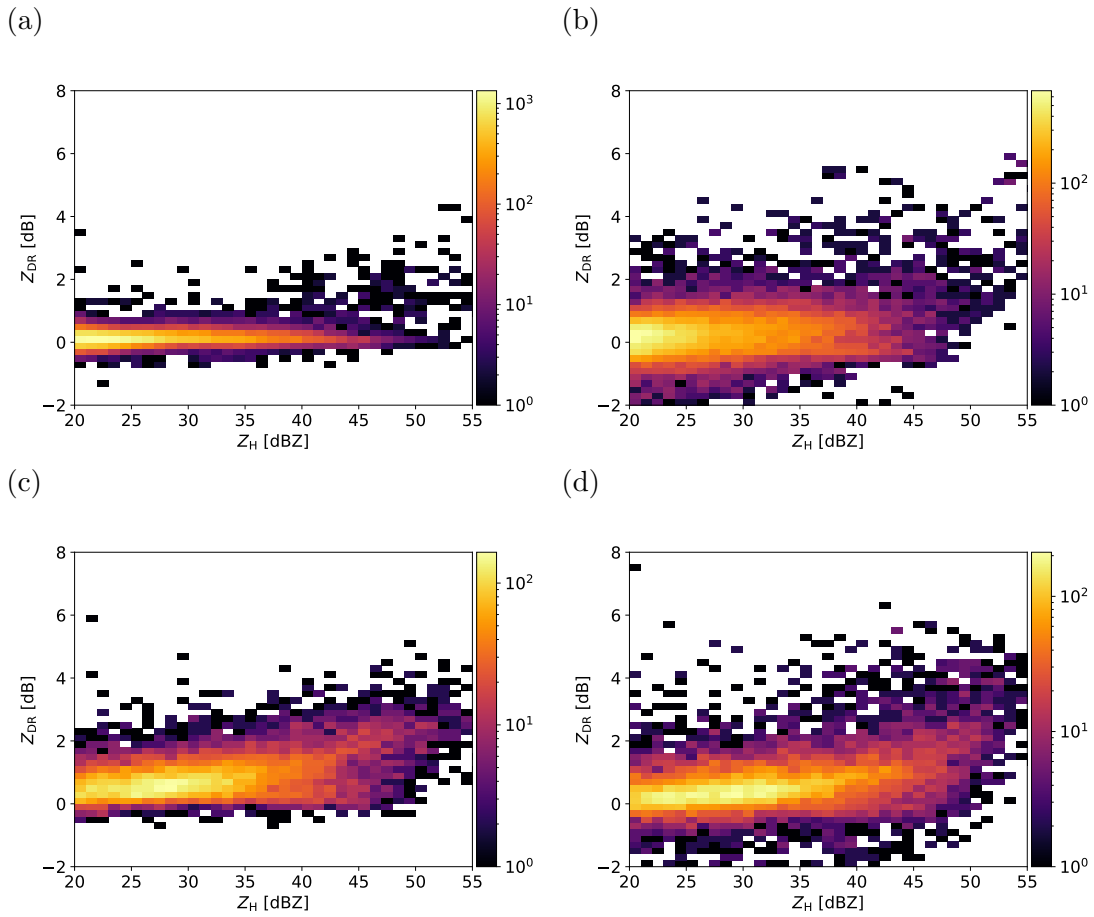

Figure 3.5: Joint distributions of Z_H and Z_{DR} for regridded CAMRa data (a,c) and composite-generated pseudo-RHIs (b,d) considering grid points above (top row) and below (bottom row) the freezing height. Note that the colour bar ranges are different for different panels.

(a)

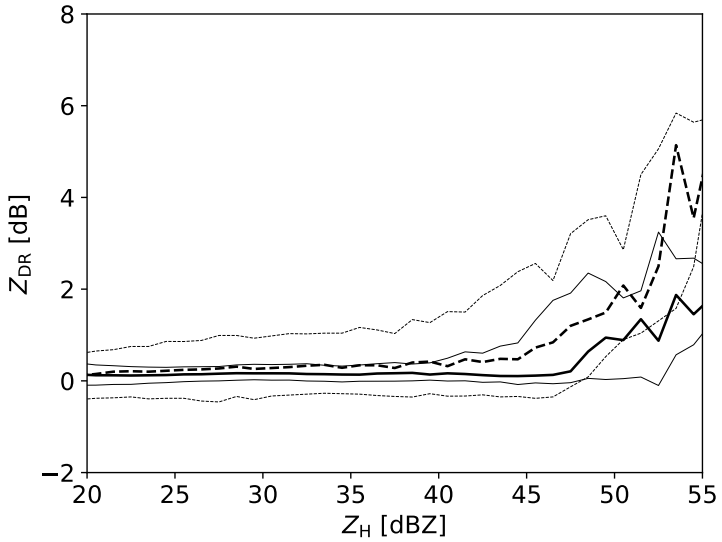

(b)

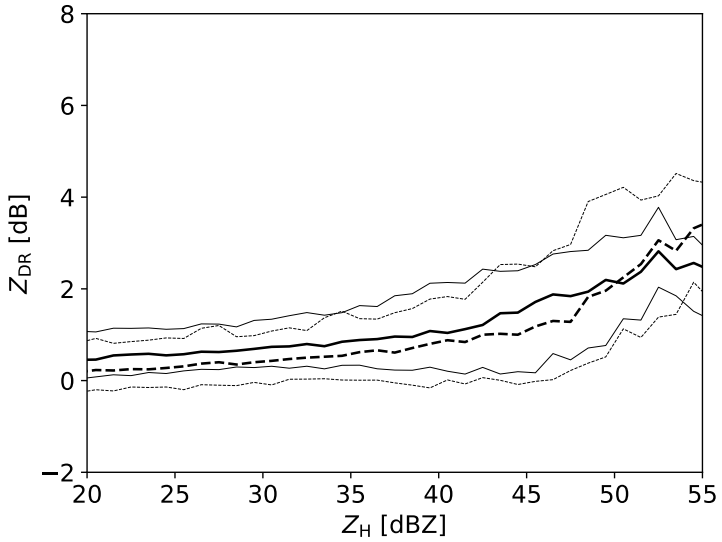

Figure 3.6: Median, 10 and 90-th percentile Z_{DR} values for each Z_{H} bin for grid points (a) above and (b) below the freezing height. Solid lines represent regridded CAMRa data, whereas the dotted lines represent composite data. Thicker lines show the median Z_{DR} values.

Office.

With the compositing process fixed, pseudo-RHIs were compared visually with CAMRa RHI scans. Reflectivity cores and Z_{DR} columns were collocated between the two types of observations. The heterogeneity of observations at km and sub-km scales could explain how Z_{DR} values are more intense in the composite at times with enhanced values extending deeper within convective cells. If a specific RHI is picked whereby the scan coincidentally targets the core of a Z_{DR} column, Z_{DR} values could be comparable with the composite-derived pseudo-RHIs also capturing the presence of the same Z_{DR} column. Due to the narrow nature of Z_{DR} columns and the fine beam of CAMRa, it is unsurprising for CAMRa to have sampled the edges of Z_{DR} columns to give lower Z_{DR} values than the radar composite.

Having resampled CAMRa scans to the same grid as the pseudo-RHIs, joint distributions of Z_{H} and Z_{DR} were investigated. The positive correlation between Z_{H} and Z_{DR} within the joint distributions showed that both radar observation sources could capture the presence of rain below the freezing height. Although the spread of Z_{DR} from the composite was larger than that from CAMRa for grid points higher than the freezing height, their median Z_{DR} were comparable to within 0.5 dB when both values were below 2.0 dB. The larger deviations at more extreme Z_{DR} values can be explained by the operational C-band radars affected by Mie resonance effects.

Outputs from CAMRa captured sub-kilometre features such as the width of Z_{DR} columns and their horizontal structures within a cell are too fine to be resolved by the composite. Despite the resolution limitations of operational radars, this work chapter has provided confidence that the radar composite can be exploited to reliably capture the presence of Z_{DR} columns at a horizontal spatial resolution of 1 km alongside an indication of their maximum heights.

Chapter 4

Use of Z_{DR} columns for early detection of severe convection within the operational radar network of the United Kingdom

This chapter is adapted from the following publication in *Meteorological Applications* with the following reference:

Lo, C. H. B., Stein, T. H. M., Scovell, R. W., Westbrook, C. D., Darlington, T., & Lean, H. W. (2024). Use of ZDR columns for early detection of severe convection within the operational radar network of the United Kingdom. Meteorological Applications, 31(1), e2159. https://doi.org/10.1002/met.2159

Estimated contribution: 80%. CHBL developed the methodology, performed all analysis and wrote the manuscript with input and suggestions from THMS and CDW. RWS provided the radar compositing code. THMS provided the storm tracking code. All authors commented on the manuscript and discussed the results at all stages. Two anonymous reviewers provided comments on earlier versions of the manuscript.

Abstract

Differential reflectivity (Z_{DR}) columns were observed using a Met Office three-dimensional radar composite. An algorithm for automatic detection of Z_{DR} columns was developed, based on $Z_{\mathrm{DR}} \geq 1.0\,\mathrm{dB}$ and $Z_{\mathrm{H}} \geq 10\,\mathrm{dBZ}$. Across three case days, detected Z_{DR} columns were found to precede severe convection in tracked convective

cells with a range of lead times from 0 to 20 min depending on the case day. Requiring maxima above 1.4 dB and 30 dBZ of Z_{DR} and Z_{H} respectively was an appropriate second condition for all three cases although the skill in the early detection of severe convection varied across case days. Despite the high probability of detections, the high false alarm rate accompanied by low critical success index and data latency limit performance based on the three cases considered in this study. Nevertheless, the ability to detect Z_{DR} columns in operational radar data with a useful lead time prior to severe convection in certain conditions is a promising development towards advancing nowcasting of severe convection in the United Kingdom.

4.1 Introduction

A differential reflectivity (Z_{DR}) column is defined as "a region of enhanced Z_{DR} as situated above the 0 °C level" (Kumjian, 2013) that can be identified from weather radar measurements. Z_{DR}, which is defined as the difference in dB between the horizontally and vertically polarized radar reflectivity, Z_{H} and Z_{V}, is generally a measure of the sphericity of radar targets for which the Rayleigh approximation is valid. More positive values indicate more oblate shapes, although for large hydrometeors, Mie resonance scattering effects could disrupt the relationship between aspect ratio and Z_{DR}. The majority makeup of a Z_{DR} column is raindrops at its base and wet hail with supercooled raindrops or those in the process of freezing near the middle and upper sections of the column (Kumjian et al., 2014; Snyder et al., 2015). As such, a Z_{DR} column is indicative of a strong updraft that would support the lofting of these large oblate drops. In the storm simulation by Carlin et al. (2017), Z_{DR} columns were coincident with updrafts collocated with deep plumes of saturation and regions of latent heating directly above the columns. This suggests that latent heat release from condensation and freezing processes contribute to intense updraft strengths.

Although ice crystals such as dendrites and plates can also enhance Z_{DR}, these tend to have small Z_{H} values and can thus be discriminated from large raindrops (e.g. Hogan et al., 2002, 2003; Westbrook et al., 2010). When the concentration of large raindrops is low, a Z_{DR} column may have small Z_{H} value too, in which case further context such as temperature, storm evolution and vertical extent of the column will help distinguish the signature from ice crystals.

Z_{DR} columns have been widely documented in the literature, starting from early polarimetric radar observations (e.g. Illingworth et al., 1987). They have been related to areas near or at updraft maxima (e.g. Kumjian and Ryzhkov, 2008; Kumjian et al., 2014; Snyder et al., 2015) as shown conceptually in Figure 4.1a. Brandes et

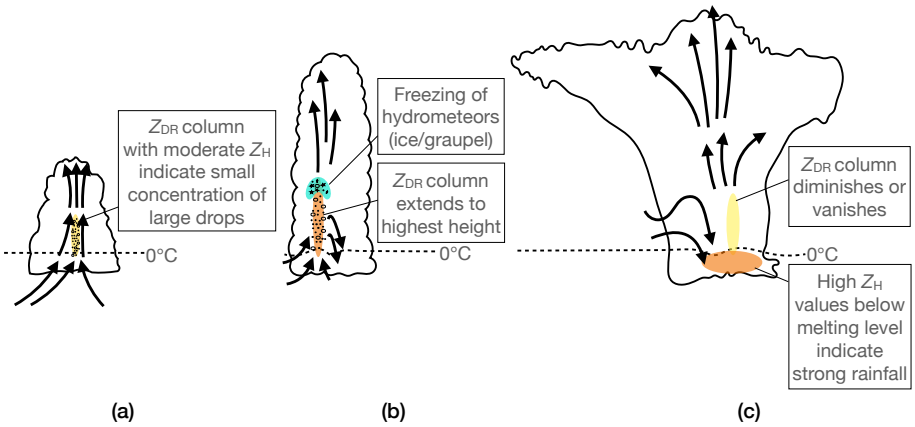

Figure 4.1: Conceptual diagrams showing the (a) developing (b) vigorous growth and (c) mature stages of a convective cell focusing on Z_{DR} column evolution.

al. (1995) showed using in situ aircraft measurements through a limited number of convective cells that the observed Z_{DR} columns were dominated by large liquid drops and mixed-phased precipitation near the top of Z_{DR} columns as labelled in Figure 4.1b. In Kumjian et al. (2014), the evolution of a simulated Z_{DR} column starting from small oscillations in height of the melting layer to reaching its maxium nearly 6 km AGL happened on the order of ten minutes. As illustrated in Figure 4.1c, Herzegh and Jameson (1992) have found both heavy rain and hail polarimetric signatures in a mature convective cell following the manifestation of a Z_{DR} column. Kumjian et al. (2014) found a lag of 10-15 minutes when correlating the evolution of Z_{DR} column height with increases in Z_{H} and hail mass content at the surface in their simulation and an observed supercell case. The largest lead times between peaks in observed Z_{DR} column size prior to severe hail reports and severe wind reports were 7 and 9 minutes respectively (Kuster et al., 2019). More recently, studies have highlighted the importance and usefulness of Z_{DR} columns in informing forecast warning decisions, compared with only utilizing reflectivity signatures (e.g. Kuster et al., 2020).

The UK Met Office has fully upgraded all 15 C-band radars as of January 2018 to have polarimetric capabilities. Three-dimensional radar composite products that incorporate the whole UK radar network, originally developed for the European SESAR Aviation programme, provide large horizontal spatial coverage on the order of 1000 km (Scovell and al-Sakka, 2016). Whereas a single radar would only be able to detect hydrometeors as high as its highest elevation, thus leaving the so-called "cone of silence" aloft closest to the radar, the dense UK network permits nearby radars to fill in these regions of missing observations. The 3D vertical structure provides important information for aviation meteorology where pilots navigate to avoid areas of severe convective development (Scovell and al-Sakka, 2016). It also complements existing surface rainfall rate products (Harrison et al., 2009) for

nowcasting severe convection over the entirety of the United Kingdom that could cause flooding, which could be used as a central component of a national severe convection nowcasting system. Stein et al. (2020) verified the reliability of the 3D composite by comparison with data from the Chilbolton Advanced Meteorological Radar (CAMRa) using cloud-top height, fractional coverage and storm morphology, all with reflectivity thresholds for studying convective storm characteristics.

The use of Z_{DR} for nowcasting is currently only explored in a few countries. The effectiveness of Z_{DR} columns detection for the United Kingdom is yet to be explored. Plummer et al. (2018) studied Z_{DR} signatures in warm-based convective cases (i.e., convective events for which the inflow source originates from levels warmer than freezing point) from the summer of 2013 Convective Precipitation Experiment (COPE) field campaign. Using data from a mobile X-band radar, they showed that larger derived precipitation rates were associated with convective systems containing Z_{DR} columns. However, cases studied in Plummer et al. (2018) had access to a research radar that scanned at 10 elevation angles, as opposed to the 5 angles used operationally. It is not self-evident that Z_{DR} columns can be used for nowcasting based on these findings alone. Furthermore, their results may partly be influenced by the unique topography of the south-west peninsula that inspired the COPE campaign.

To harness the greater spatial domain of the 3D radar composite constituting data from multiple overlapping radars, for this study, it was upgraded to include Z_{DR} to investigate the operational potential of using Z_{DR} columns for nowcasting severe convection. This study assesses the effectiveness of an implemented threshold-based Z_{DR} column detection algorithm for diagnosing severe convective development across three different case days within the United Kingdom.

Cases studied are introduced in the next section (Section 4.2), followed by a description of the data used and a description of the Z_{DR} column detection algorithm in Section 4.3 including an analysis of sensitivity to threshold values. Results pertaining to specific convective cells, lead time and verification of the algorithm's accuracy in nowcasting severe storms are detailed in Section 4.4. A discussion and conclusion are presented in the final section (Section 4.5).

4.2 Cases of Severe Convection

4.2.1 Radar-based definition of severe convection in the United Kingdom

In order to diagnose whether a tracked storm cell eventually develops into a "severe" storm, we need a quantitative definition of what constitutes a severe storm. In this

study, we have chosen to define this based upon counting the accumulated number of high-reflectivity MAXDBZ pixels within each tracked cell. The quantity MAXDBZ is the vertical maximum of radar reflectivity Z_{H}. In the radar composite, a single pixel covers an area of $1 \times 1\,\mathrm{km}$, and a time frame of 5 min. An accumulated number of 12 pixels could thus be a storm with a single pixel above the threshold persisting for 1 h, or a storm with 12 pixels above the threshold lasting only 5 min (and any scenario between these extremes). Having analysed all tracked storms across our three case studies, we find that 50 accumulated pixels of MAXDBZ values that are greater than or equal to 50 dBZ correspond well to the 99th percentile of accumulated MAXDBZ pixels across tracked cells. Thus, 50 accumulated 50 dBZ pixels in the MAXDBZ field are selected as a criterion for labelling a tracked storm as severe in this study. A physical interpretation of 50 accumulated pixels of 50 dBZ is 2.0×10^8 kg of rain or having a depth of 204 mm if it were concentrated in a $1\,\mathrm{km}^2$ surface, assuming the Marshall-Palmer relationship (Marshall and Palmer, 1948) for converting reflectivity to rainfall.

In contrast to the United States, where the definition of a severe thunderstorm is one that produces hail with diameters equal to or larger than an inch, wind gusts that exceed 58 mph and/or produce a tornado (National Weather Service, 2017), the United Kingdom does not have such a definition and hardly experiences inch-sized hail. In the United Kingdom, severe thunderstorms are marked by heavy precipitation, which are associated with sustained high-reflectivity pixels within an evolving convective cell. This justifies the choice of using accumulated MAXDBZ as a metric as opposed to very high reflectivity cores for large hail diagnosis or Doppler signals that would indicate strong gusts.

4.2.2 Cases

To develop and test the Z_{DR} column detection algorithm, three cases were selected from the European Severe Weather Database (Dotzek et al., 2009) with news reports of heavy rain or hail associated with severe convective events in the United Kingdom.

On 16 June 2020, multiple intense isolated cells resulted in cases of damaging lightning and heavy rain over the West Midlands. The sounding on that day is shown in Figure 4.2a and is characterized by moderate instability with convective available potential energy (CAPE) of around $1300\,\mathrm{J\,kg^{-1}}$. The sounding profile presents an unstable surface layer and a moist surface to mid-level, up to 600 hPa. A moderate bulk wind shear of $11\,\mathrm{m\,s^{-1}}$ from surface to 6 km accompanied with a positive vorticity filament aloft that would have promoted dynamical ascent via differential positive vorticity advection likely supported convective development (not shown). The bulk Richardson number was approximately 100, placing the storm

environment within the single or multi-cell storms regime (Weisman and Klemp, 1982).

On 10 August 2020, multiple cells formed in south-western England, which developed into a mesoscale convective system and advected northwards to parts of Wales. Cases of damaging lightning and heavy rain were recorded in parts of Wales including Swansea. The sounding shown in Figure 4.2c has CAPE reaching $850\,\mathrm{J\,kg^{-1}}$ when considering ascent of the most unstable parcel. Surface heating later during the day (not shown) would have contributed to more instability. Similar to 16 June 2020, a positive vorticity filament aloft in the afternoon hours would have supported convective development. The bulk wind shear of $4\,\mathrm{m\,s^{-1}}$ gives a bulk Richardson number of around 100, similar to that of the June case.

On the afternoon of 20 July 2021, isolated cells formed over East England and East Midlands, evolving into a multi-cell system towards the evening and finally dissipating before midnight. Multiple cases of flooding and hail were recorded for different locations in England between 14 and 17Z. The sounding for this case is presented in Figure 4.2e with CAPE exceeding $1600\,\mathrm{J\,kg^{-1}}$. There was also a highly positive area of vorticity aloft during the afternoon hours of this case. The bulk wind shear of $4\,\mathrm{m\,s^{-1}}$ gives a bulk Richardson number of around 200.

The three chosen case days present a variety of radar echo sizes and organisations as seen in Figure 4.2b,d,f. Locations of the described radiosonde launches are marked as red crosses in the same figures. Convective cells within these three case days introduced are tracked and investigated in this study.

4.3 Data and Methodology

4.3.1 UK 3D radar composite

The UK Met Office operational radar network is comprised of 16 C-band radars. Fifteen of these radars are located within the United Kingdom and one is on the Channel Islands. All C-band radars have been fully upgraded as of January 2018 to have dual-polarization capabilities. Each radar completes a set of plan-position indicator (PPI) scans at elevations 0.5, 1.0, 2.0, 3.0 and 4.0 degrees approximately every 5 min. The radars have a pulse repetition frequency of 300 Hz and a scan velocity of 8.4 degrees per second for the lowest two elevations and 15 degrees per second for the higher elevations. Depending on the rotation rate, a variable number of pulses are integrated and averaged once an integer degree boundary is crossed. Each PPI scan covers a range of 255 km, has range gates of 600 m and a radar beamwidth of 1.0°.

In this study, multi-radar composites were generated using various configurations

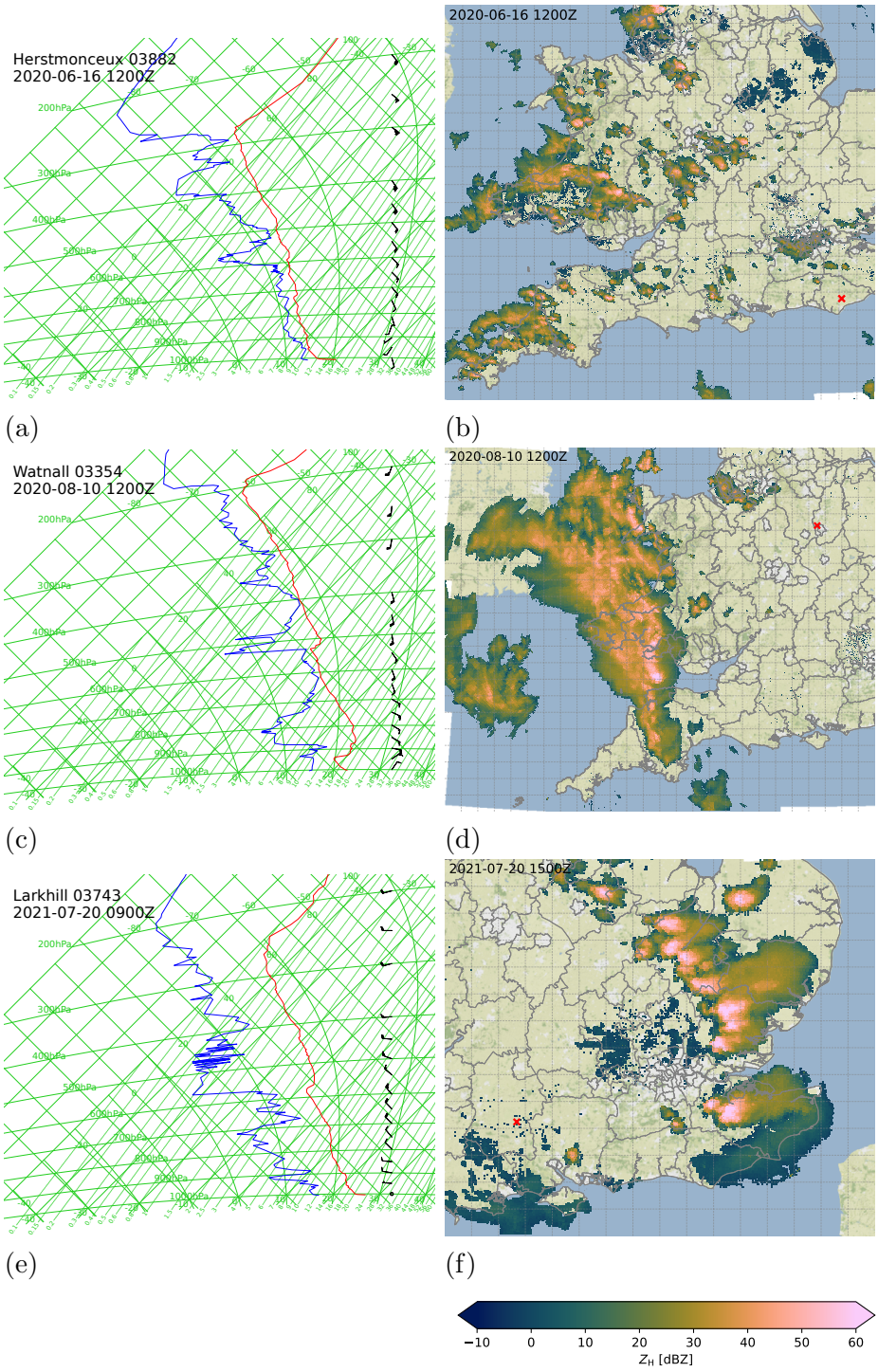

Figure 4.2: Tephigrams showing reported sounding data from (a) Herstmonceux on 16 June 2020 at 1200Z, (c) Watnall on 10 August 2020 at 1200Z and (e) Larkhill on 20 July 2021 at 0900Z. Blue and red lines correspond to dewpoint and dry bulb temperature. Wind barbs are plotted on the right side at selected pressure levels. Maximum reflectivity plots (b), (d) and (f) show a snapshot of radar echoes present on the same case days as the tephigrams in (a), (c) and (e) respectively. The red cross on each plot shows the location of the radiosonde launch. Map tiles by Stamen Design, under CC BY 4.0. Data by OpenStreetMap, under ODbL.

of the Hameldon Hill, Ingham, Clee Hill, Crug-y-Gorllwyn, Chenies, Thurnham, Cobbacombe Cross, Dean Hill and Predannack Met Office radars. The locations of these radars and others in the network are shown in Figure 4.3. These nine radars provide coverage of convective storms over southern England and Wales, coincident with the severe weather observations described in Section 4.2. The use of data from multiple radars helps to cover the "cone of silence" that is not sampled by the highest and lowest elevation scans from a single radar. Scovell and al-Sakka (2016) show that a 1 km^3 volume intersected by different 3 dB radar beams results in up to 17 available observations from multiple UK radar volumes.

Following Scovell and al-Sakka (2016), the radar data are interpolated onto a three-dimensional Cartesian grid, with 1 km horizontal and 500 m vertical spacing. Advection corrections are applied before compositing, using motion vectors derived from the previous two radar composites. In places where the radars overlap, a range-dependent weighting scheme of Zhang et al. (2005) is used. Finally, vertical linear interpolation is carried out at the request point. This study extends the described compositing process to the Z_{DR} field, by employing a similar method of interpolating Z_{H} in dB units.

4.3.2 Cell identification

Individual convective cells are identified from the MAXDBZ field by applying a dynamically thresholded image processing algorithm Otsu (1979). For each pixel and for a given time stamp, this method separates the surrounding pixels within a circular footprint of 5 km^2 into two classes, cell (foreground) and not-a-cell (background) and determines the dynamic threshold by minimising intra-class intensity variance. More details of the cell identification algorithm can be found in Supplementary Material 4.6.1. The diagrams in Figure 4.10 illustrate the operation of image thresholding, while Figure 4.11 demonstrates the operation of the cell identification algorithm. The resulting dynamic-thresholding has its advantages over using a fixed threshold value. Firstly, developing cells can be identified at lower reflectivity values. Additionally, individual convective cells can be identified when embedded within a region of high reflectivity. Z_{DR} columns tend to be quite localized and are usually collocated within or near individual narrow updrafts that can develop before or during the occurrence of high radar reflectivity (Kennedy et al., 2001). It is therefore useful to study Z_{DR} columns within tracked cells using a dynamic threshold. Finally, the identified convective cells were tracked using an object-based algorithm developed by Stein et al. (2015). In brief, horizontal motion vectors are derived from previous images to displace the convective cells and cells inherit the identification number and properties of prior cells that have sufficient overlap. With

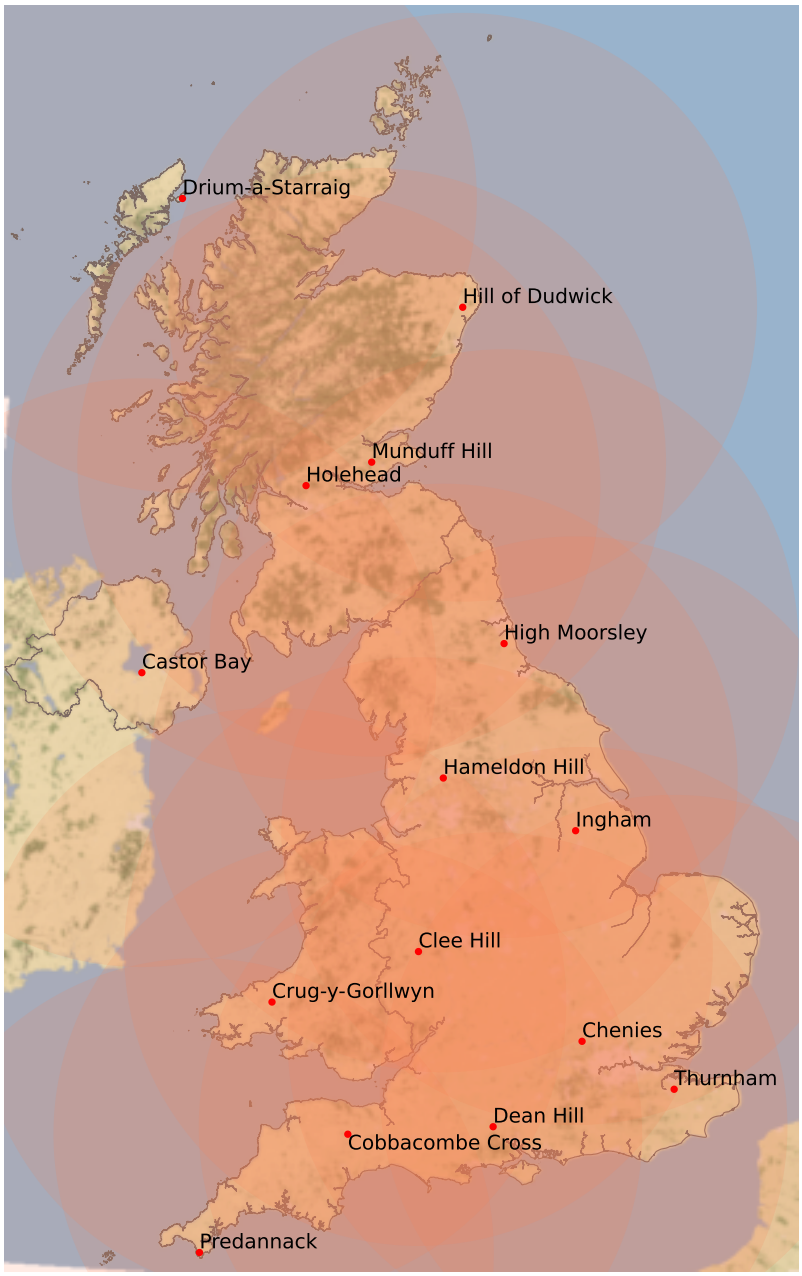

Figure 4.3: An overview of UK Met Office C-band radar locations and names. Range rings of 255km are included around each radar site. Map tiles by Stamen Design, under CC BY 4.0. Data by OpenStreetMap, under ODbL.

the ability to track objects, we can consider the temporal evolution of Z_{H} and Z_{DR} within each tracked convective cell.

4.3.3 Z_{DR} column detection algorithm

Since Z_{DR} columns are defined to intersect the freezing level, its height has to be found first before we identify such columns. The Met Office Unified Model (UM) has a global configuration that provides deterministic forecast covering a 6-day period. The model has a resolution of approximately 0.234×0.153 degrees of latitude and longitude respectively. Model runs occur every 12 h at 0 and 12UTC with forecast available every 3 h from T+0 to 60 h. The temperature field is available every 12 h on standard pressure levels (i.e. 1000, 950, 925, 850, 700, 500, 400, 300, 250, 200, 150 and 100 hPa). The pressure level parameters used in this study are geopotential height and temperature at all standard pressure levels.

For each generated radar composite, the freezing level is determined by first finding the closest model run in time occurring before the valid time of the radar composite. The closest available time step within that model run is then selected for calculation of the freezing level. With the given geopotential heights and corresponding temperatures for the 12 standard pressure levels, geopotential heights are linearly interpolated to derive geopotential heights where air temperature is 0 °C over the spatial domain of the radar composite. Mittermaier and Illingworth (2003) have confirmed that the MetUM predicts the 0 °C wet-bulb temperature height to within the specified 200 m error when compared with observations. While we speculate that the model will have improved since then, this error is smaller than the vertical resolution of the radar composite and thus suitable for this study.

With freezing heights calculated, we can now define the base of potential Z_{DR} columns within the 3D radar composite. The detection algorithm uses a primary Z_{H} threshold of 10 dBZ and primary Z_{DR} threshold of 1.0 dB to generate a 3D contiguous volume that extends at least 500 m above the freezing level to be considered a column candidate. These primary thresholds are the same as those used in Plummer et al. (2018), whereas the study by Snyder et al. (2015) uses a $Z_{\mathrm{DR}} \geq 1.0$ dB-only criterion with spatial filtering and despeckling to remove noisy signals such as ice along the edge of anvils. A candidate is then classified as a column if the maximum Z_{H} and maximum Z_{DR} within the volume exceed what we will refer to as secondary thresholds. These secondary thresholds of Z_{H} and Z_{DR} can be equal to or higher than the fixed primary thresholds to ensure well-defined column structures are identified, while eliminating noisier data. A visual comparison of Z_{DR} columns detected with or without the use of secondary thresholds can be found in Figure 4.12 of Supplementary Material 4.6.2. An analysis on the choice of secondary thresholds

will be explored in the following section.

4.3.4 Example of Z_{DR} column detection

The 12 panels in Figure 4.4b show radar composite generated MAXDBZ plots covering a 30×40 km region in south-east England, indicated in Figure 4.4a. These plots show the case of a developing storm cell on 20 July 2021 and are overlaid with Z_{DR} column detection field shown as black pixels. In these detections, secondary thresholds of Z_H and Z_{DR} in the algorithm were set to 25 dBZ and 2.5 dB, respectively, as per the thresholds used in Plummer et al. (2018). The storm cell contained multiple Z_{DR} column detections starting from 1310Z and eventually grew into a storm containing MAXDBZ exceeding 50 dBZ at 1335Z. Flooding associated with the storm was recorded in mid-Kent and was reported by multiple news outlets (e.g. McConnell, 2021). The flash floods were also documented as a flooding event in the European Severe Weather Database (Dotzek et al., 2009).

Figure 4.5 visualises the Z_{DR} column detections within the blue rectangle domain at 1310Z with meridional and zonal cross sections. Figure 4.5a shows a vertical maximum plot of Z_H with accompanying cross sections. Figure 4.5b is the same plot but for Z_{DR}. These plots clearly show a contiguous volume of enhanced Z_{DR} exceeding 3.0 dB extending up to around 6 km in height, corresponding to 3 km above the environmental freezing level on that day. The identified feature is also associated with reflectivity values of 30 dBZ consistent with the automatically detected Z_{DR} columns in Figure 4.4.

4.4 Results

4.4.1 Time series analysis

To test whether Z_{DR} columns are of use for early detection of severe weather, we first analyse the time series of tracked cells for the time between Z_{DR} column detection and onset of severe weather as defined using MAXDBZ described in Section 4.2.1.

Figure 4.6 shows a composite time series analysis of accumulated MAXDBZ pixels and accumulated Z_{DR} column pixels within tracked storms. We accumulate the number of Z_{DR} column pixels as well to test the importance of size and persistence of the Z_{DR} column for severe weather detection. Note that we only consider Z_{DR} column footprints, not the volume of 3D Z_{DR} observations. Only tracked storms that had both Z_{DR} column pixels and were eventually labelled as severe were included in this analysis; missed storms and false alarms will be considered in the next sub-section. Zero lead time is defined as the time when the definition of severe

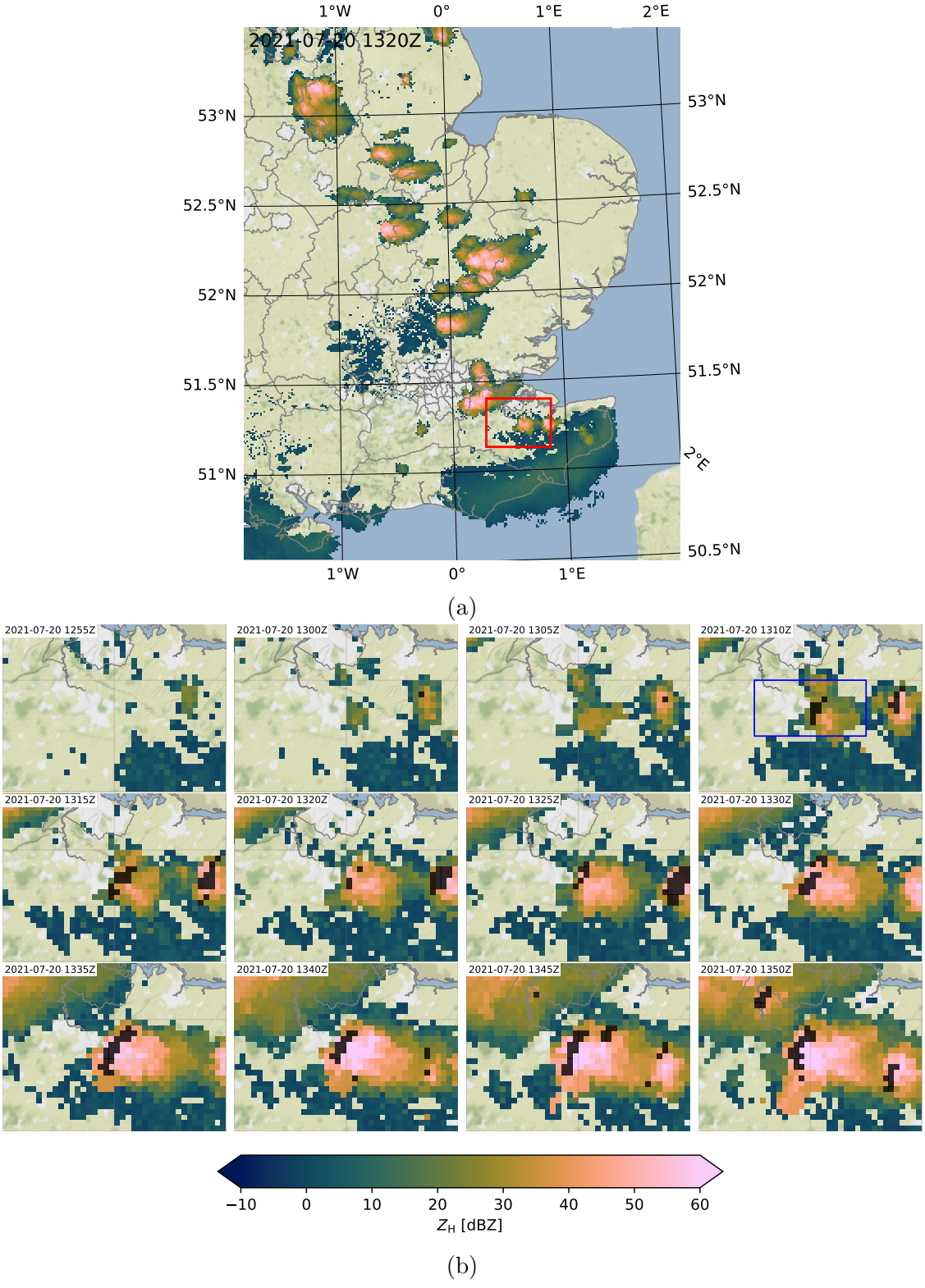

Figure 4.4: (a) An overview plot of MAXDBZ over eastern England on 20 July 2021 at 1320Z. The red rectangle demarcates a domain of interest with a convective storm development case. (b) A series of MAXDBZ showing convective storm development within the red rectangle domain for 20 July 2021 from 1255 to 1350Z. Panels in (b) are radar composites generated five minutes apart. Black pixels are detections of Z_{DR} columns. The blue rectangle in the 1310Z plot demarcates the region of the cross section of a convective cell in Figure 4.5. Map tiles by Stamen Design, under CC BY 4.0. Data by OpenStreetMap, under ODbL.

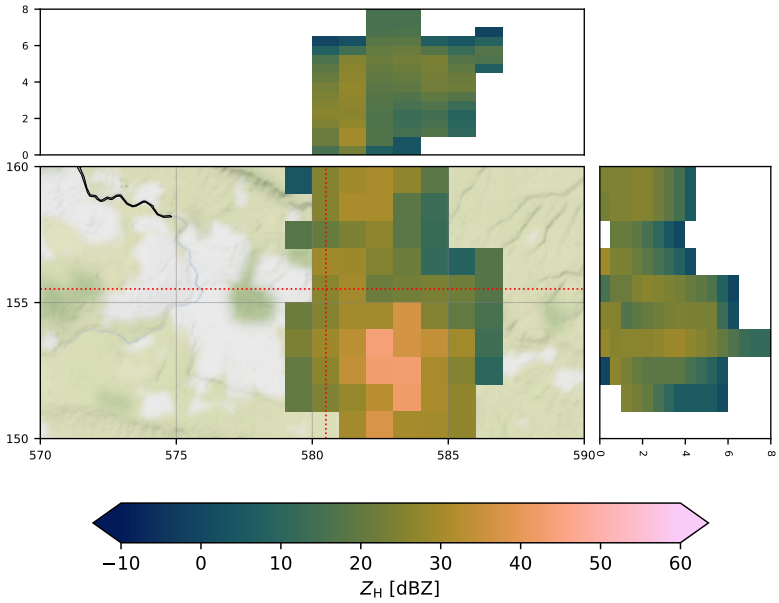

(a)

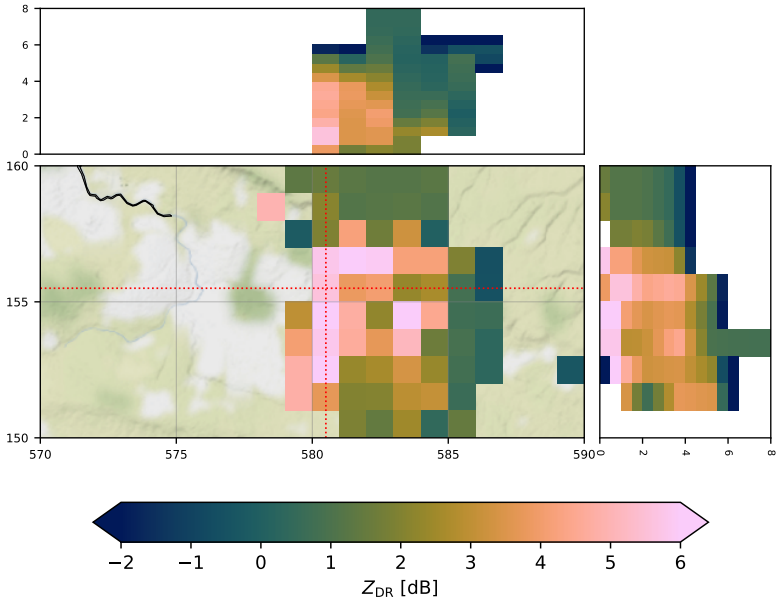

(b)

Figure 4.5: (a) A maximum Z_H plot with vertical cross sections on 20 July 2021 at 1310Z. Red dotted lines show the position of the vertical cross sections. Vertical cross section plots have 2 km tick labels in height. Spatial domain covered is the blue rectangle in Figure 4.4b, 1310Z panel. Enhanced Z_{DR} values exceeding 3.0dB are present near the western flank of the cell suggesting the presence of a Z_{DR} column. (b) As in (a), but for Z_{DR}. The Z_{DR} column is accompanied by reflectivity values not exceeding 30dBZ. Map tiles by Stamen Design, under CC BY 4.0. Data by OpenStreetMap, under ODbL.

was met by the tracked cell. The choice of accumulated Z_{DR} pixels is in contrast to several past studies that have used column properties such as their heights, volume, area and maximum Z_{DR} value within the column. Past observational studies such as Kuster et al. (2020) have focused on measuring column properties by utilizing a bespoke rapid-scan strategy and is therefore not characteristic of what could be done operationally with the UK radars used in this study. Snyder et al. (2015) used operational data from the NEXRAD WSR radars that scan at higher elevation angles, enabling them to report the heights of Z_{DR} columns defined as the height of $Z_{\mathrm{DR}} \geq 1.0\,\mathrm{dB}$ at each pixel. In contrast, we are interested more in the persistence of Z_{DR} columns rather than their vertical extents. We are also limited by the compositing process, which may use information from radar ranges exceeding 100 km and hence larger beam sampling volume with uncertainty in the vertical on the order of 1 km. While on a "storm object" basis, Z_{DR} column information could be reasonable; its height is not reliable on a pixel-by-pixel basis. Stein et al. (2020) also found quite a large root-mean-square error in heights of reflectivity contours within the radar composite but with only a small bias. This further suggests the suitability of using aggregate information over instantaneous measurements. Past modelling studies (e.g. Kumjian et al., 2014) were able to measure column properties accurately at higher spatial resolutions. However, in this study, we are limited to a horizontal resolution of 1 km. Rather than studying the properties of each Z_{DR} column signature, the reasons provided justify using an accumulated metric to ensure robustness of a possible Z_{DR} column or multiple of them occurring within a tracked convective cell.

For the cases of 16 June 2020 (Figure 4.6a,d) and 20 July 2021 (Figure 4.6c,f), the median and upper quartiles show a clear signal of 10-20 km^2 of Z_{DR} column pixel accumulation before time zero. Both cases see the steepest increases in Z_{DR} column pixel accumulation at approximately 10-20 min of lead time. For the case on 10 August 2020 (Figure 4.6b,e), the accumulation of Z_{DR} column pixels in the median time series at zero time is lower, at 8 km^2 compared with 14.5 and 18 km^2 for the other two cases, although the upper quartile time series is comparable across all three cases.

To consider the importance of size and duration of the Z_{DR} column, Figure 4.7 shows box plots of lead time, which is the duration between tracked storms meeting a certain threshold of accumulated Z_{DR} column pixels and meeting our radar-based definition of severe convection. Note that when we increase our threshold of accumulated Z_{DR} column pixels, we also reduce the sample going into these statistics, thus increasing the number of missed events. For all cases, lead time decreases with increasing Z_{DR} column number threshold. This is expected since tracked storms should accumulate an increasing number of detected Z_{DR} column pixels throughout

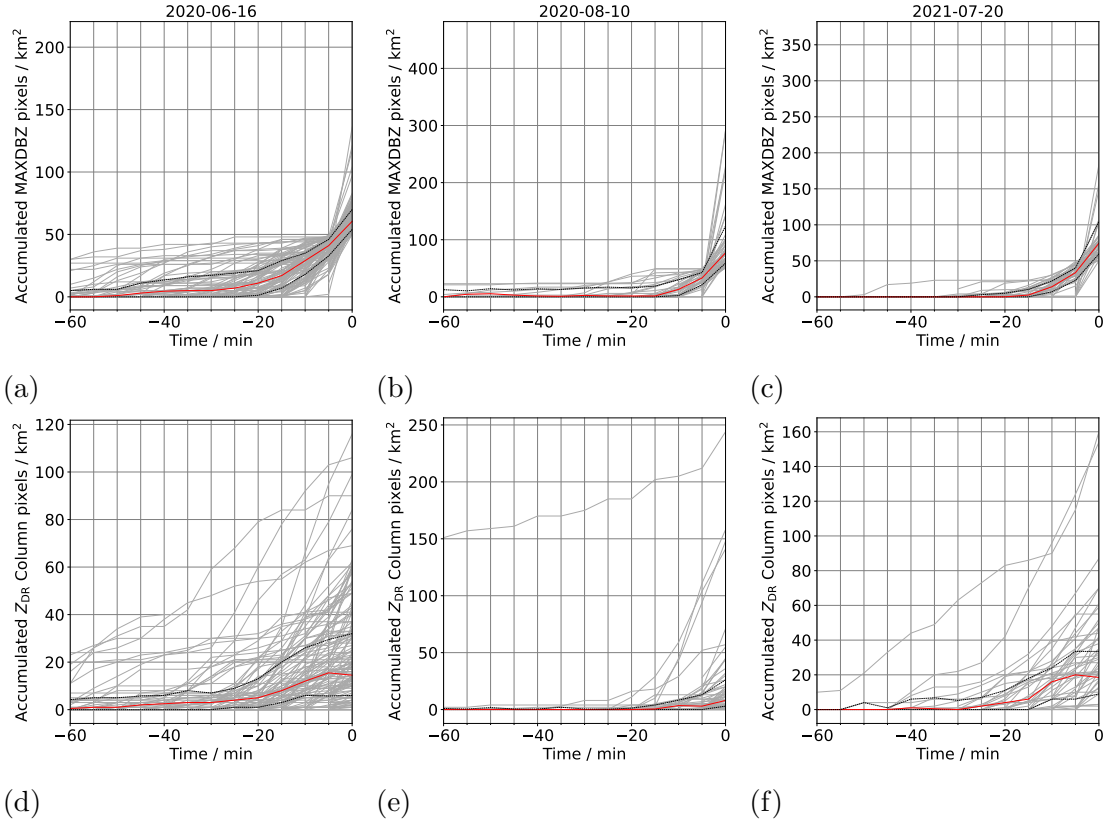

Figure 4.6: Grey lines showing time series of tracked storm properties in each case. Zero time is defined as the tracked storm meeting or having exceeded 50 accumulated pixels of MAXDBZ. In each sub-figure, upper panels (a-c) show MAXDBZ pixels within a tracked storm, whereas lower panels (d-f) show the accumulated number of detected Z_{DR} column pixels within each tracked storm. Red and black dotted lines show the median and quartiles of the time series, calculated from available data at each 5 min time step. First (a & d), second (b & e) and third (c & f) column of panels correspond to storms tracked on 16 June 2020, 10 August 2020, 20 July 2021.

their lifetimes, such that a larger accumulation of such pixels is likely to occur closer in time to the occurrence of high-reflectivity pixels. The spread of lead times also decreases when using a higher Z_{DR} column pixel threshold. Long lead times could also suggest the possibility for a long-lived storm that had Z_{DR} columns early in its lifetime but only later redeveloped into an intense storm that met our definition of severe convection. Thus, using a higher threshold of Z_{DR} column detection (e.g. 10 pixels) would suggest better robustness of Z_{DR} column detection, despite a shorter lead time. Z_{DR} columns are typically associated with vigorous updrafts that evolve into areas of high-reflectivity cores associated with greater concentrations of hail and large freezing raindrops. This conceptual model is supported by observations and modelling studies (e.g. Knight, 2006; Kumjian et al., 2014) that suggest Z_{DR} columns to precede the occurrence of high reflectivity up to 30 min in advance, although other studies such as Picca et al. (2010) may have found longer lead times of 40 min between Z_{DR} column detection and large hail diagnosis in some convective cells. It is worth noting, however, that our study covers a broader definition of severe convective weather not limited to hail.

For the same accumulated Z_{DR} column pixel threshold, we also observe variations in lead time between the three cases considered. Considering a Z_{DR} column pixel threshold of 10, the upper quartile lead times are 20, 5 and 15 min for 16 June 2020, 10 August 2020 and 20 July 2021 cases, respectively. This shows differences in the time of Z_{DR} column appearance within storm evolution between case days with varying synoptic situation, complicating any algorithm design using Z_{DR} columns for nowcasting.

4.4.2 Nowcasting verification

To investigate the skill of Z_{DR} column detection as a precursor of severe convection, non-precursor and non-severe events must also be considered. In addition to counting tracked storms with Z_{DR} column detection, a 2×2 contingency table is constructed to tally the number of tracked storms with Z_{DR} columns detected that did not later develop into a severe storm (false alarms), tracked storms without a Z_{DR} column precursor but later considered to be a severe cell (misses) and cells without a Z_{DR} column precursor and any remaining storms (correct negatives). From the number of hits (A), false alarms (B), misses (C) and correct negatives (D), verification metrics are calculated such as probability of detection ($\mathrm{POD} = A/(A+C)$), false alarm ratio ($\mathrm{FAR} = B/(A+B)$) and critical success index ($\mathrm{CSI} = A/(A+B+C)$). CSI lacks any dependence on the number of correct negatives, which makes it suitable as a performance measure for rare events. As mentioned in Section 4.3.2, a cell is a contiguous area of MAXDBZ pixels above

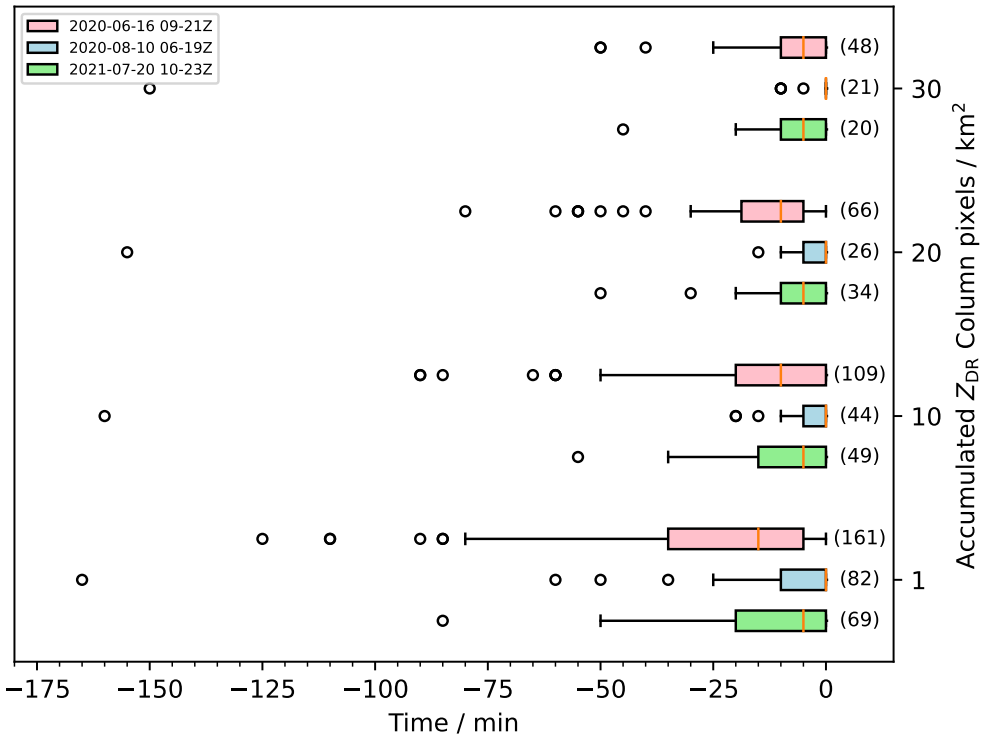

Figure 4.7: Box plots showing tracked storms that have met an accumulated Z_{DR} column pixel threshold and later lead to severe storm development. Lead time is the time between accumulated Z_{DR} column pixel threshold being met and the time when the tracked storm meets the severe requirement. Whiskers extend from the quartiles by 1.5 times the inter-quartile range. Tracked storms with longer lead times are marked as circles beyond the whiskers. Boxplots are grouped according to accumulated Z_{DR} column pixel threshold and sub-divided by different cases. Red, blue and green shading correspond to storms tracked on 16 June 2020 from 09 to 21Z, 10 August 2020 from 06 to 19Z and 20 July 2021 from 10 to 23Z respectively. The number of elements for each boxplot is shown in parentheses.

the variable "Otsu" threshold or 20 dBZ, whichever is higher, and a severe event as having accumulated 50 pixels over 50 dBZ, as described in Section 4.2.1. To confirm that these severe convective events are rare, we find base rates of 0.9%, 0.4% and 1.6% meeting the severe definition out of all tracked storms for the 16 June 2020, 10 August 2020 and 20 July 2021 case days, respectively.

To inform future development of nowcasting algorithms using Z_{DR} columns, we are also interested in the sensitivity of the detection algorithm to the various thresholds introduced, particularly (a) the secondary Z_{H} threshold, (b) the secondary Z_{DR} threshold and (c) the Z_{DR} column accumulation threshold. All three of these thresholds will affect the contingency table, with higher thresholds moving hits to misses and false alarms to correct negatives. Informed by Section 4.4.1 and Figure 4.7, our severe weather precursor requires 10 accumulated Z_{DR} column pixels between 5 and 30 min prior to the definition of severe weather being met within a tracked convective cell. The choice of this 30 min threshold was informed by the box plot of precursor lead times in Figure 4.7 showing most storms having precursor lead times of < 30 min. We note that this 30 min threshold considers lead times between 5 and 30 min, rather than storms meeting the severe definition beyond 30 min of having accumulated 10 Z_{DR} column pixels. Higher values of Z_{H} and Z_{DR} are considered more stringent secondary thresholds, since drops with even more oblateness are required in the storm for detection of a Z_{DR} column. This will lead to fewer storms labelled with precursors and more missed severe weather events, but also a decreased amount of false alarms.

Figure 4.8 shows the performance of the detection algorithm in nowcasting severe convective events by varying the secondary thresholds of Z_{H} and Z_{DR} for the cases of 16 June 2020, 10 August 2020 and 20 July 2021 respectively. For determining the significance of verification metrics presented, bootstrapping was carried out using secondary thresholds of 25 dBZ and 2.5 dB for the detection of Z_{DR} columns. This gives an estimate of the uncertainties for the corresponding verification metric across secondary threshold space of Z_{H} and Z_{DR}. In all three cases, POD decreases with increasing secondary thresholds. Going from thresholds of $Z_{\mathrm{DR}} \geq 1$ dB and $Z_{\mathrm{H}} \geq 18$ dBZ to $Z_{\mathrm{DR}} \geq 2$ dB and $Z_{\mathrm{H}} \geq 30$ dBZ reduces POD from around 0.47 to 0.38 in the June case. Likewise, we see a reduction in POD from 0.19 to 0.10 in the August case. In contrast, the July case shows fairly constant POD values of around 0.40. However, the reduction in FAR is greatest in the August case, from 0.77 to 0.65, followed by the July case from 0.43 to 0.36, whereas these are fairly constant with values around 0.50 for the June case.

A common metric used to assess the ability to forecast rare severe weather events is the CSI, also known as threat score. For each studied case day, choosing secondary thresholds of $Z_{\mathrm{DR}} = 1.4$ dB and $Z_{\mathrm{H}} = 30$ dBZ would provide the highest CSI values,

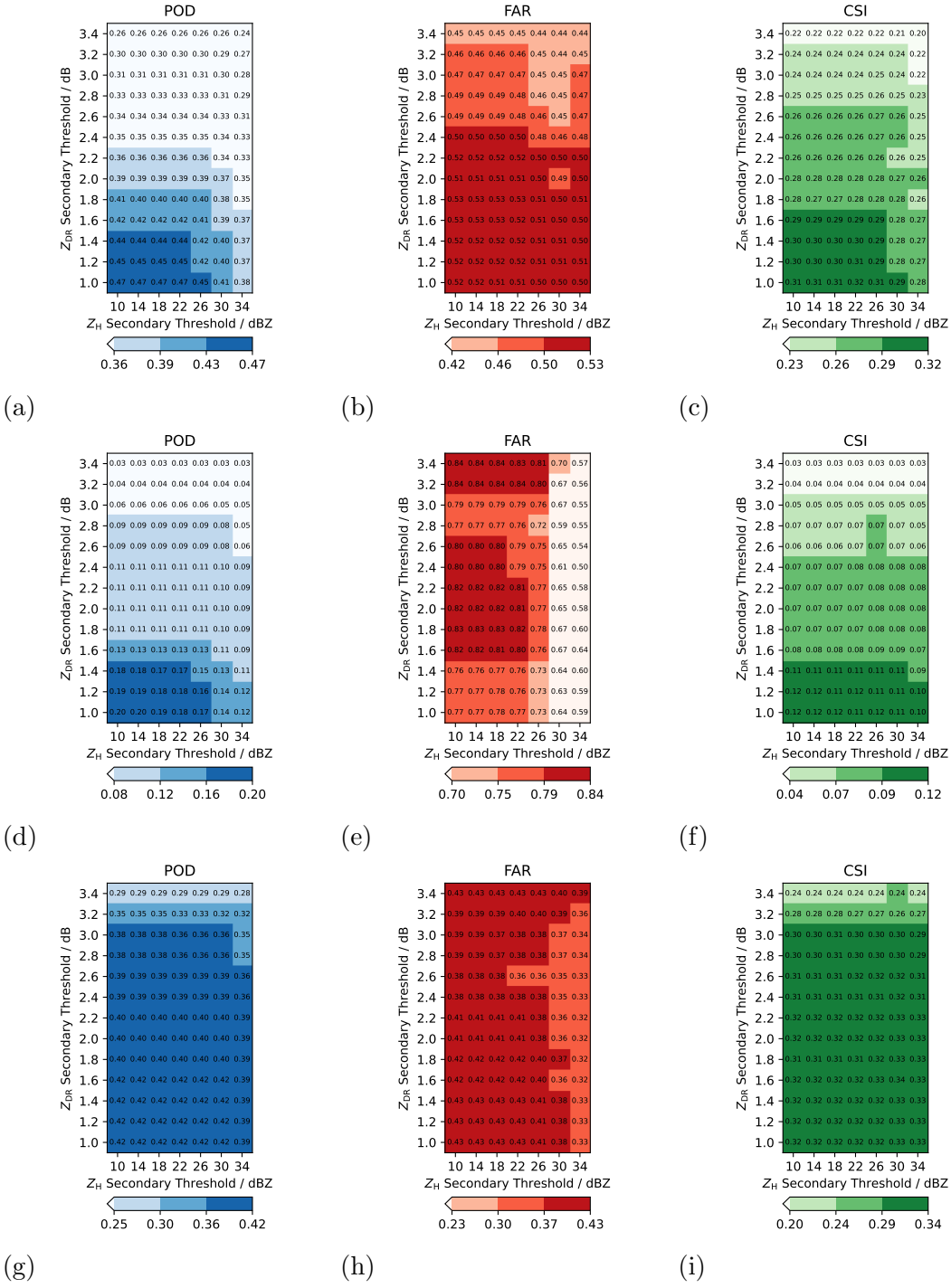

Figure 4.8: Verification metrics for verifying the effectiveness of Z_{DR} column appearance prior to severe convection for tracked storms on (a-c) 16 June 2020, (d-f) 10 August 2020 and (g-i) 20 July 2021 showing how probability of detection (POD), false alarm rate (FAR) and critical success index (CSI) varies over changing secondary reflectivity and differential reflectivity thresholds in Z_{DR} column detection algorithm. N =18605, 24723 and 4476 convective cells were tracked for 16 June 2020, 10 August 2020 and 20 July 2021 respectively. From bootstrapping tracked storms at 25dBZ of Z_H and 2.5dB of Z_{DR}, each colour level represents one standard deviation of change in the verification metric.

resulting in 0.28, 0.11 and 0.33. These values are lower than other nowcasting studies such as Seroka et al. (2012) that achieved CSI of up to 0.45 in cell-based verification when reflectivity was used to predict cloud-to-ground lightning.

We see differences in the distribution of CSI values across the secondary threshold space. The case of 10 June 2021 had the highest CSI around 1.0-1.6 dB of Z_{DR} and 10-26 dBZ of Z_{H} secondary thresholds. These values of Z_{DR} and Z_{H} are consistent with previous physical understanding that Z_{DR} columns consist of a low concentration of large drops present in growth stage of storms with updrafts later leading to severe convection.

The case of 10 August 2020 presents a different profile of maximum CSI extending to higher Z_{H} thresholds exceeding 30 dBZ although with a slightly narrower range of Z_{DR} thresholds between 1.0 and 1.4 dB. This is associated with the highest hit cases concentrated in the lower secondary Z_{H} Z_{DR} thresholds and significant decrease in false alarm cases as evidenced by the drop in FAR from 0.77 to 0.59 across tested Z_{H} thresholds. Similar to the June case, enhanced Z_{DR} thresholds are consistent with expected Z_{DR} column microphysics. The sensitivity of FAR across Z_{H} but less so in Z_{DR} suggests that the detection of Z_{DR} columns consisting of a higher concentration of raindrops resulted in a lower amount of tracked cells falsely predicted to meet the definition of severe convection.

The case of 20 July 2021 presents maximum CSI values that do not vary much over both Z_{DR} and Z_{H}. This is similar to the rather constant POD and FAR values over tested secondary thresholds. Similar to the August case, enhanced Z_{DR} thresholds are consistent with expected Z_{DR} column microphysics. However, the insensitivity of the POD metric to Z_{H} could suggest hail development in most tracked severe cells. The possible presence of hail within detected Z_{DR} columns in cells tracked on this day will be detailed later. In the August case, high CSIs were dominated by the hit cases mostly described by low thresholds and a marked decrease of false alarms with increasing Z_{H}. In this case, the number of hits (~ 30) and misses (~ 42) for Z_{DR} thresholds < 2.0 dB were fairly constant. Despite there being a decrease in false alarms for increasing Z_{H}, there was no significant increase in CSI.

To explore the possibility of hail growth in Z_{DR} columns, we use a hail diagnostic based on the polarimetric algorithm of Aydin et al. (1986). The diagnostic H_{DR} is a function of Z_{H} and Z_{DR} (See equations 4 and 5 in Aydin et al. (1986) for more details). The simple parametrisation of the inferred rainfall-hail boundary of $H_{\mathrm{DR}} = 0$ was predicted from disdrometer measurements. On a plot of Z_{H} against Z_{DR}, a radar measurement of tumbling hail will likely give a high Z_{H} value but low Z_{DR} and thus lie in the region above the $H_{\mathrm{DR}} = 0$ boundary. In other words, any positive H_{DR} could signify the presence of hail, with larger values providing more certainty that the signal is not due to raindrops. Depue et al. (2007) found an H_{DR}

threshold of 30 dB to be most reliable when tested against hail damage reports. We thus chose this threshold of $H_{\mathrm{DR}} \geq 30\,\mathrm{dB}$ to identify the potential presence of hail flagging columns in the radar composite where the maximum H_{DR} reaches above this threshold. Figure 4.9b,d,f shows where hail was identified using this approach for 16 June 2020, 10 August 2020 and 20 July 2021 cases, respectively. A small frequency of hail was diagnosed for the June case with 9185 pixels of Z_{DR} columns and 196 pixels of hail. Hail was diagnosed in isolated regions in the August case with 11,104 pixels of Z_{DR} columns and 240 pixels of hail. Z_{DR} columns diagnosed in this case over the Celtic Sea and Ireland may not be reliable owing to coverage by only one or two radars. In the July case, hail diagnosis was more widespread with 3506 pixels of Z_{DR} columns and 1049 pixels of hail. In this final case, the hail diagnostics were collocated with many regions of Z_{DR} column detection.

Reviewing Figure 4.8 with the knowledge that the July case has hail present, we can consider how that could affect the CSI pattern. In particular, a storm with hail present is highly likely to be severe (50 accumulated MAXDBZ pixels above 50dBZ) and has a high Z_{H}. For the July case, we see that the whole range of tested Z_{H} thresholds lead to little changes in POD, FAR and CSI, especially for Z_{DR} secondary thresholds of less than 2.0 dB. Analysis of further cases will be necessary to disentangle the Z_{DR} column detection from hail contamination and explore the need for an algorithm that can warn of both heavy rainfall and hail. It is also possible that different environmental conditions may have led to air parcels containing different drop size distributions with higher concentrations of smaller drops resulting in enhanced Z_{H}.

4.5 Discussion and Conclusions

A three-dimensional radar composite comprising data from polarimetric C-band radars was used for identifying Z_{DR} columns over the United Kingdom. The identification algorithm was tested for its ability in nowcasting severe convection, which was for this UK study defined as accumulating 50 km^2 pixels with MAXDBZ $> 50\,\mathrm{dBZ}$ over the lifetime of the cell.

Using image thresholding and object tracking techniques, storm timelines were derived. A lead-time analysis on these timelines found up to 20 min of lead time between an increase in the number of detected Z_{DR} column pixels and the tracked cell meeting the criterion for severe convection. However, it is worth noting the variability in lead time depending on the considered case and the accumulated Z_{DR} pixels used as a criterion for diagnosis of severe convection. Although we do not consider column height in this article, our findings on lead time are comparable

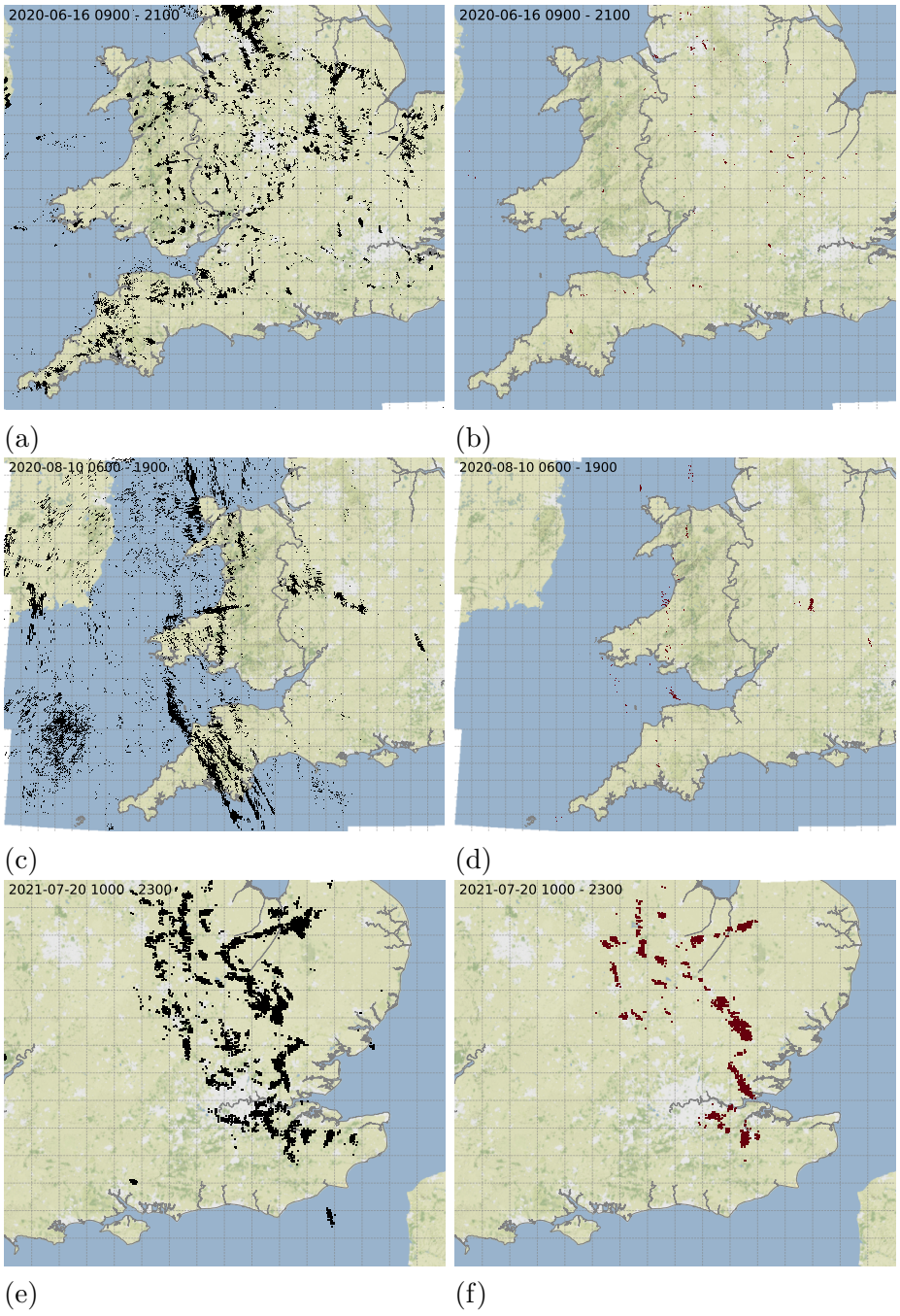

Figure 4.9: The left panels show accumulated detections of Z_{DR} columns using secondary thresholds of 2.5dB and 25dBZ Z_{DR} and Z_{H} respectively over the case days of (a) 16 June 2020, (c) 10 August 2020 and (e) 20 July 2021. The right three panels (b), (d) and (f) are accumulations of the hail diagnostic from Aydin et al. (1986) applied to the same three cases respectively. Brown areas indicate hail signals exceeding a vertical maximum of H_{DR} equal or exceeding 30dB. Map tiles by Stamen Design, under CC BY 4.0. Data by OpenStreetMap, under ODbL.

with storm cases in Kuster et al. (2020), where they found Z_{DR} column heights increasing 11 min prior to an increase in reflectivity within the cell, and in one case, Z_{DR} column development occurred 16 min prior to a hail report. Despite having different definitions of labelling storms as "severe" across studies due to differing storm morphologies and the occurrence of severe weather in different geographical regions, it is nevertheless promising to see how Z_{DR} columns act as precursors for severe convection.

Results from this study suggest that enhanced Z_{DR} values above 1.0 dB are suitable for Z_{DR} column detection within storms that lead to severe convection in the United Kingdom. Although this is similar to the implementation in Snyder et al. (2015), we also implemented an additional primary threshold of $Z_{\mathrm{H}} \geq 10$ dBZ to exclude noisy data and ice in stratiform cloud that could be mistaken for a Z_{DR} column. The need for secondary thresholds, as justified in Plummer et al. (2018), ensures the identification of subjectively well-defined column structures.

The use of verification metrics, such as CSI, in exploring secondary threshold space highlighted appropriate Z_{DR} and Z_{H} values for each case day. We were able to attribute the best algorithm performance for a wider spread of Z_{H} secondary thresholds to hail presence within detected Z_{DR} columns. In contrast to Plummer et al. (2018) who used secondary thresholds of 2.5 dB and 25 dBZ Z_{DR} and Z_{H} thresholds respectively for detecting Z_{DR} columns, our results suggest that preferred Z_{DR} secondary threshold be lower at 1.4 dB and a similar Z_{H} secondary threshold at 30 dBZ. We note, however, that the set of secondary thresholds that offer the best algorithm performance varies amongst cases.

Our study highlights several issues with using Z_{DR} columns to nowcast severe convection. Our POD of around 0.40 could be comparable with other studies, but similarly high FARs could consequently lead to lower CSIs. Potentially, additional criteria on the Z_{DR} column height could reduce the FAR and these are in line with the physical interpretation of Z_{DR} columns. However, for the UK composite, heights above 3 km are generally observed by low-elevation scans at ranges > 100 km. At such ranges, the beam widths are > 1 km leading to uncertainty in estimating Z_{DR} column height. A comparison of Z_{DR} columns in the composite against a research grade radar such as CAMRa might help (e.g. Stein et al., 2020), but the rarity of these events makes this a challenging task. Scan strategies involving higher elevations would also provide better coverage at higher altitudes. This would permit a more reliable measurement of Z_{DR} column heights, which could potentially be exploited as an additional identification criterion. Considering that data latency of producing a radar composite output is of similar magnitude to the median lead times of Z_{DR} column accumulation, we also acknowledge there to be some practical applicability of Z_{DR} columns as a precursor in the Met Office's operational setting

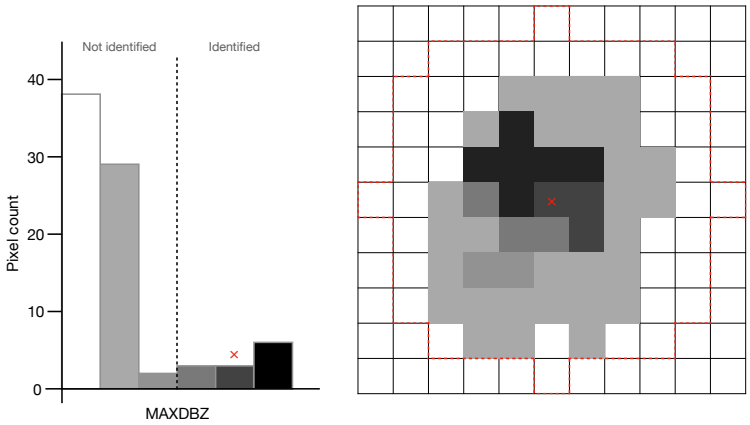

Figure 4.10: The histogram on the left shows the pixel counts of different MAXDBZ intensities and a partition to determine whether the pixel in question should be identified as part of a convective cell. The grid on the right is a fictitious MAXDBZ field.

at least based on the three cases presented here.

The question of whether a consistent set of thresholds can be found and whether Z_{DR} columns are more prominent at a similar range of lead times before the onset of severe weather in certain synoptic conditions could be of interest in future studies. The availability of the polarimetric data for the United Kingdom to capture more case days of interest will allow future work to build on existing synoptic regime analysis (e.g. Wilkinson and Neal, 2021) and Z_{DR} column prevalence within convective storms.

4.6 Supplementary Information

4.6.1 Explaining the Otsu image thresholding algorithm

The simplest form of the Otsu algorithm considers all pixels in a domain and returns a single intensity threshold that partitions pixels in the background and the foreground by minimising intra-class intensity variance. This form of the Otsu algorithm is useful for thresholding a single image.

Our variant of the Otsu algorithm applies thresholding to pixels within a footprint rather than the whole image. For instance, Figure 4.10 illustrates how the identification algorithm determines if the grid marked by the red cross should be identified as part of a convective cell. We first apply a circular footprint of five kilometre radius (dotted red border) around the grid point in question (red cross). Pixel

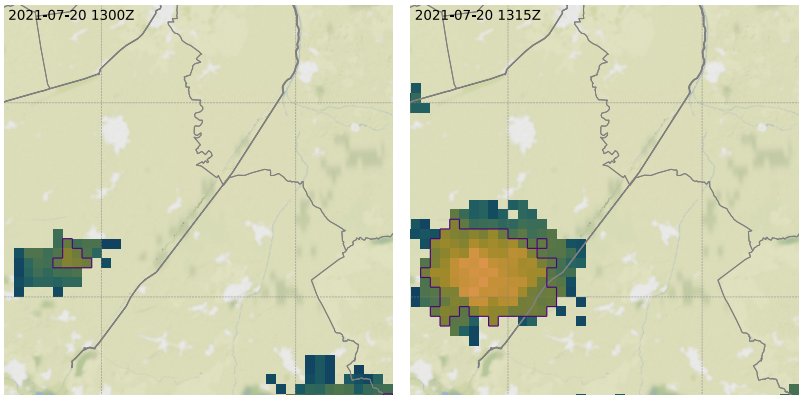

Figure 4.11: An example of an identified cell using the implemented Otsu algorithm on 20 July 2021 at 1300 and 1315Z. The dark purple outline highlights the identified cell.

(MAXDBZ) intensities within the footprint are tabulated and partitioned using the Otsu algorithm. In this example, the pixel intensity is higher than the calculated threshold and thus could be identified to be part of a cell, subject to it being higher than the fixed base threshold of MAXDBZ $\geq 20\,\mathrm{dBZ}$ and being part of a convective cell with an area exceeding $4\,\mathrm{km}^2$.

The process is repeated for other pixels in the image.

Figure 4.11 shows the result of the Otsu algorithm implementation. If one were to use a fixed threshold algorithm (e.g. 30 dBZ) instead of the Otsu thresholding algorithm, the convective cell would not have been identified as early as 1300Z.

4.6.2 The effect of using a secondary threshold in Z_{DR} column detection

Figure 4.12 highlights results at different steps of the Z_{DR} column identification. The left panel of the figure shows column detections that only use primary thresholds of $Z_{\mathrm{H}} \geq 10\,\mathrm{dBZ}$ and $Z_{\mathrm{DR}} \geq 1.0\,\mathrm{dB}$ fulfilled by all pixels within the identified column. The right panel also implements the same primary thresholds and, additionally, secondary thresholds of $Z_{\mathrm{H}} \geq 25\,\mathrm{dBZ}$ and $Z_{\mathrm{DR}} \geq 2.5\,\mathrm{dB}$, which are values that column maxima must meet to be identified as a Z_{DR} column.

The implementation of secondary thresholds eliminates Z_{DR} column signals that are likely to be false detections. For instance, the secondary thresholds have eliminated detections within stratiform-like rain near the eastern flank of the storm as circled in red. These are unlikely to be Z_{DR} columns associated with a developing

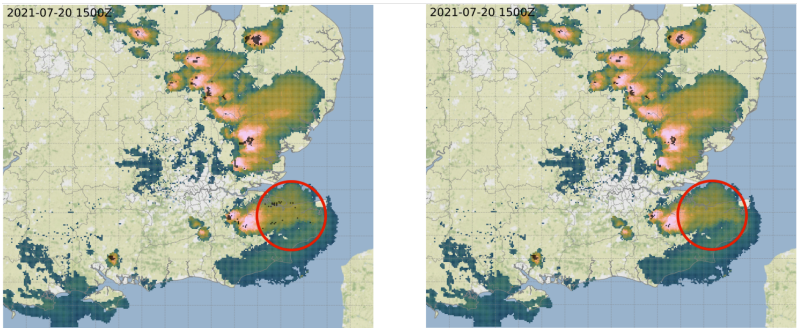

Figure 4.12: Both panels show the maximum reflectivity (MAXDBZ) field on 20 July 2021 at 1500Z, with Z_{DR} column detections shown as black pixels. The panel on the left applies the Z_{DR} column detection algorithm with only primary thresholds, whereas the panel on the right includes secondary thresholds.

convective cell. Conversely, using more stringent identification criteria decreases the number of Z_{DR} column detection pixels, which could omit weaker Z_{DR} columns that are still of interest. However, most cells in the example presented still contain Z_{DR} column detections, albeit a smaller area of them.

Chapter 5

Forward Operator for Z_{DR}

5.1 Introduction

This section reviews radar reflectivity and its relationship to scattering properties and the implementation of the existing radar forward operator in the MetUM. Section 5.2 describes how Z_{DR} is simulated for this thesis instead and presents results from sensitivity testing of this forward operator. The penultimate section, Section 5.3, details the implementation of the forward operator within the MetUM before the final section that summarises this work chapter.

A radar's reflectivity η is related to the radar cross section of scatterers σ_b and to the particle size distribution N.

$$\eta = \int_0^\infty N\left(\sigma_b\right) \sigma_b \, d\sigma_b \tag{5.1}$$

For spherical scatterers sensed by radars of long wavelengths, the Rayleigh scattering assumption could be made. Radar reflectivity is expressed as a radar reflectivity factor at either a horizontal Z_{H} or vertical polarisation Z_{V}.

$$Z_{\mathrm{H}} = Z_{\mathrm{V}} = \int_0^\infty N(D) D^6 \, dD \tag{5.2}$$

The derivation of Z for spherical hydrometeors is detailed in Section 1.2.1.

The Rayleigh scattering regime is only valid for electromagnetic waves scattered by particles with sizes much smaller than the sensing wavelength and the theory considers these particles to be spherical. Starting with the far-field approximation, where field behaviour is considered far away from the source of the electromagnetic waves, the unknown to be found is the total electric field in the interior of the dielectric particle. In Rayleigh scattering, this unknown is assumed to be an electrostatic solution within the particle, which is a uniform field for a spherical particle of a constant dielectric. Although the simplest to implement, a radar sensing with a

shorter wavelength comparable with hydrometeor size will cause the size parameter X to increase such that Rayleigh scattering theory becomes inappropriate. Figure 5.1 shows various scattering regimes separated by size parameters $X = \frac{2\pi r}{\lambda}$ for different particle radii r and sensing wavelengths λ. A C-band radar operating at 5.3 cm sensing raindrops of around 3.0 mm gives a size parameter of 0.4. This is in the transition region from Rayleigh scattering regime to Mie scattering regime. For a C-band radar with a wavelength of 5.3 cm, multi-millimetre hydrometeors will break the Rayleigh scattering assumption. However, Z_{DR} columns contain such supercooled drops reaching diameters of a few millimetres (Illingworth et al., 1987).

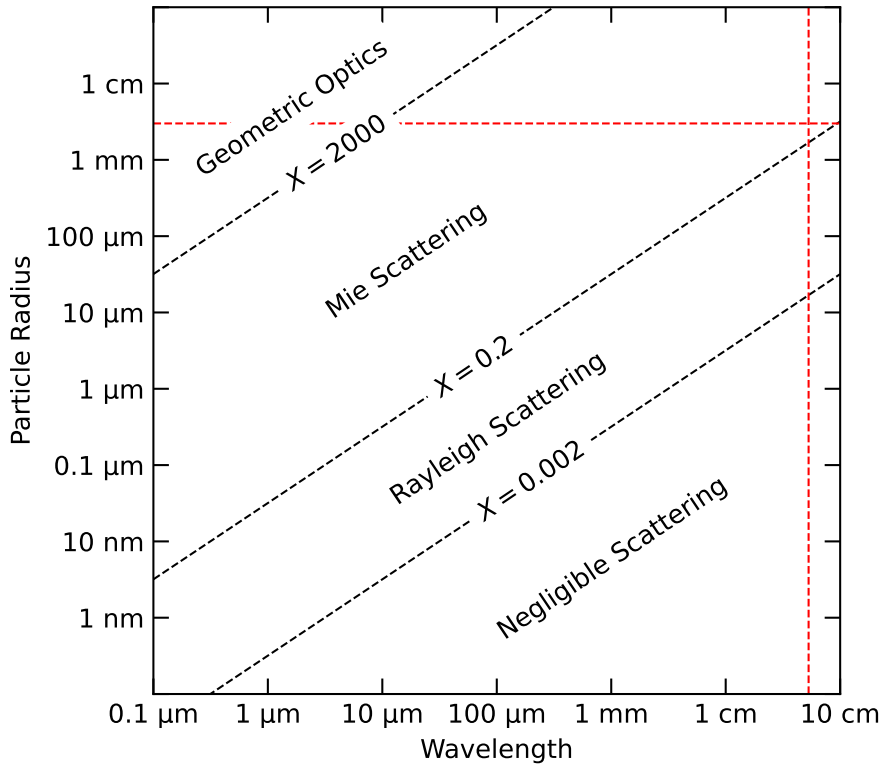

Figure 5.1: Sensing wavelength and particle sizes are shown at the bottom and left axes respectively. Dotted lines are contours of the same size parameter X, which is a function of radiation wavelength and particle radius. Redlines indicate a wavelegnth of 5.3 cm and a particle radius of 3.0 mm. Figure adapted from Petty (2006).

The assumption of spherical hydrometeors implies that radar reflectivity factors in both polarisations are equal, $Z_{\mathrm{H}} = Z_{\mathrm{V}}$. For a hydrometeor that is not spherical, such an assumption fails. The axes of polarisation of transmitted waves from a radar are modified by the hydrometeor's shape, size and refractive index. The differential effects of a partial reflection of the transmitted wave in the two planes of polarisation could yield different values of Z_{H} and Z_{V} and thus a non-zero Z_{DR}. Large raindrops are not spherical as observed in wind tunnel investigations by Pruppacher and Beard (1970).

5.1.1 Pre-exisiting radar forward operator

The large-scale precipitation scheme within the MetUM calculates radar reflectivity as a diagnostic. Radar reflectivity is used as an alternative or in addition to precipitation rate to determining precipitation strength. Radar reflectivity diagnostics are also of interest to those examining radar data directly, data assimilation and model evaluation using radar observations.

The MetUM microphysics scheme calculates radar reflectivity with the following assumptions:

- Rayleigh scattering is assumed, which is valid for longer wavelength radars such as those in the S-band.
- The bright band is not explicitly modelled as the microphysical scheme may not include processes to model this phenomenon, although different dielectric constants are used for different hydrometeor categories.
- Attenuation is not accounted for and the calculation makes no assumption on the location of the radar, apart from assuming a 0° elevation angle.

5.1.2 Wilson-Ballard

In the single moment microphysics scheme, rain reflectivity is calculated based on Stein et al. (2014), McBeath et al. (2014) and Gaussiat (2008). As Rayleigh scattering is assumed, reflectivity is considered proportional to hydrometeor mass squared. The radar reflectivity for rain in units of $\mathrm{mm}^6\,\mathrm{m}^{-3}$ is

$$Z_{\mathrm{H\ rain}} = \mathcal{R}_{\mathrm{rain}} \int_0^\infty \left[M_{\mathrm{rain}}(D)\right]^2 n_{\mathrm{rain}}(D) dD \tag{5.3}$$

where $M_{\mathrm{rain}}(D)$ is the mass of a raindrop of diameter D. The dielectric constant of liquid water $|K_{\mathrm{rain}}|^2$ and its density ρ_w are encoded within the constant $\mathcal{R}_{\mathrm{rain}}$.

$$\mathcal{R}_{\mathrm{rain}} = 10^{18} \frac{|K_{\mathrm{rain}}|^2}{0.93} \left(\frac{6}{\pi \rho_{\mathrm{rain}}}\right)^2 \tag{5.4}$$

The factor of 10^{18} accounts for conversion from $\mathrm{m}^6\,\mathrm{m}^{-3}$ to $\mathrm{mm}^6\,\mathrm{m}^{-3}$. The constant 0.93 is the dielectric constant of water at centimeter wavelengths, which scales the quantity into an equivalent radar reflectivity factor. The factor $\frac{6}{\pi \rho_{\mathrm{rain}}}$ converts mass into diameter of a spherical drop. Following the assumption of a spherical drop, the mass-diameter relationship implies that the mass of a raindrop will be the density of liquid water multiplied by the volume of a sphere of diameter D.

$$M_{\text{rain}} = \frac{\pi}{6}\rho_{\text{rain}} D^{b_{\text{rain}}} \tag{5.5}$$

where b_{rain} is defined in Table 5.1.

The MetUM uses a modified gamma particle size distribution to describe raindrops. Note that this is not a forward operator assumption, but already parametrised in the microphysical scheme of the MetUM.

$$n_{\text{rain}} = n_{a\ \text{rain}} \lambda_{\text{rain}}^{n_{b\ \text{rain}}} D^{\alpha_{\text{rain}}} e^{-\lambda_{\text{rain}} D} \tag{5.6}$$

For this single moment microphysics scheme, the product of the first two factors makes up the intercept parameter, which is assumed to be a simple function of λ_{rain}, instead of using a constant intercept parameter such as in Marshall and Palmer (1948). Abel and Boutle (2012) used observations to develop this improved parametrization of the raindrop size distribution to better capture raindrop sizes within convective showers and stratocumulus clouds. Parameters for the equations above are given in Table 5.1.

Parameter	Value
$\lvert K_w \rvert^2$	0.93
ρ_w	$1000\,\text{kg}\,\text{m}^{-3}$
α_{rain}	0
$n_{a\ \text{rain}}$	0.22
$n_{b\ \text{rain}}$	2.2
a_{rain}	$\frac{\pi}{6}$
b_{rain}	3

Table 5.1: Parameters used in the Met Office Unified Model for simulating rain reflectivity.

The variable λ_{rain} can be derived through the rain water content in grid box W_{rain} from the rain mass mixing ratio q_r.

$$W_{\text{rain}} = \frac{q_r \rho_{\text{air}}}{C_{\text{rain}}} \tag{5.7}$$

in which C_{rain} is the grid fraction occupied by rain. Since rain water content is the integral of mass over the particle size spectrum, otherwise known as the first-moment

of mass, the quantity can be calculated as

$$W_{\text{rain}} = \int_0^\infty M_{\text{rain}}(D) n_{\text{rain}}(D) dD$$
$$= a_{\text{rain}} N_{0\ \text{rain}} \Gamma(b_{\text{rain}} + 1 + \alpha_{\text{rain}}) \lambda_{\text{rain}}^{-(b_{\text{rain}}+1+\alpha_{\text{rain}}-n_{b\ \text{rain}})} \tag{5.8}$$

Integrating and rearranging the expression for rain water content gives shape parameter λ_{rain}.

$$\lambda_{\text{rain}} = \left[\frac{N_{0\ \text{rain}} a_{\text{rain}} \Gamma(b_{\text{rain}} + 1 + \alpha_{\text{rain}})}{W_{\text{rain}}} \right]^{1/(b_{\text{rain}}+1+\alpha_{\text{rain}}-n_{b\ \text{rain}})} \tag{5.9}$$

Substituting the mass-diameter relationship (Equation (5.5)) and particle size distribution (Equation (5.6)) into the expression for rain radar reflectivity (Equation (5.3)) and integrating gives

$$Z_{\text{H rain}} = C_{\text{rain}} \mathcal{R}_{\text{rain}} N_{0\ \text{rain}} a_{\text{rain}}^2 \Gamma(1 + 2b_{\text{rain}} + \alpha_{\text{rain}}) \lambda_{\text{rain}}^{-(1+2b_{\text{rain}}+\alpha_{\text{rain}}-n_{b\ \text{rain}})} \tag{5.10}$$

This approach allows for the simulation of rain radar reflectivity $Z_{\text{H rain}}$ using q_{rain} and C_{rain} fields and other parameters already assumed within the Wilson-Ballard single moment microphysics scheme of the MetUM. Simulated rain radar reflectivity within the Wilson-Ballard scheme is defined completely by q_{rain}, and nothing else that is not already known or diagnosed by the MetUM.

5.1.3 CASIM

In addition to rain mass mixing ratio, CASIM also prognoses the number concentration of raindrops N_{rain}, otherwise known as the zeroth moment of mass.

$$N_{\text{rain}} = \int_0^\infty n_{\text{rain}}(D) dD \tag{5.11}$$

The rain drop size distribution is similar to that of Wilson-Ballard, but with an intercept parameter $n_{0\ \text{rain}}$ that is prognosed by the model rather than parametrised by λ_{rain}. Also note that α_{rain} is now fixed at 2.5 (Field et al., 2023), rather than 0.

$$n_{\text{rain}} = n_{0\ \text{rain}} D^{\alpha_{\text{rain}}} e^{-\lambda_{\text{rain}} D} \tag{5.12}$$

Thus, integrating Equation (5.11) gives us the number concentration of raindrops as

$$N_{\text{rain}} = n_{0\ \text{rain}} \Gamma(\alpha_{\text{rain}} + 1) \lambda_{\text{rain}}^{-(\alpha_{\text{rain}}+1)} \tag{5.13}$$

Similar to Equation (5.8), the rain water content is

$$W_{\text{rain}} = a_{\text{rain}} n_{0\ \text{rain}} \Gamma(b_{\text{rain}} + 1 + \alpha_{\text{rain}}) \lambda_{\text{rain}}^{-(b_{\text{rain}}+1+\alpha_{\text{rain}})} \tag{5.14}$$

Dividing Equation (5.14) by Equation (5.11) and rearranging, we get an expression for λ_{rain} without dependence on the intercept parameter $n_{0\ \text{rain}}$.

$$\lambda_{\text{rain}} = \left[a_{\text{rain}} \frac{\Gamma(b_{\text{rain}} + \alpha_{\text{rain}} + 1)}{\Gamma(\alpha_{\text{rain}} + 1)} \frac{N_{\text{rain}}}{W_{\text{rain}}} \right]^{1/b_{\text{rain}}} \tag{5.15}$$

To then solve for the intercept parameter, Equation (5.11) is inverted.

$$n_{0\ \text{rain}} = \frac{N_{\text{rain}} \lambda_{\text{rain}}^{(\alpha_{\text{rain}}+1)}}{\Gamma(\alpha_{\text{rain}} + 1)} \tag{5.16}$$

Reflectivity for rain derived using CASIM is thus

$$\begin{aligned} Z_{\text{H rain}} &= C_{\text{rain}} \mathcal{R}_{\text{rain}} n_{0\ \text{rain}} a_{\text{rain}}^2 \Gamma(1 + 2b_{\text{rain}} + \alpha_{\text{rain}}) \lambda_{\text{rain}}^{-(1+2b_{\text{rain}}+\alpha_{\text{rain}})} \\ &= C_{\text{rain}} \mathcal{R}_{\text{rain}} a_{\text{rain}}^2 N_{\text{rain}} \frac{\Gamma(1 + 2b_{\text{rain}} + \alpha_{\text{rain}})}{\Gamma(\alpha_{\text{rain}} + 1)} \lambda_{\text{rain}}^{-2b_{\text{rain}}} \end{aligned} \tag{5.17}$$

This approach allows for the simulation of rain radar reflectivity $Z_{\text{H rain}}$ using q_{rain}, n_{rain} and C_{rain} fields and other parameters already assumed within the CASIM's double moment microphysics scheme of the MetUM. Simulated rain radar reflectivity within the CASIM scheme is defined completely by two diagnostic variables n_{rain} and q_{rain}, and nothing else that is not already known or diagnosed by the MetUM. The quantity is not a one-to-one function of q_{rain}.

5.2 Forward Operator Design

The current formulations for simulating radar reflectivity in both a single moment and double moment microphysics scheme are carried out online in the MetUM. Despite being simple and convenient, the forward model's assumptions are inappropriate for simulating polarimetric radar variables within severe convection.

As establisbed in the previous section, the MetUM simulates rain reflectivity by assuming Rayleigh scattering for spherical raindrops. It is unable to simulate backscatter including non-Rayleigh effects from UK C-band radars when sensing millimetre-sized hydrometeors in the Mie regime. The pre-existing forward operator assumes spherical raindrops and thus fails to simulate any non-zero Z_{DR}. To address these two shortcomings in the MetUM's forward operator, we need to design a forward operator that calculates scattering numerically without assuming the Rayleigh

regime and decide on a drop shape model to account for the non-sphericity of large raindrops.

5.2.1 Scattering Calculations

Lorenz (1890), Mie (1908) and Debye (1909) derived the scattering solution for an isotropic homogeneous dielectric sphere, otherwise known as Lorenz-Mie theory. The formalism allows the calculation of the scattered electric and magnetic fields for particle sizes comparable to that of the incident electromagnetic wavelength. To account for the non-spherical geometry of hydrometeors, Gans theory (Gans, 1912) can be used to extend Rayleigh scattering theory to spheroidal particles. An example of its use assuming an aspect ratio model by Pruppacher and Beard (1970) is demonstrated in Seliga and Bringi (1976). The theory still assumes Rayleigh scattering, which is simple and economic for computing scattering amplitudes. However, a radar forward operator should also account for Mie scattering and be able to assume an aspect ratio of raindrops with different sizes.

To extend the Lorenz-Mie formalism to particles of various shapes, Mishchenko (2000) developed code to compute a transition matrix (T-matrix) for simple particles based on the extended boundary condition method. Incident and scattered waves are decomposed into an orthogonal set of vector spherical wave functions. The expanded wave components of the incident and scattered waves are then related by the T-matrix. Such an approach is currently one of the most powerful and widely used tools for the rigorous computation of electromagnetic wave scattering by particles of certain geometries such as oblate spheroids.

The PyTMatrix package (Leinonen, 2014) is invoked here to perform T-matrix calculations. A refractive index and axis ratio function is specified to calculate amplitude matrices for backscatter cross-section from a single scatterer over a range of sizes. An amplitude matrix linearly transforms the incident electric field vector components into components of the scattered wave. The refractive index of water is calculated using the model by Turner et al. (2016). Finally, particle size distribution-integrated quantities such as radar reflectivities are calculated by numerically integrating the radar cross section contributions over the particle size distribution as per Equation (5.1).

5.2.2 Comparison between Rayleigh and non-Rayleigh

To quantify the deviation from not using Rayleigh scattering, we proceed with comparing their outputs.

We first tested the forward modelled reflectivity Z_{H} in forward operators suitable for a single moment microphysics scheme, such as the MetUM's Wilson and Ballard

(1999) scheme. Assuming a grid rain fraction of 1 and taking the mass rain fraction of rain q_{rain} as input, Figure 5.2 shows how forward-modelled Z_{H} changes with q_{rain} assuming spherical raindrops for various scattering assumptions. All simulated Z_{H} increase with q_{rain}. For small q_{rain} below $5 \times 10^{-4}\,\text{kg}\,\text{kg}^{-1}$, all Z_{H} values converge as expected for scattering dominated by small particles. In other words, Rayleigh scattering should provide a fair approximation for T-matrix scattering calcuations for small-size parameters.

Forward modelled Z_{H} calculated using Rayleigh-Gans theory diverges from Z_{H} calculated using Rayleigh theory. This is due to the use of finite numerical integration of drop size distribution up to 1 cm to accommodate the piecewise aspect ratio function in Seliga and Bringi (1976), although all aspect ratios were set to 1.0 in this test of sperical hydrometeors. Numerical integration is in contrast to the analytical method of integrating a drop size distribution from zero to infinity in the Rayleigh scattering forward operator. To test this artefact of numerical integration with a finite upper limit, we implemented numerical integration of the drop size distribution with an upper limit of 1 cm for the Rayleigh forward operator (black dotted line) and find it produces identical Z_{H} values as the Rayleigh-Gans forward-model (blue).

For larger q_{rain} such as $1 \times 10^{-3}\,\text{kg}\,\text{kg}^{-1}$, Z_{H} calculated using the T-matrix method (red) diverges from other lines, as it captures Mie scattering phenomena such as Mie resonance in contrast to the other forward operators, which all operate in the Rayleigh scattering regime.

5.2.3 Aspect Ratio

Because the cross-sectional area in the horizontal and vertical direction are the same, spherical raindrops will only yield zero differential reflectivity Z_{DR}. The MetUM lacks explicit parameters describing the aspect ratio of raindrops. Hence, we have to introduce aspect ratio models sourced from the literature that are usually based on observations and lab experiments. Having tested our forward operator on spherical raindrops, we now try the forward operators on more realistic raindrops modelled as homogeneous oblate spheroids by implementing three different aspect ratio models. An aspect ratio that is not constrained to 1.0 should give a non-zero Z_{DR} and allow us to simultaneously investigate simulated Z_{H} and Z_{DR}.

Figure 5.3 presents a number of aspect ratio models, showing how each of their aspect ratio changes with increasing equivalent volume diameter of a raindrop. The equivalent volume diameter is the diameter of a sphere that has the same volume as the actual non-spherical raindrop. Green (1975) developed a model for raindrop deformation that accounts for the effects of surface tension and drop size. Brandes et al. (2002) conducted an experiment to determine the impact of different drop

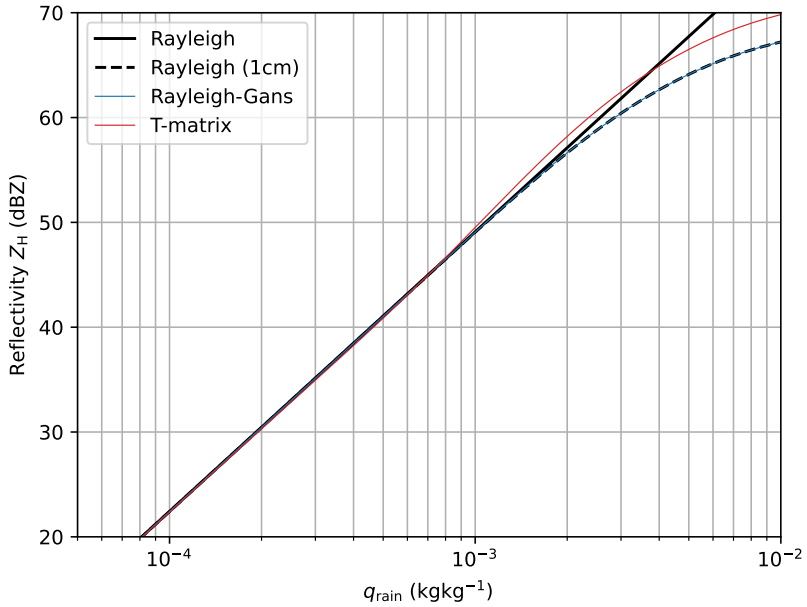

Figure 5.2: Forward modelled reflectivity Z_{H} against against rain mass fraction q_{rain} for spherical raindrops. Black solid line is the MetUM's forward operator assuming Rayleigh scattering. Dotted line truncates particle size distribution at 1 cm. Blue and red lines are results from using Rayleigh-Gans and T-matrix scattering formulations respectively.

shapes on the value of disdrometer-derived Z_{DR}. They combined observations from multiple studies to derive an empirical relation between aspect ratio and equivalent-volume drop diameter. Although the relation results in similar aspect ratios as the Green (1975) model for drops up to 4 mm, larger drops deviate significantly from other models in that they are more oblate. At first glance, such a deviation may seem to have a large effect on the drop shape model. However, it is worth noting that Brandes et al. (2002) likely did not observe many large drops beyond a few millimetres as their disdrometer Z_{DR} data are all below 3 dB and they admit that their model deviates from observations in other studies for large drops exceeding 5 mm in diameter. Thus, we should not expect their model to work well for very large drop sizes. Andsager et al. (1999) also shows a large deviation from other drop shape models, as it is limited to drops smaller than 4.4 mm of diameter. Using a two-dimensional video disdrometer, Thurai et al. (2007) constructed contour shapes of raindrops in an 80 m fall experiment. They were able to find appropriate aspect ratio models from two previous studies to construct a piecewise aspect ratio model assuming spheres if the equivalent diameter was smaller than 0.7 mm.

In Figure 5.4, we investigate the effects of forward-modelled Z_{DR} with rain mass fraction q_{rain} for different aspect ratio models and scattering computation methods. For spheres, Z_{DR} is zero as expected for all values of q_{rain}. All aspect ratio models

produce comparable Z_{DR} values within 0.2 dB up to q_{rain} of $8 \times 10^{-4}\,\mathrm{kg\,kg^{-1}}$. Most drop models yield similar Z_{DR} for values above 1 dB with the exception of two shape models owing to limitations of their studies. It is clear that the forward operator is not sensitive to the choice of aspect ratio models especially for large q_{rain} values. The drop shape model in Thurai et al. (2007) that considers drop sizes up to 10 mm will be used.

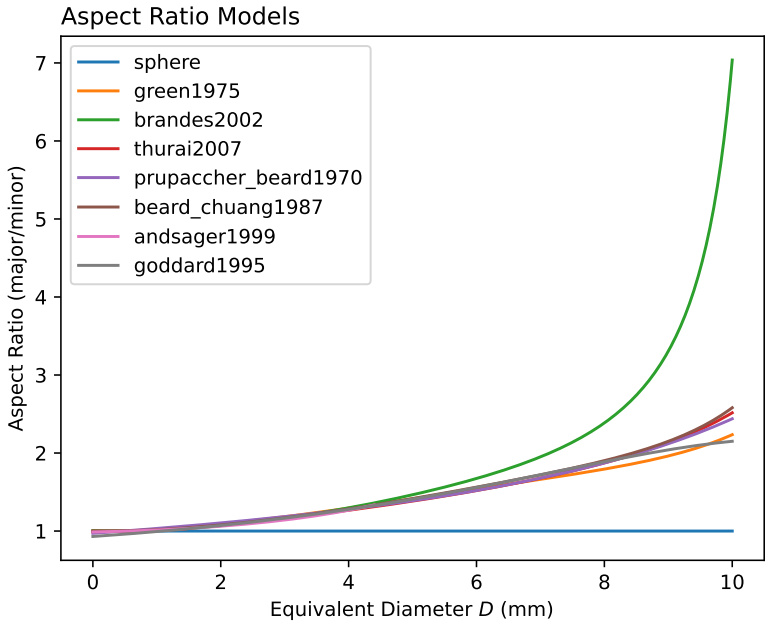

Figure 5.3: Aspect ratio against equivalent raindrop diameter for various aspect ratio models. Note that the Andsager et al. (1999) aspect ratio model is truncated at 4.4 mm of diameter.

5.2.4 Canting Angle

A raindrop's orientation changes under the effect of turbulence and windshear. This phenomenon has been theorised (e.g. Beard and Jameson, 1983) and observed (e.g. Brunkow, 2008) in past studies. The increased canting of drops within a radar sampling volume dampens the horizontal backscatter component and increases the vertical backscatter component, thus giving lower Z_{DR}. To understand the implication of drop canting, we assume that drop canting angles are normally distributed with a mean of zero and test the effect of increasing the canting angle Gaussian distribution width. Figure 5.5 shows Z_{DR} against q_{rain} for the T-matrix scattering formulation with increasing Gaussian widths of canting angle distributions. Out of the five different canting angle distribution widths tested, the widest distribution gave the lowest Z_{DR} values as expected. At the maximum q_{rain}, canting distribution widths can cause differences of about 2 dB. On theoretical grounds, Beard and

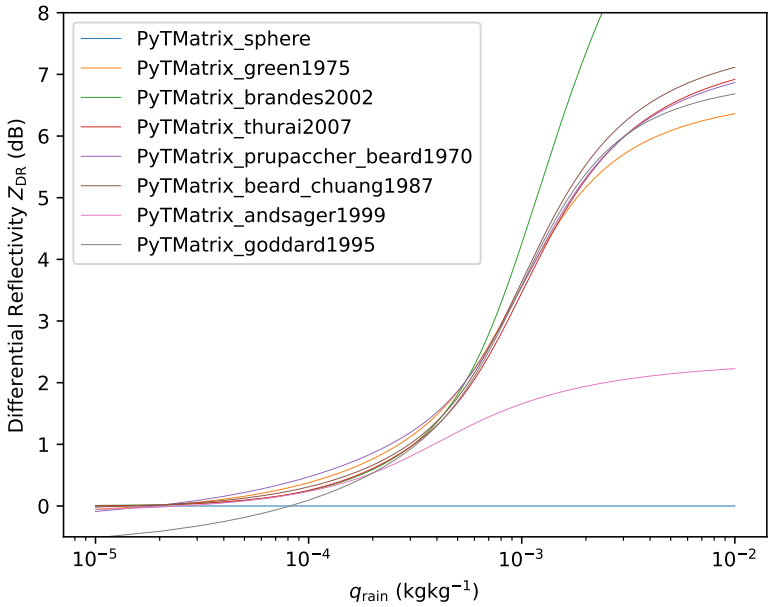

Figure 5.4: Forward modelled differential reflectivity Z_{DR} against rain mass fraction q_{rain} given in a single moment microphysics scheme for different scattering theory and aspect ratio model configurations.

Jameson (1983) showed that the Gaussian canting angle model is valid with a mean of 0° and standard deviation less than 5°. Also assuming a Gaussian model, Hendry et al. (1987) estimated a standard deviation of 6° from observing a large swing in the cross-polar power as the direction of the transmitted linear polarization was varied. Considering both studies and that there are minimal effects on Z_{DR} between setting the canting distribution width to 0 or 5°, a 0° canting distribution width is thus a reasonable choice for the forward operator.

5.2.5 Double Moment Microphysics

For testing forward operators taking in both q_{rain} and n_{rain} from a double moment microphysics scheme, we set up configurations to using the Thurai et al. (2007) aspect ratio model with reasons justified from testing forward operator configurations for a single moment microphysics scheme.

Figure 5.6 shows simulated Z_{DR} values for given values of raindrop number concentration per kilogram of air n_{rain} and rain mass fraction q_{rain}. For a given rain mass fraction, Z_{DR} decreases with increasing n_{rain}. The greater the n_{rain}, the larger the value of λ_{rain} in Equation (5.15). The mass-weighted mean diameter of drops is defined as the ratio of the fourth moment and the third moment of the dropsize distribution. For a gamma dropsize distribution, the mass-weighted mean diameter

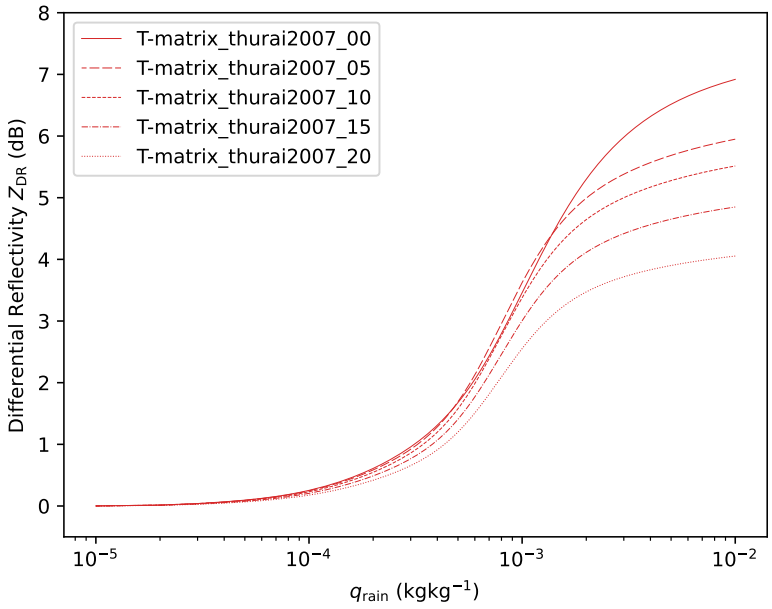

Figure 5.5: Forward modelled differential reflectivity Z_{DR} against rain mass fraction q_{rain} for T-matrix method with canting angle distribution widths ranging from 0 to 20°.

can be expressed in terms of variables describing the gamma distribution as shown.

$$D_m = \frac{\int_0^\infty D^4 n(D)\, dD}{\int_0^\infty D^3 n(D)\, dD} \tag{5.18}$$

$$= \frac{\alpha + 4}{\lambda} \tag{5.19}$$

Hence, a larger λ_{rain} would signify a smaller mean drop diameter. In other words, if a mass of water is distributed amongst more drops, each drop will have a lower volume and thus a smaller equivalent diameter. Such small drops will have an aspect ratio closer to 1 resembling more spherical scatterers thus giving a lower Z_{DR}.

5.3 Implementation

Running the T-matrix code for every model grid point would be computationally infeasible. Lookup tables are used instead as they are convenient and efficient as long as parameters in the forward operator are unperturbed. The lookup tables generated assume a nominal scatterer temperature of $-10\,^{\circ}\mathrm{C}$ as we are interested in super-cooled raindrops within Z_{DR} that extend in height above the freezing level. The Thurai et al. (2007) aspect ratio model is employed with the assumption of zero width in the drop canting distribution centred about 0°.

For the Wilson-Ballard single moment microphysics scheme, one-dimensional

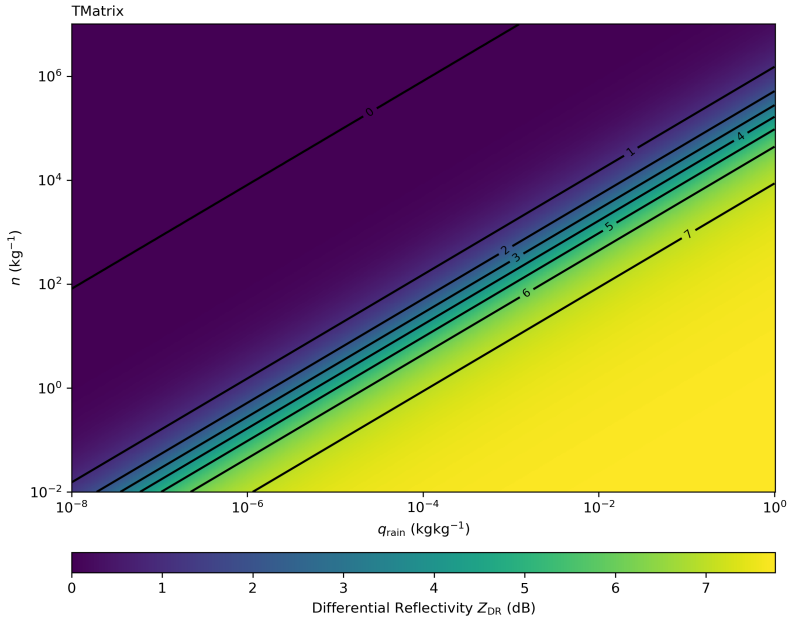

Figure 5.6: Simulated Z_{DR} for given inputs from the CASIM microphysics scheme.

lookup tables are generated with the input being rain water content W_{rain}. This is related to rain mass fraction q_{rain} which was used when testing the forward operator.

$$W_{\text{rain}} = \frac{q_{\text{rain}}\rho_{\text{air}}}{C_{\text{rain}}} \tag{5.20}$$

The use of W_{rain} removes the lookup table's dependence on the density of air ρ_{air} and the grid fraction of rain C_{rain}. The lookup points are logarithmically spaced between 1×10^{-8} to $1\,\text{kg}\,\text{m}^{-3}$ with 500 bins.

A two-dimensional look up table is generated for the CASIM double moment scheme with the inputs being W_{rain} and raindrop concentration N_{rain} in units of per cubic metre of air. The lookup points on the W_{rain} axis are spaced as far as in the forward operator lookup table for the Wilson-Ballard scheme. On the second axis of the lookup table, raindrop concentration N_{rain} per unit volume of air is used, in contrast to raindrop concentration per unit mass of air.

$$N_{\text{rain}} = \frac{n_{\text{rain}}\rho_{\text{air}}}{C_{\text{rain}}} \tag{5.21}$$

Similarly, the use of raindrop concentration in units of per cubic metre removes the lookup table's dependence on the density of air ρ_{air} and the grid fraction of

rain C_{rain}. The lookup points on the N_{rain} axis are logarithmically spaced between 1×10^{-2} to $1 \times 10^{7}\,\text{m}^{-3}$ against 500 bins. The bounds of lookup tables were informed by the likely minimum and maximum values possible from the model. The spacing of points in the lookup table ensures a precision of better than 1.0 dBZ and 0.1 dB of Z_{H} and Z_{DR} respectively. Such precisions are comparable with those of observations from the radar composite.

Once Z_{H} and Z_{DR} are calculated at a nominal temperature of $-10\,^{\circ}\text{C}$, a first order correction is applied to account for differences in refractive index of liquid water. The resulting corrected Z_{DRT} is calculated as:

$$Z_{\text{DRT}} \approx Z_{\text{DR}} + \frac{dZ_{\text{DR}}}{dT}\Delta T \tag{5.22}$$

where ΔT is the air temperature in the model grid box minus the nominal temperature of $-10\,^{\circ}\text{C}$. The derivative $\frac{dZ_{\text{DR}}}{dT}$ is estimated from linear regression of Z_{DR} against T at a range of temperatures from -20 to $25\,^{\circ}\text{C}$ in 5 degC steps for each grid point in the lookup tables. This correction scheme estimates Z_{DR} values for warmer or colder temperatures that are up to 0.2 dB different than if values were calculated directly at that warmer or colder temperature. Without this temperature correction, there could be biases of up to 2 dB in both Z_{H} and Z_{DR}.

5.4 Online Testing

Once the forward operator was implemented within the MetUM, the rain reflectivity field generated by the forward operator is compared with the rain reflectivity field that was already calculated by the MetUM via the Rayleigh scattering assumption. The evaluation of simulated Z_{H} and Z_{DR} against observations will take place in Chapter 6.

Figure 5.7 shows simulated radar reflectivity from rain alone for both the RA2M and RAL3.1 configurations that run the single moment Met Office-modified Wilson and Ballard (1999) and double moment CASIM (Field et al., 2023) microphysical schemes respectively. The simulated fields from the MetUM assuming Rayleigh scattering and the implementation of PyTMatrix as a lookup table are comparable at 1 km model height with most grid points showing zero difference. As seen in Figure 5.8, the median in the difference fields are at most 0.3 dBZ for all MetUM simulated reflectivity values below 40 dBZ for both RA2M and RAL3.1. The median difference value increases to 3.5 dBZ and 2.4 dBZ when the MetUM simulates reflectivity values of 55 dBZ. A difference of a few decibels between the two methods of simulation is expected from Mie effects as highlighted in Section 5.2.2.

Figure 5.9 show fields of q_{rain}, Z_{H} and Z_{DR} at 1 km in height for simulations

coupled to Wilson-Ballard (RA2M) and CASIM (RAL3.1). The plotted regions spanning approximately an area of 33 km × 33 km were chosen to show regions of heavy rain where one should expect enhanced Z_{DR} values. Larger values of q_{rain} clearly result in higher values of Z_{H} and Z_{DR} in the Wilson-Ballard simulation as expected. The CASIM simulation also shows a collocation between areas of large q_{rain} and enhanced Z_{H} and Z_{DR}.

The testing carried out shows that the implemented forward operator produces simulated output as expected and is now ready to be used for comparison with observations.

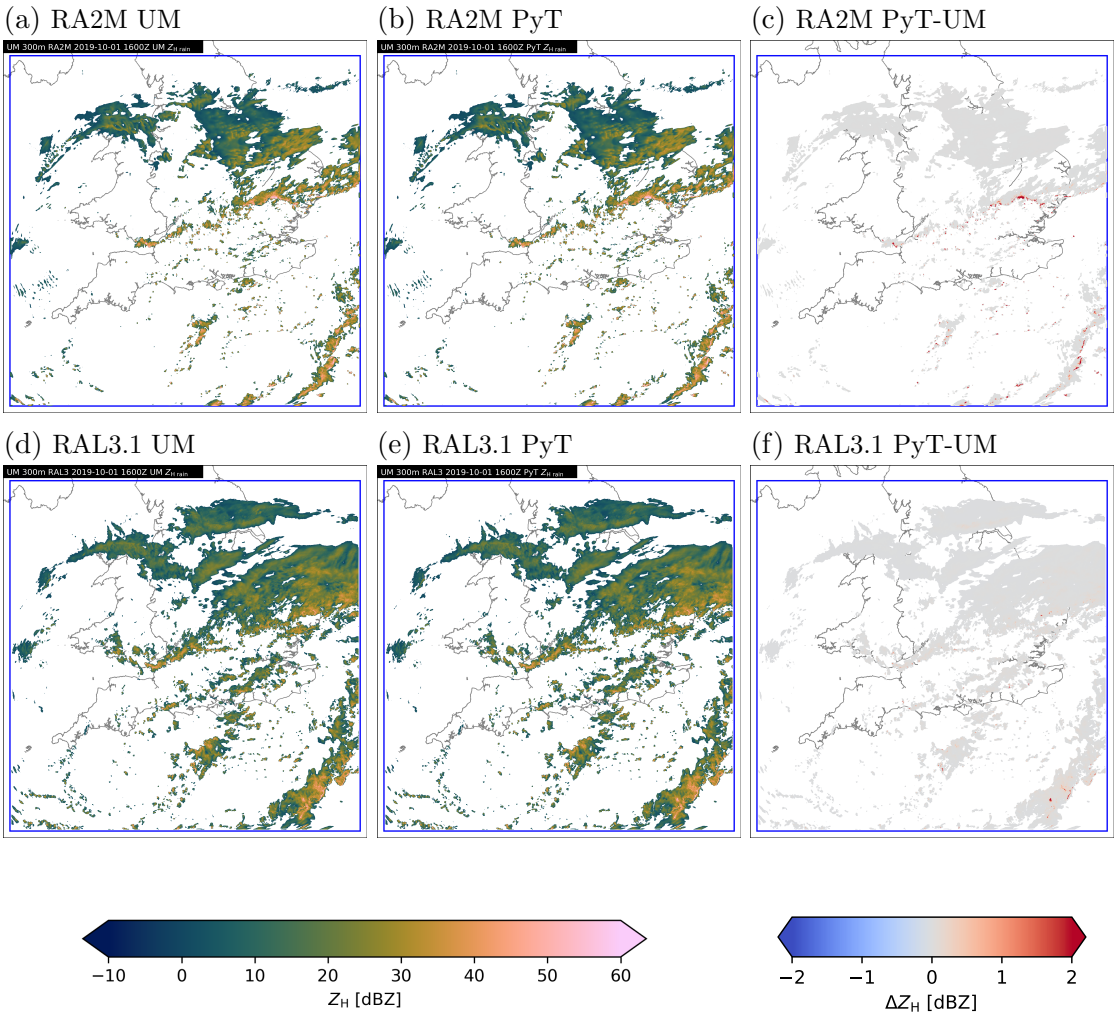

Figure 5.7: Simulated radar reflectivity fields at 1km model height for both the RA2M (top) and RAL3.1 (bottom) configurations using the Rayleigh scattering assumption within the MetUM (first column), PyTMatrix (second column) and their difference field (final column).

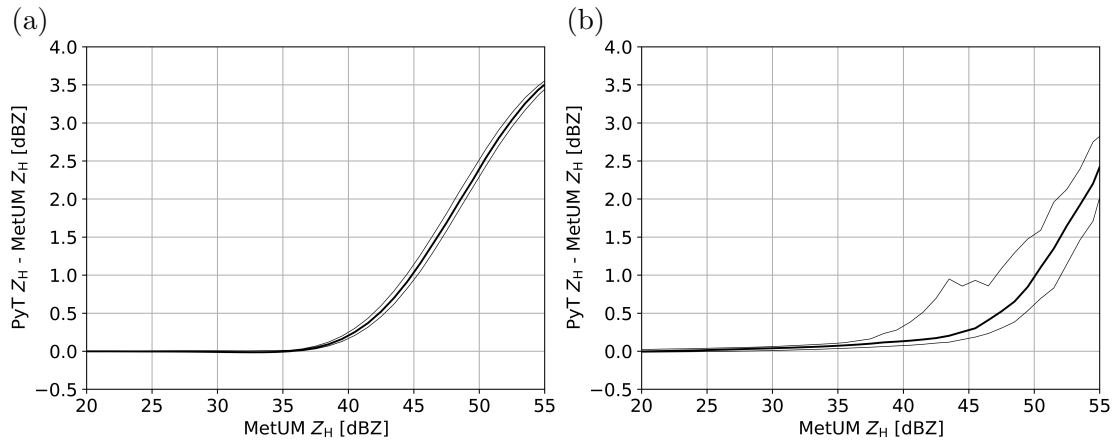

Figure 5.8: Median, 10 and 90-th percentile differences of rain Z_H between PyT-matrix and MetUM forward operators.

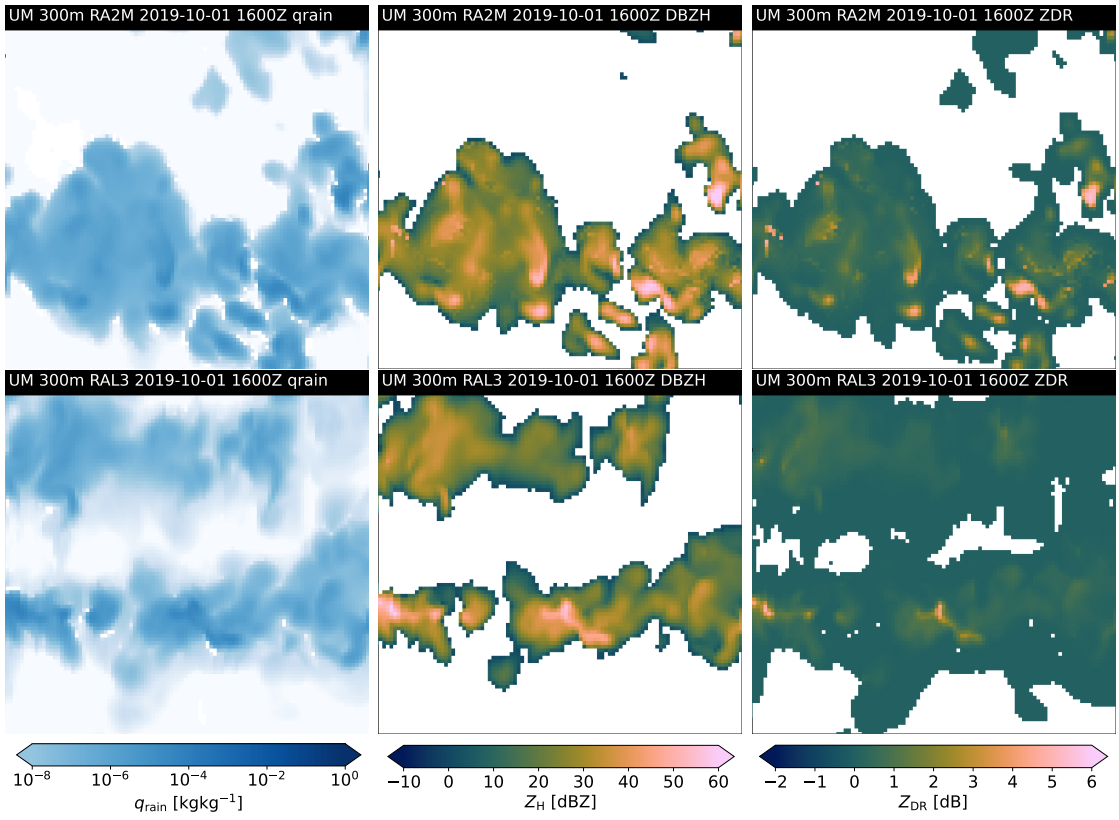

Figure 5.9: RA2M (top row) and RAL3.1 (bottom row) simulation outputs at 1 km in height showing q_{rain} (left column), Z_H (middle column) and Z_{DR} (right column) fields for 33 km × 33 km regions.

5.5 Summary and Conclusions

Current forward operator formulations within the MetUM for both the Wilson-Ballard and CASIM microphysical schemes were derived in full to understand their assumptions and parametrisations. The Rayleigh scattering and spherical hydrometeor assumptions used to derive the MetUM's simulated radar reflectivity field were challenged. Rayleigh scattering was shown to be inappropriate for simulating C-band radars scanning a volume that potentially contained large raindrops, since such millimetre-sized drops have a size parameter that lies within the Mie scattering regime. Furthermore, the spherical assumption will result in zero Z_{DR} being produced, which would suppress any possibility for a Z_{DR} column to be simulated.

The T-matrix scattering method was introduced as an appropriate scattering formulation, which accounts for Mie scattering effects and non-spherical hydrometeors using the PyTMatrix software. The T-matrix formulation was found to produce similar simulated reflectivity values with the MetUM's forward operator for small rain mass fractions and reflectivity values reaching 40 dBZ. Differences at higher reflectivities could be explained by Mie scattering effects and by numerically integrating a discretised particle size distribution up to a finite diameter of 1 cm. Other sensitivity tests on variables not modelled within the MetUM were also investigated. The use of aspect ratio models could result in Z_{DR} differences especially for simulated values exceeding 3.0 dB. An increasing canting angle distribution width could potentially reduce Z_{DR} by around 2.0 dB for extreme values of Z_{DR}. From these sensitivity tests, the Thurai et al. (2007) aspect ratio model was selected with no width in canting angle distribution. In other words, it is assumed that all raindrops have a canting angle of zero.

Considering the computational resources required for the T-matrix method, the forward operator was implemented in the form of lookup tables within the MetUM. This allowed quick calculations of Z_{H} and Z_{DR} from rain for the entirety of the model domain. Owing to the sensitivity of the scatterer dielectric constant to temperature, a first-order temperature correction is also applied to both simulated radar variables.

A brief comparison was made between the original simulated reflectivity field from the MetUM and that using the T-matrix method. Nearly all model grid points show a near-zero reflectivity bias. Deviations of less than a few dB are expected for the reflectivity values exceeding 40 dBZ due to differences in the Rayleigh scattering assumption and the T-matrix method.

The forward operator implemented in this chapter is a first step in exploiting the UK C-band polarimetric radar network for the purposes of model evaluation. The Z_{DR} detection algorithm described in Chapter 4 when applied to the radar composite highlights the presence of Z_{DR} columns. With the new forward operator,

the presence of observed Z_{DR} columns can be directly compared with simulated Z_{DR} signatures from rain within the MetUM.

Chapter 6

Evaluation of Z_{DR} in the Unified Model

6.1 Introduction

This chapter presents the evaluation of the MetUM using Z_{DR}. The model configurations are described in detail in Section 2.4.2. In brief, a horizontal grid length of 300 m is chosen as a compromise between the ability to represent the updraft strength and size to loft raindrops and the computational expenses required. The simulation domain is nested within a larger simulation of 1.5 km grid length, which is initialised by archived global model data. Four simulations, namely RA2M, RAL3.1, RAL3.1WB, and RAL3.1NB were carried out. RA2M is an operational configuration that implements the Wilson-Ballard single moment microphysics scheme, whereas RAL3.1 is a near-operational configuration that implements the CASIM double moment microphysics scheme alongside other model physics changes. To isolate differences arising from using a different microphysics scheme, RAL3.1WB has identical model physics as RAL3.1 except that it implements Wilson-Ballard single moment microphysics. RAL3.1NB has identical model physics as RAL3.1 except that the Bigg (1953) process is turned off within CASIM. Hourly outputs of certain three-dimensional fields are available from the model simulations, including radar fields simulated by the implemented forward operator described in Chapter 5. The simulated Z_{DR} field provides further insight into the modelled rain formation processes within the MetUM, hence allowing researchers to verify whether the model represents these correctly through comparison with observations. Cases of interest that could utilise simulated Z_{DR} include frontal precipitation and warm rain (not studied in this thesis), as well as convective storms which is the subject of this thesis.

The chapter is organised as follows: Section 6.2 describes the case day studied using outputs produced by the three-dimensional radar composite and from various MetUM run configurations that will be described in this section. Using the forward operator described in Chapter 5, the microphysical variables that are mapped to simulated radar observables are shown in Section 6.3, including a comparison be-

tween MetUM simulations and the radar composite. The presence of simulated Z_{DR} columns is then explored in Section 6.4. The chosen cross sections reveal a discrepancy between rain contributions to Z_{DR} columns between model configurations, which is investigated further by analysing updraft magnitudes in Section 6.5 and the vertical distribution of hydrometeor species in Section 6.6. Finally, summary and conclusions are given in Section 6.7.

6.2 Case Overview

On 1st October 2019, a depression and upper vortex moved eastwards across the UK as seen in Figure 6.1. An associated frontal zone advected slowly southwards. A moist, deeply unstable environment was present ahead of this frontal zone, bringing unsettled weather to the southern part of England. From the maximum reflectivity field of the radar composite valid at 1600Z in Figure 6.3a, convective cells can be seen within or near the upper vortex centre with some linear organisation in the east-west direction associated with the occluded front and low-level convergence. There is also a prevalence of Z_{DR} columns at this time as seen in Figure 6.3b.

Figure 6.2 shows the domain-averaged rainfall rate across three MetUM simulations and the 1 km resolution rainfall product derived from the Met Office Nimrod system. The common domain for averaging rainfall rate and for any analyses described in this chapter is shown by the plot extents of Figure 6.5. The domain covers parts of England affected by signficant rainfall rates associated with the line convection feature that was both simulated by the MetUM and observed by the dense coverage of radars in the area. The domain is situated well away from the spatial boundaries of the MetUM simulations to avoid contamination from the lateral boundary conditions provided by one-way nesting of the 1.5 km-resolution model.

The MetUM simulations and the Nimrod-derived observations begin with nearly no rainfall to areas of drizzle in the early hours of the case day. At 0500Z, Nimrod observes individual convective cells that begin to organise, whereas the MetUM runs already produce intense cells with some linear organisation in southern England. The first peak in Nimrod occurs at 0800Z with large stratiform rain areas covering the southwest (Figure 6.4a). The models then show the day's maximum close to noon when numerous intense convective cells are generated along and in front of the line convection feature that advects southwards (Figure 6.4d). Embedded convection is also simulated within the widespread stratiform region behind the line convection. At this time, Nimrod observes mostly isolated intense single cells that have begun to organise (Figure 6.4c). The dominant flow changes from southwesterly to northwesterly in both models and observations at around 1200Z. In the

afternoon hours, the Nimrod domain-averaged rainfall nearly reaches $1.0\,\mathrm{mm\,h^{-1}}$ as seen from an abundance of intense convection developing at the leading edge of the line convection feature in Figures 6.4e and 6.5a. As for the model simulations, rainfall is underestimated in the afternoon (Figure 6.4f), regardless of configuration. Towards the latter part of the evening, the heavy precipitation associated with the depression weakens and clears away to the southeast of the domain for both model and observations.

The discrepancy in timing and intensity of severe convective features between the MetUM and radar observations makes this a complicated case study. Considering that highest observed rainfall rates and organisation of the line convection feature were centred in the common domain at 1600Z of the case day, radar composite and model outputs were selected at this time for further analysis.

6.3 Comparing radar variables

To show that the radar forward operator developed in Chapter 5 functions as expected, the joint distribution of simulated Z_{H} and Z_{DR} contributions from rain is investigated for each model simulation. These simulated values can also be compared with observed radar variables from the radar composite.

Figure 6.6a shows the joint distribution of Z_{H} and Z_{DR} from the radar composite. The joint distribution is for the radar composite, so it includes both rain and frozen hydrometeors, as well as regions with low signal to noise ratio. There is a mode of composite grid points with Z_{H} of 20 dBZ and Z_{DR} of 0.2 dB. For low values of Z_{H} below 10 dBZ, the range of Z_{DR} values increases to around 3.0 dB. These are regions of low signal to noise ratio particularly near the cloud tops and edges, giving rise to higher uncertainties in the Z_{DR} measurement. Secondly, higher heights in the radar composite are normally covered by lower elevation scans at greater range, hence the greater sampling volume. Non-uniform beam filling effects within these large sampling volumes could lead to positive and negative biases in Z_{DR} (Ryzhkov, 2007). There is also a concentration of grid points with Z_{H} above 30 dBZ and positive Z_{DR}. This feature is most likely a signature of raindrops.

Figures 6.6b, 6.6c and 6.6d show joint distributions of simulated Z_{H} and Z_{DR} contributions from rain for all model grid points within the common domain for the RA2M, RAL3.1WB and RAL3.1 configurations respectively. Most model grid points have Z_{H} below 30 dBZ and Z_{DR} that does not exceed 1.0 dB. In the single moment microphysics simulations, RA2M and RAL3.1WB, a large number of grid points have simulated Z_{H} and Z_{DR} following a curve with Z_{DR} that increases with Z_{H}. This line resembles the expected relation between the two radar variables

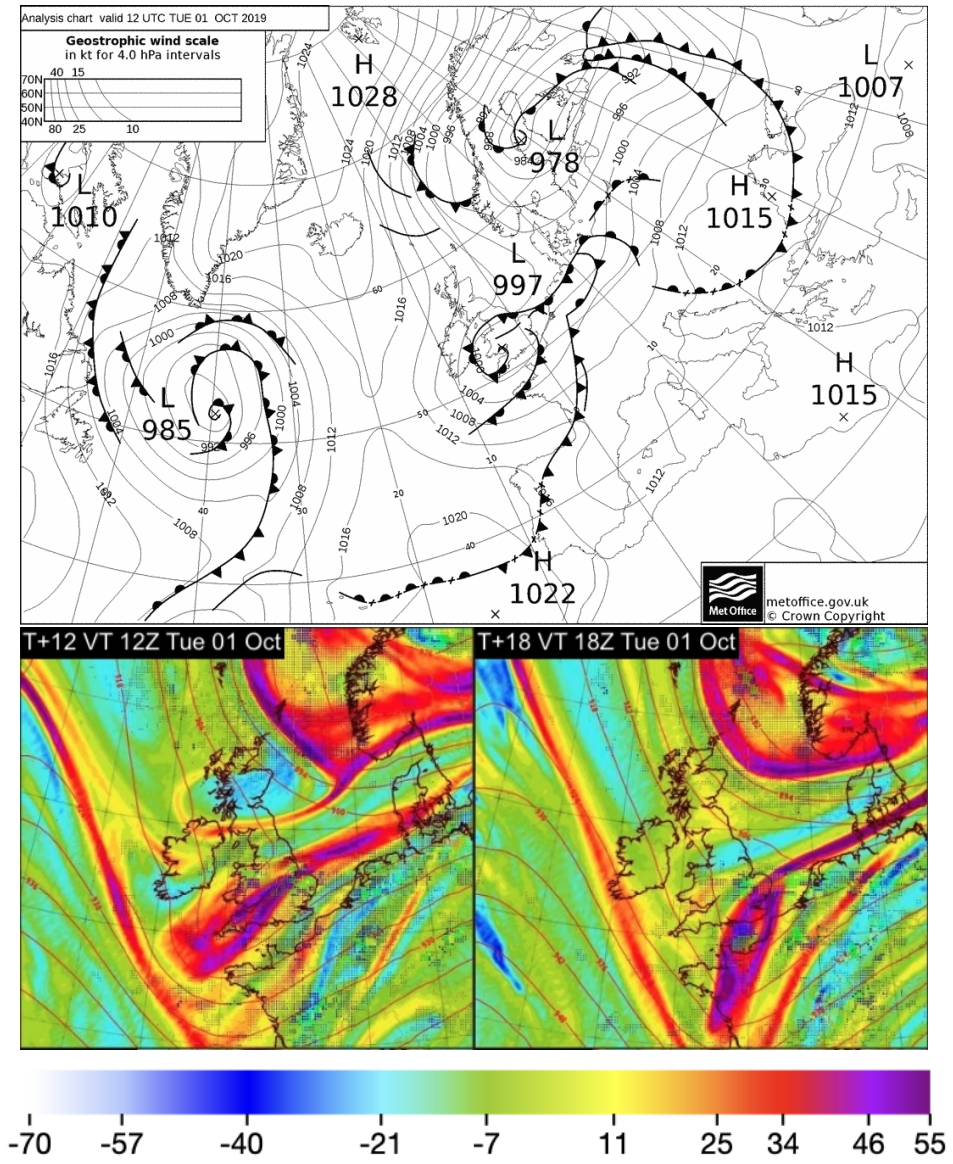

Figure 6.1: Surface analysis chart (top panels) valid on 01 October 2019 at 1200Z. Vorticity fields at 300hPa (bottom panels) adapted from Met Office short range guidance is derived from MetUM global model run initialised at 0000Z and valid at 1200Z (left) and 1800Z (right). Red contours show the geopotential height at 300hPa. The vorticity colour bar tick labels are approximate and scaled by 10^{-5} with units s^{-1}.

considering the one-to-one mapping from q_{rain} to Z_{H}, and from q_{rain} to Z_{DR} for the single moment Wilson-Ballard scheme forward operator described in Chapter 5. A spread of model grid points to the left of the curve is explained by the use of the prognostic precipitation fraction C_{rain} in the calculation of rain mass fraction q_{rain} (Equation (5.7)) and as a multiplier for rain radar reflectivity (Equation (5.10)). Prognostic precipitation fraction is a variable that represents the sub-grid fraction of rain and should have a maximum of value of 1.0. Another reason for deviation from the theoretical curve is the first-order temperature correction for both Z_{H} and

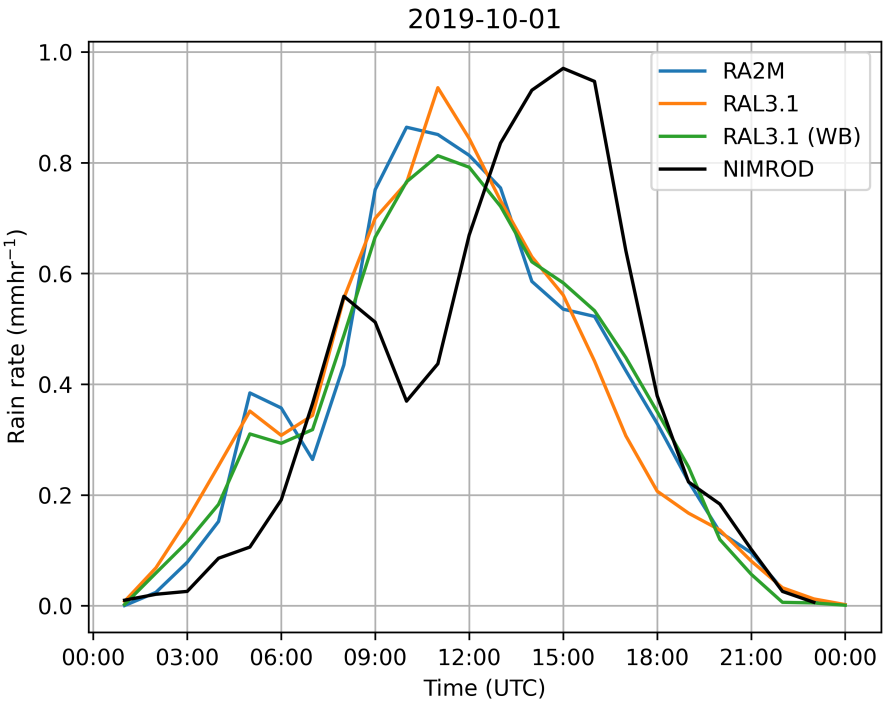

Figure 6.2: Time series of domain-averaged rainfall rate between three model simulations and radar observations (Nimrod).

Z_{DR} and linear interpolation of both values from the lookup table. In the RAL3.1 simulation, most model grid points also follow a positive relation between Z_{H} and Z_{DR} albeit with a more diffuse distribution. Using both rain mass fraction q_{rain} and number concentration of rain n_{rain} severs the one-to-one relation between Z_{H} and Z_{DR}. An evaluation of the simulations is complicated by the construction of the 3D radar composite. I will now proceed with conditional sampling of the data to provide a more detailed evaluation.

A similar set of joint distribution plots are presented in Figure 6.7 but for model and radar composite grid points situated close to 1 km in height respectively. This allows a closer inspection of the joint distribution at levels dominated by liquid rain. At 1 km in height, RA2M and RAL3.1WB grid points are still mostly constrained to the expected Z_{H} and Z_{DR} relationship. The joint distribution of RAL3.1 compares better with the radar composite, despite being underspread. It is worth noting that the spread in the radar composite could be due to uncertainty in observed Z_{H} and Z_{DR}. This result suggests that RAL3.1 seems to represent more realistically observed rain in the warm levels for this case study.

In the radar composite at 3 km in height, where one should expect to find supercooled raindrops within Z_{DR} columns, there is a mode of grid points at Z_{H} of 22 dBZ and Z_{DR} of 0 dB (Figure 6.8), which suggests the presence of small, frozen hydrometeors with a mostly spherical geometry. Although the RA2M and RAL3.1WB plots

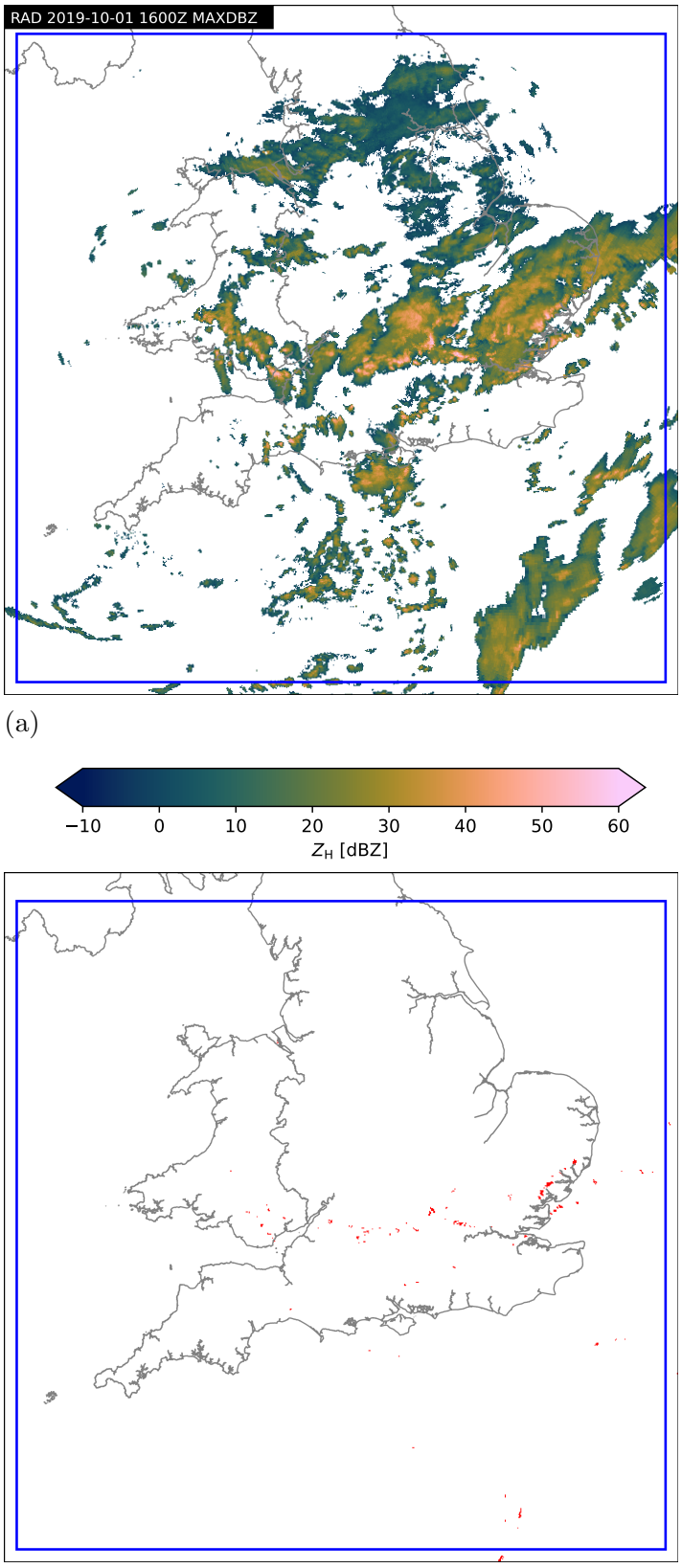

Figure 6.3: (a) Maximum reflectivity field from the three-dimensional radar composite valid on 01 Oct 2019 at 1600Z. The blue rectangle indicates the domain of the 300m resolution MetUM simulations. Z_{DR} column detections are marked as red dots in (b).

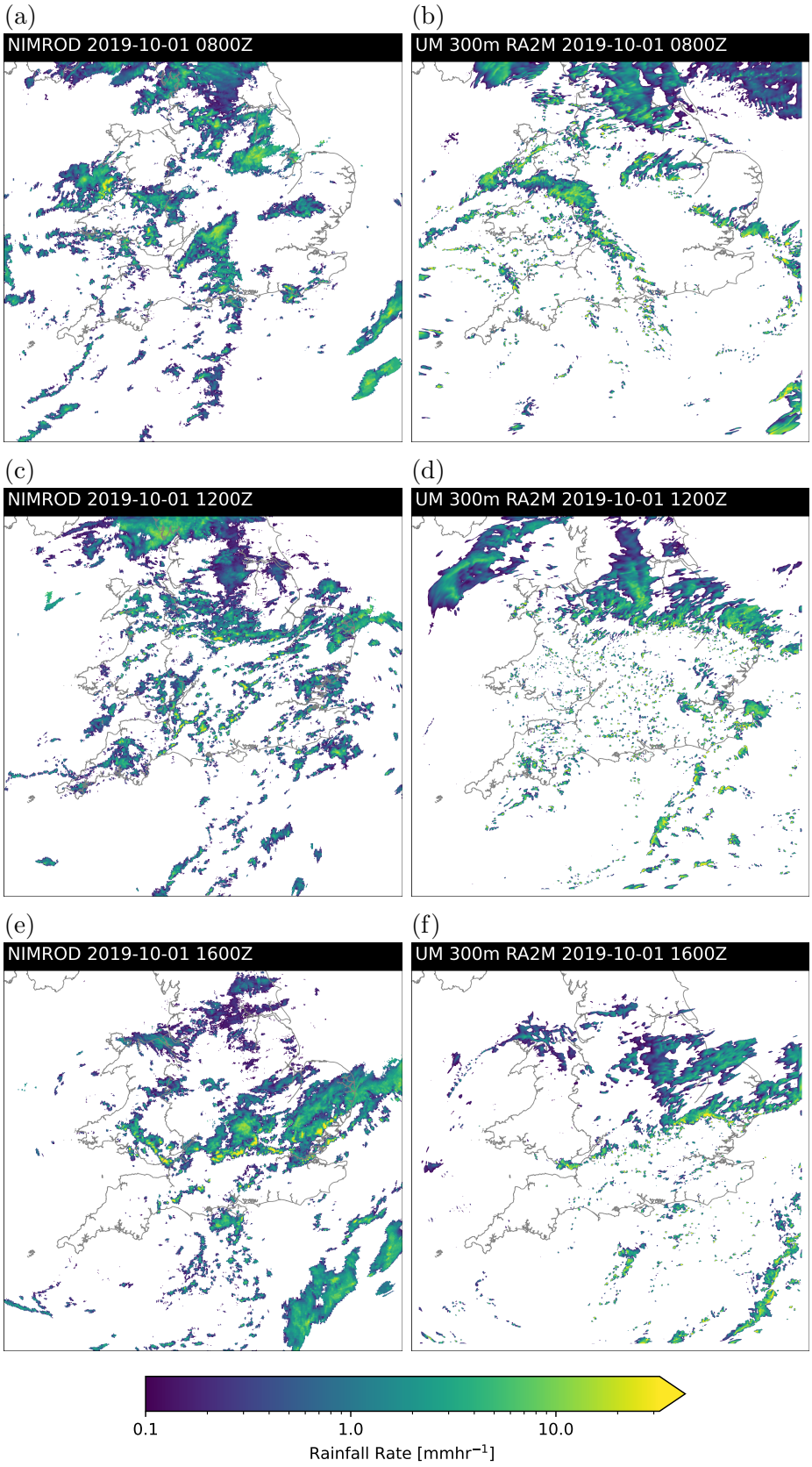

Figure 6.4: Fields of observed rainfall rates derived from the Nimrod system at (a) 0800Z, (c) 1200Z and (e) 1600Z. Simulated rainfall rates from the RA2M model run at (b) 0800Z, (d) 1200Z and (f) 1600Z.

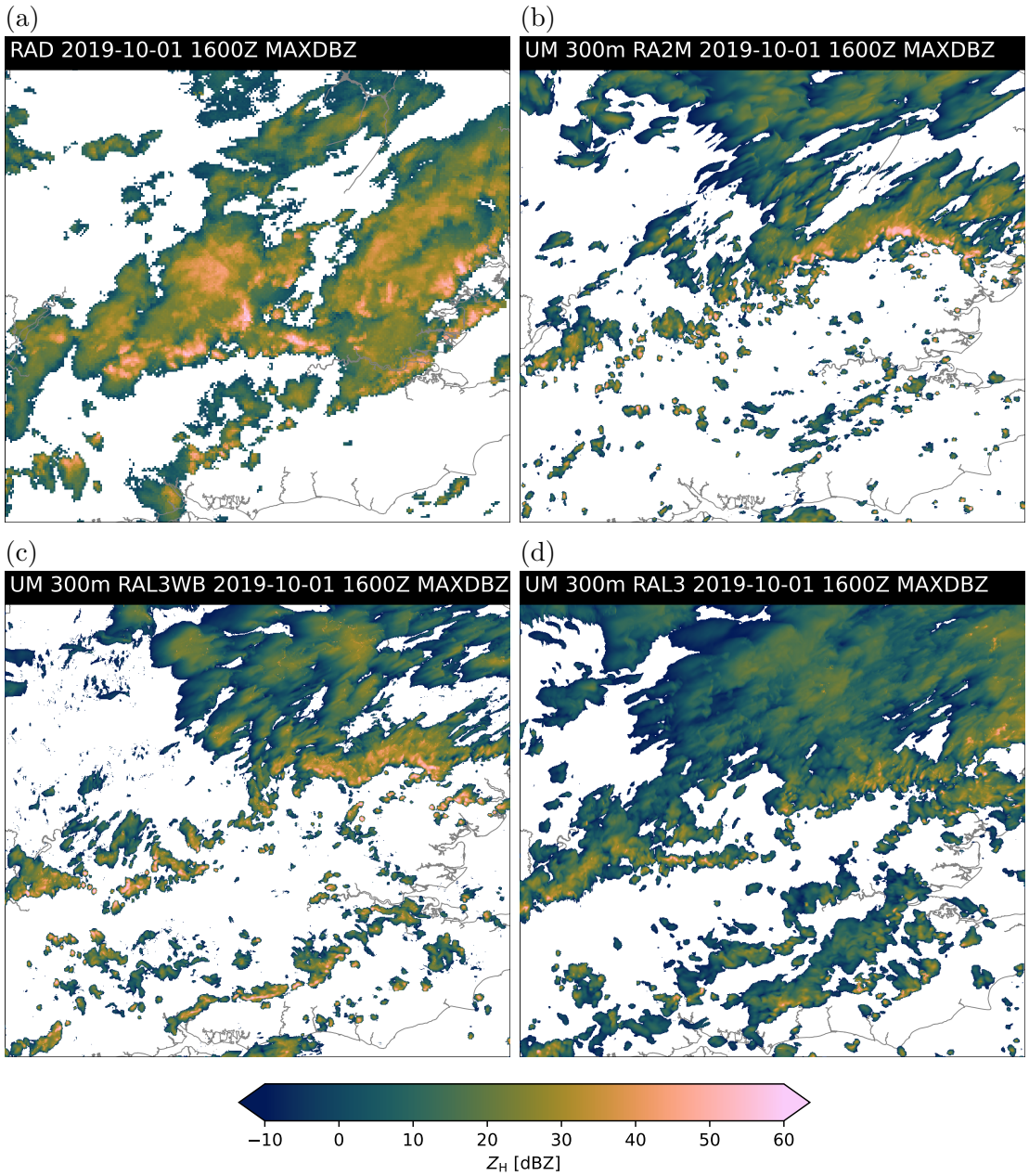

Figure 6.5: Maximum reflectivity field derived from the (a) radar composite, (b) RA2M, (c) RAL3.1 (Wilson-Ballard), and (d) RAL3.1 model simulations covering Southern England valid on 01 Oct 2019 at 1600Z.

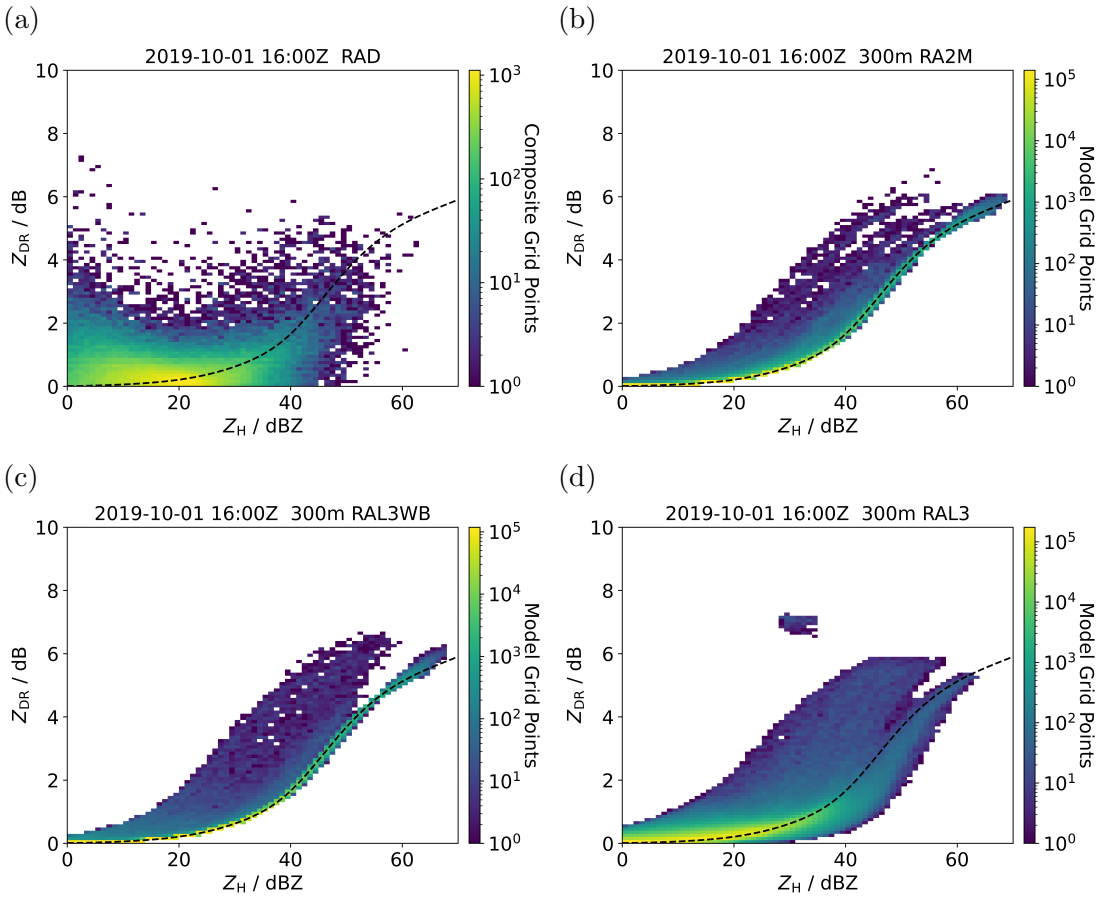

Figure 6.6: Joint distributions of reflectivity Z_{H} and differential reflectivity Z_{DR} values of grid points within the (a) radar composite, (b) RA2M, (c) RAL3.1 (Wilson-Ballard), and (d) RAL3.1 model simulations valid on 01 Oct 2019 at 1600Z. The black dashed line is the one-to-one relation between Z_{H} and Z_{DR} assuming a temperature of 20 °C and an air pressure of 1000 hPa.

still show grid points concentrated on the Z_{H} and Z_{DR} curve, the number of grid points in bins decreases by an order of magnitude compared to their distribution at 1 km. In the RAL3.1 run, there are no grid points at 3 km with simulated Z_{DR} from rain exceeding 2.0 dB and a lack of grid points at reflectivities exceeding 50 dBZ. These results suggest a much lower rain mass just above the freezing level relative to warm levels in both observations and model output. The presence of Z_{DR} exceeding 1.0 dB existing in all joint distributions indicate Z_{DR} columns in both the radar composite and various MetUM simulations.

6.4 Presence of Z_{DR} columns

Figure 6.9b shows a vertical cross section of Z_{DR} from the radar composite. Using 1.0 dB as a nominal threshold for Z_{DR}, the example shows a Z_{DR} column extending to 4 km in height, which is about 1.5 km above the freezing level on that day. The

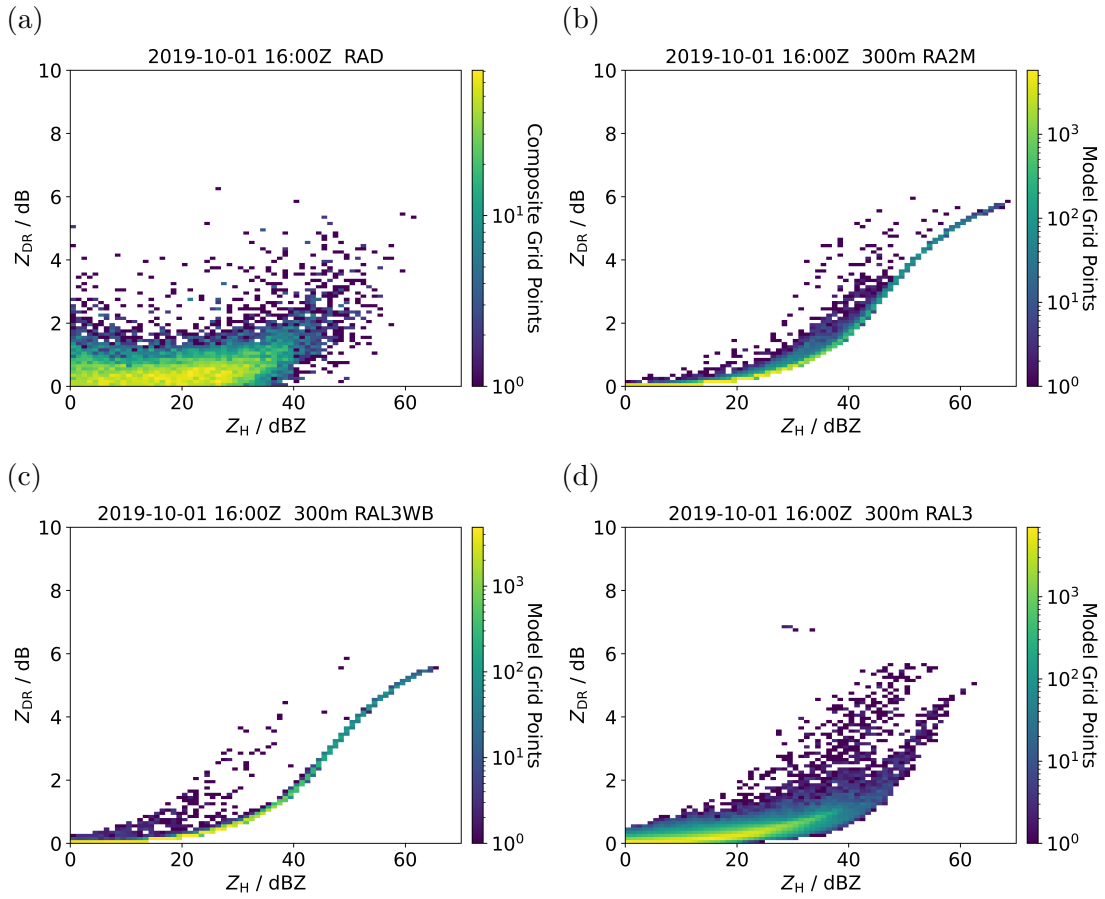

Figure 6.7: Similar to Figure 6.6 but only containing grid points near 1km of height within the (a) radar composite, (b) RA2M, (c) RAL3.1 (Wilson-Ballard), and (d) RAL3.1 model simulations valid on 01 Oct 2019 at 1600Z.

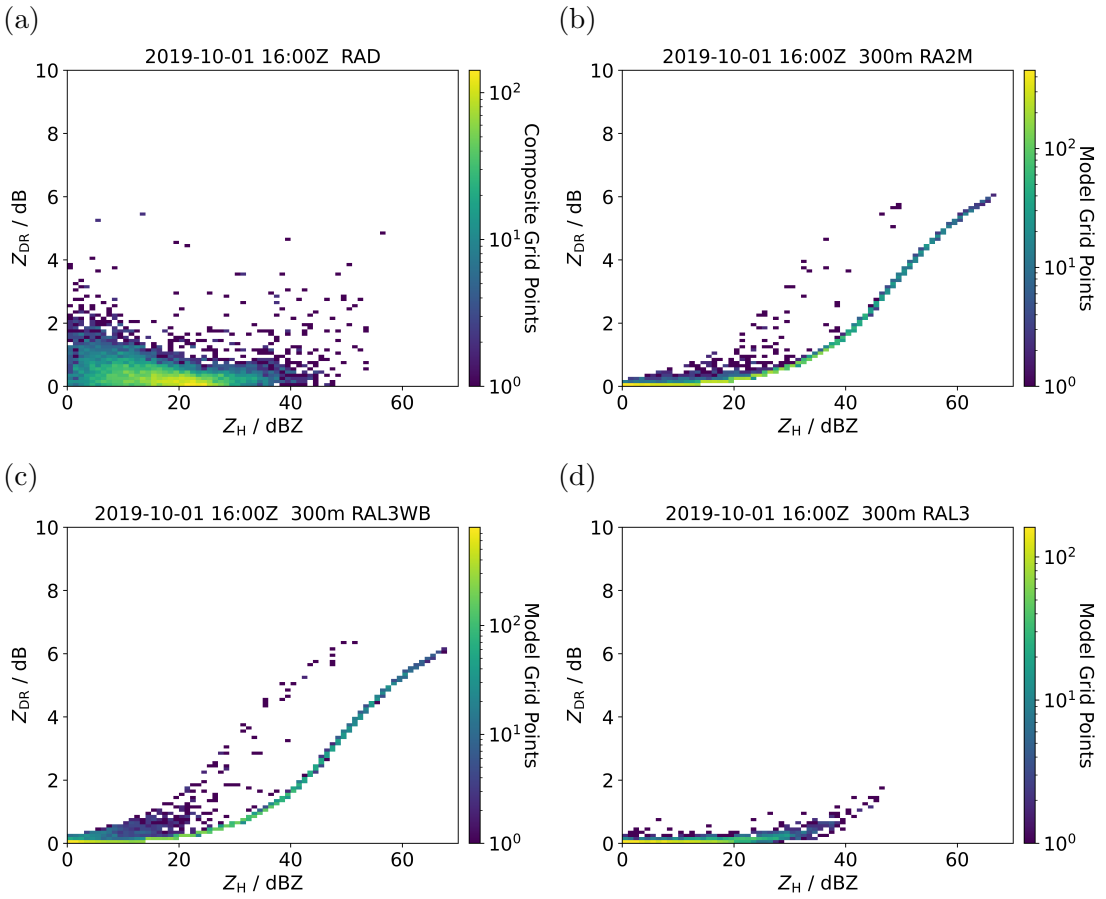

Figure 6.8: Similar to Figure 6.7 but for grid points near 3 km of height within the (a) radar composite, (b) RA2M, (c) RAL3.1 (Wilson-Ballard), and (d) RAL3.1 model simulations valid on 01 Oct 2019 at 1600Z.

observed Z_{DR} column is collocated with moderate Z_{H} of about 20 to 30 dBZ as shown in Figure 6.9. In Figures 6.9d and 6.9f showing vertical cross sections of simulated cells within RA2M and RAL3.1 (Wilson-Ballard) respectively, there are intense Z_{DR} columns exceeding 3.0 dB that extend 2 km above the freezing level. Both Z_{DR} columns are accompanied by high reflectivity values exceeding 50 dBZ as seen in Figures 6.9c and 6.9e. In contrast, RAL3.1 in Figure 6.9h exhibits a shallow Z_{DR} column extending 0.5 km above the freezing level with a maximum Z_{DR} value of 1.0 dB. In these examples within the MetUM, all simulated Z_{DR} columns are well collocated or at the periphery of updraft cores exceeding $5\,\mathrm{m\,s^{-1}}$.

Having inspected one cross section for the radar composite and for each model configuration, we now investigate the vertical extent of enhanced Z_{DR} across the common domain. Figure 6.10 are contour frequency by altitude diagrams (CFAD) (Yuter and Houze, 1995) of observed Z_{DR} from the radar composite and simulated rain contribution to Z_{DR} from model outputs. Taking 1.0 dB as a reference, the RA2M and RAL3.1WB outputs have Z_{DR} features extending up to 3 km above the freezing level, whereas this is limited to 0.5 km in RAL3. There is an abundance of grid points in the radar composite with enhanced Z_{DR} at heights above the freezing level, although this is an observed Z_{DR} value due to scattering by hydrometeors other than raindrops as well. It is clear that there is an abundance of Z_{DR} column signatures from rain in simulations that use single moment microphysics, whereas there is a lack of such features in the simulation with the double moment CASIM scheme.

The differences between RAL3.1WB and RAL3.1 come only from the microphysics scheme, whereas RA2M has differences in other schemes as well. The change in microphysics scheme suggests that it dominates the prevalence of Z_{DR} columns. However, changes in the microphysics scheme can affect dynamics through mechanisms such as latent heat release, cold pools, and hence updraft strengths, which are a main part of Z_{DR} columns. Therefore, it is important to investigate both potential causes of Z_{DR} column differences.

6.5 Updrafts

In order to investigate what updraft speeds could support and loft raindrops that could give an enhanced Z_{DR} value, we consider the relationship between raindrop size, terminal fall velocity and back scatter. Figure 6.11a shows the relationship between the terminal velocity of a water drop and its equivalent spherical diameter based on equations in Beard (1976). An air pressure of 700 hPa and air temperature of $-10\,^{\circ}\mathrm{C}$ are assumed in calculations, so as to obtain values that are appropriate

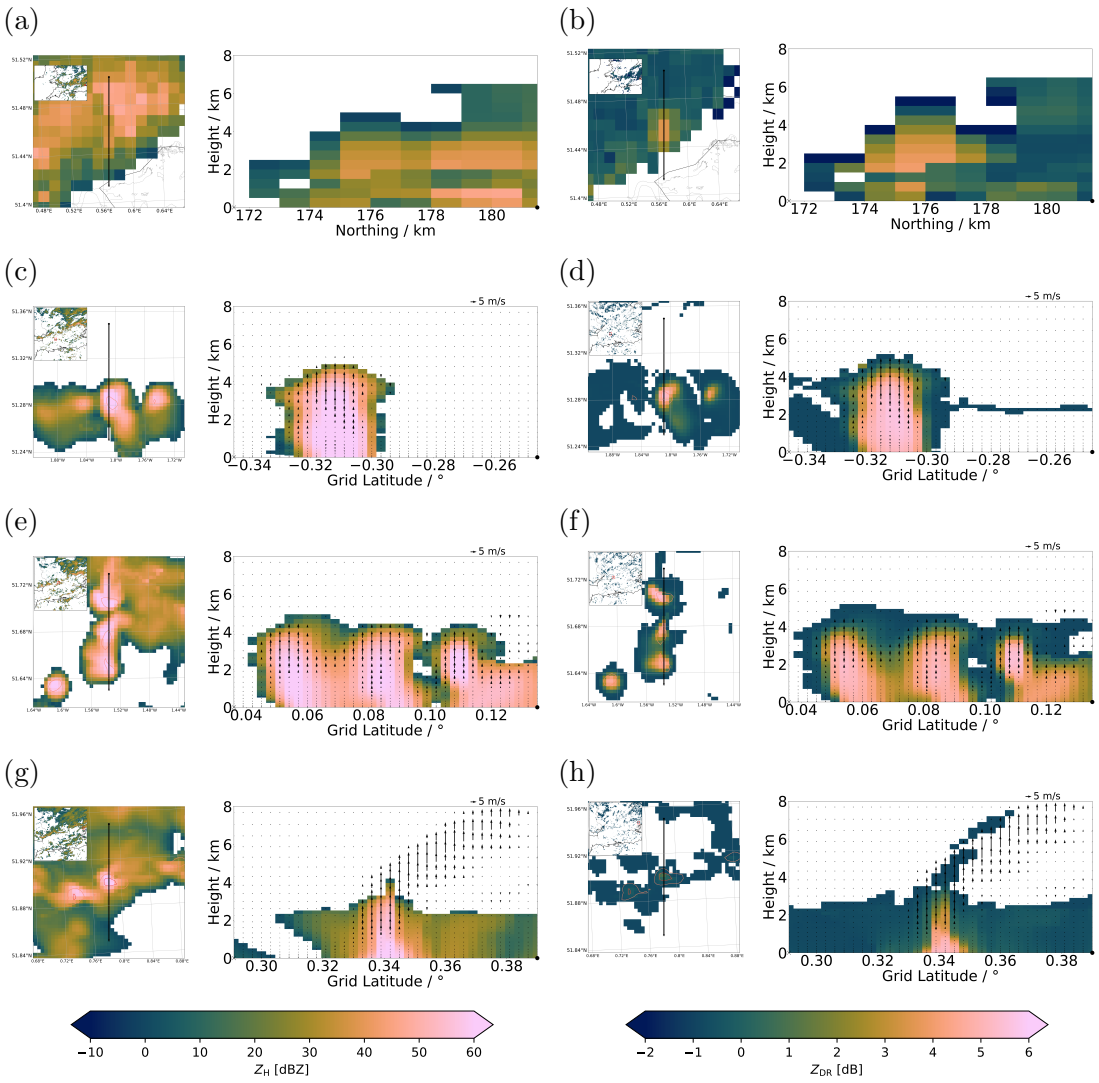

Figure 6.9: Chosen cross sections showing reflectivity Z_{H} and differential reflectivity Z_{DR} for convective cells within the (a, b) radar composite, (c, d) RA2M, (e, f) RAL3.1 (Wilson-Ballard), and (g, h) RAL3.1 model simulations valid on 01 Oct 2019 at 1600Z.

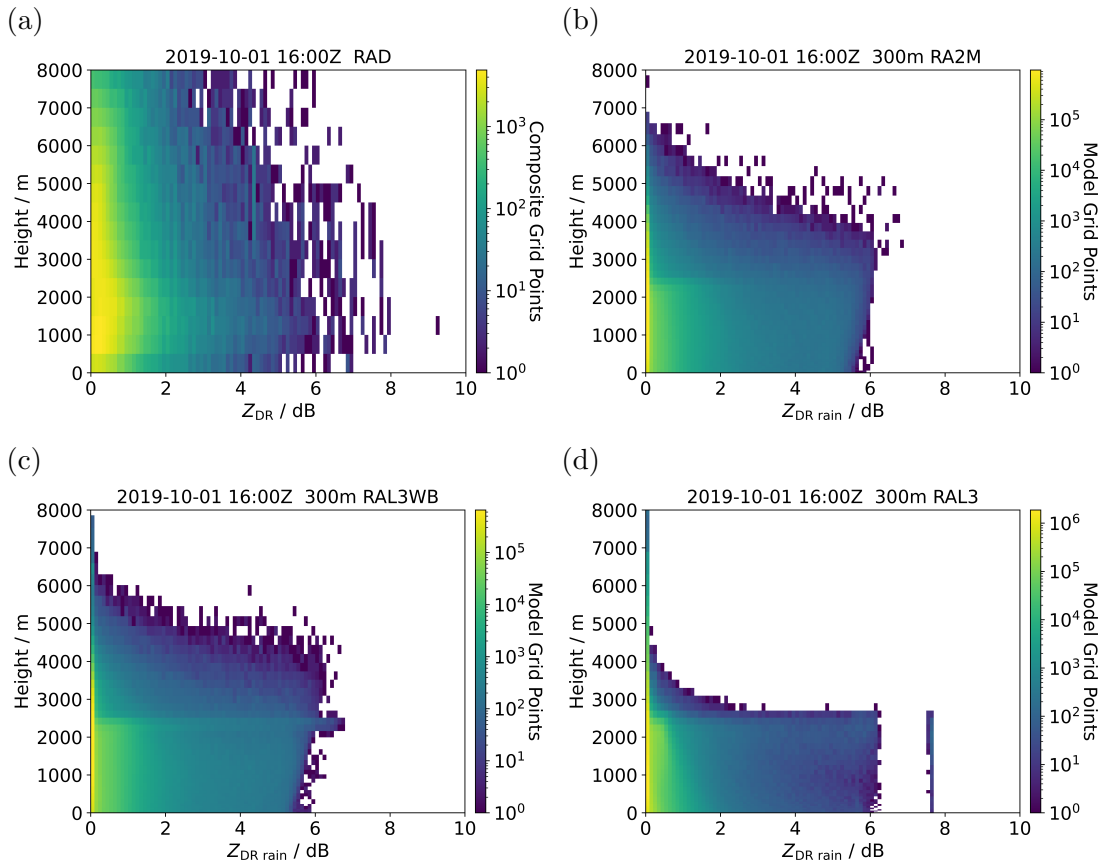

Figure 6.10: Contour altitude by frequency diagrams of differential reflectivity Z_{DR} for grid points within the (a) radar composite, (b) RA2M, (c) RAL3.1 (Wilson-Ballard), and (d) RAL3.1 model simulations valid on 01 Oct 2019 at 1600Z.

for supercooled raindrops approximately situated just above the freezing level. The figure shows a positive relationship between terminal velocity and drop diameter, with terminal velocity levelling off at just above $10\,\mathrm{m\,s^{-1}}$ for multi-millimetre raindrops. Figure 6.11b shows simulated Z_{DR} values for increasing raindrop diameter. The T-matrix method is used here with the Thurai et al. (2007) aspect ratio model. A drop diameter just larger than 2.0 mm would give a Z_{DR} of 1.0 dB. Figure 6.11c links terminal velocity with Z_{DR} highlighting that an updraft exceeding $8\,\mathrm{m\,s^{-1}}$ is necessary to support a raindrop that would give Z_{DR} exceeding 1.0 dB.

Figure 6.12 are distributions of positive upward velocity values present in MetUM simulations outputs. Using $8\,\mathrm{m\,s^{-1}}$ as a reference, RA2M and RAL3.1WB exhibit a similar count of grid point, whereas RAL3.1 has half the number of grid points. Note that RA2M contain grid points with maximum updraft velocities exceeding $20\,\mathrm{m\,s^{-1}}$, but other two simulations only have updraft velocities reaching just above $15\,\mathrm{m\,s^{-1}}$. The cumulative histogram in Figure 6.13 underlines this clearly by showing similar upward air velocity values for both RA2M and RAL3.1 (Wilson-Ballard) up to 99.9-percentile, whereas RAL3.1 (Wilson-Ballard) and RAL3.1 share similar upward air velocities beyond the most extreme 99.9999-percentile.

To better understand the differences in updraft magnitudes, Figure 6.14 compares updraft magnitudes and percentiles between three model runs at model heights up to 8 km. All model runs regardless of configuration exhibit similar updraft values when considering the 99-percentile value at each model level. On the other hand, updraft values at 99.99-percentile diverge between simulations just above 3 km, which is just above the freezing level for this case and where one would expect Z_{DR} column signatures to appear. This set of results suggests that the difference in microphysical scheme could mostly account for differences in moderate updraft values needed to support large drops, whereas differences in updraft values of the highest magnitudes could be attributed to changes in other model physics (RA2M vs RAL3.1). The difference in updraft values between RAL3.1 (Wilson-Ballard) and RAL3.1 (CASIM) can mostly be attributed to differences in the microphysics scheme. It is possible that differences in freezing processes lead to different amounts of latent heat released thus feeding back into updraft magnitudes.

6.6 Microphysics

Other than having sufficiently strong updrafts to loft raindrops to higher heights, another obvious explanation for the difference in prevalence of Z_{DR} columns is the freezing of rain mass into other hydrometeor classes within these updrafts. Figure 6.15a, 6.15b and 6.15c are CFADs of rain mass fraction within vertical columns contain-

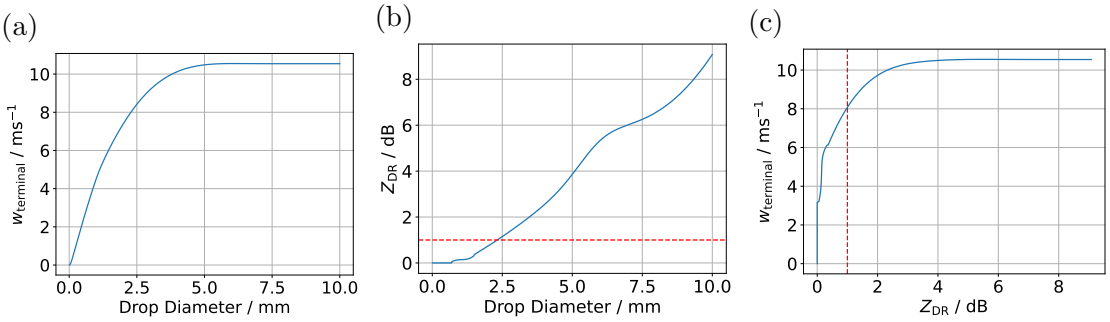

Figure 6.11: Panel (a) shows terminal velocity of raindrops over a range of diameters. Panel (b) shows simulated differential reflectivity Z_{DR} for raindrops of increasing diameters. (c) shows the terminal velocity of raindrops that will result in a certain simulated Z_{DR}. Red dotted lines mark where Z_{DR} has a value of 1.0dB.

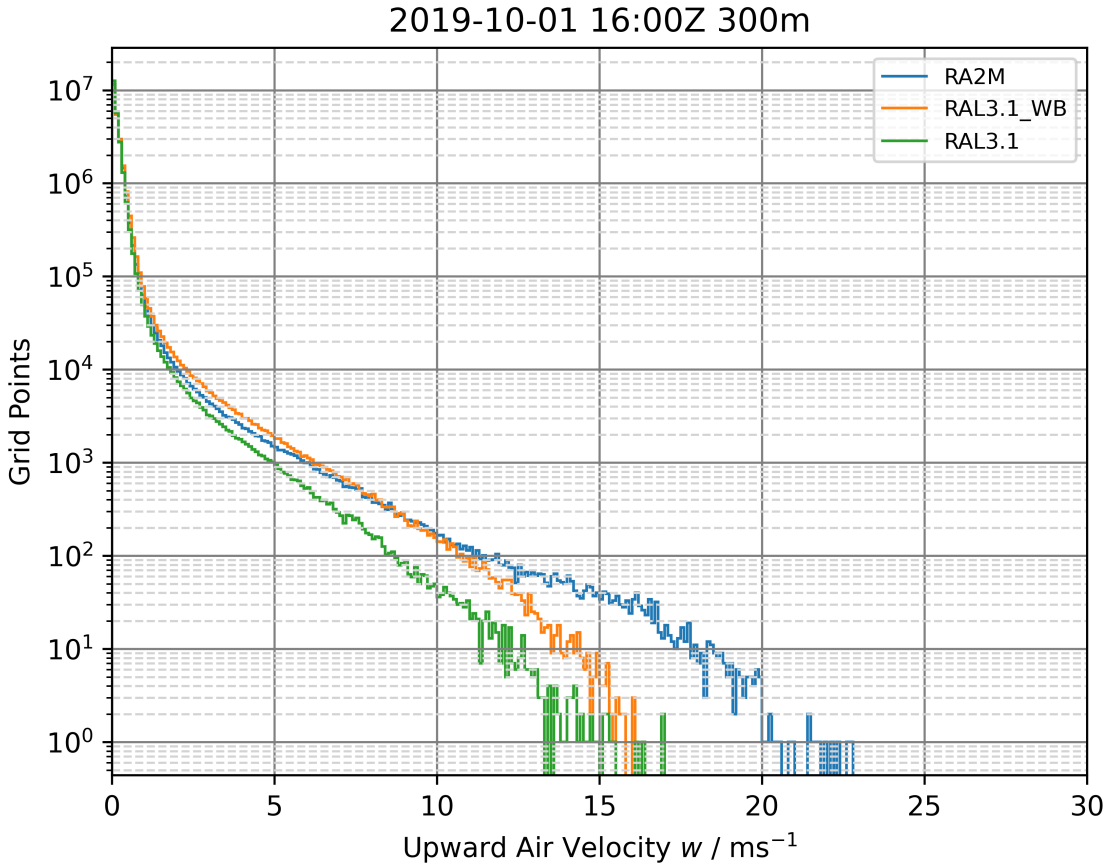

Figure 6.12: Histograms of upward air velocities for grid points above the freezing height within RA2M, RAL3.1 (Wilson-Ballard), and RAL3.1 model simulations valid on 01 Oct 2019 at 1600Z.

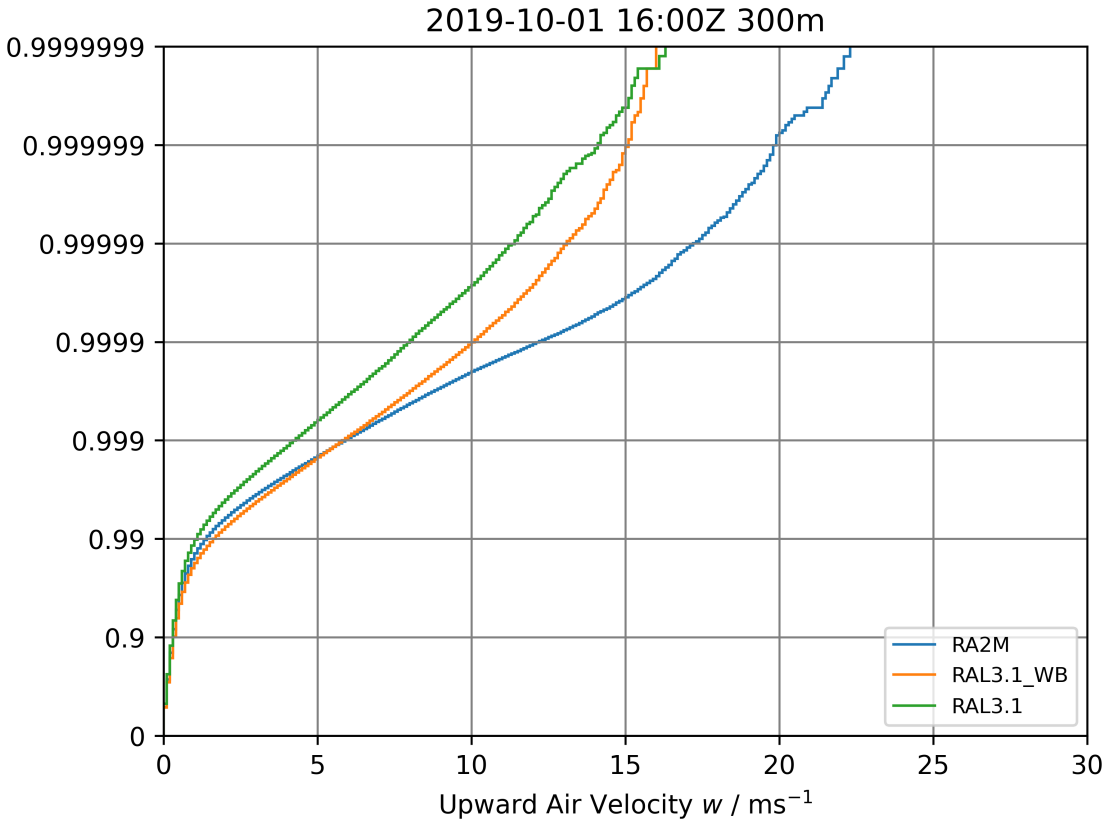

Figure 6.13: Cumulative histograms of upward air velocities for grid points within RA2M, RAL3.1 (Wilson-Ballard), and RAL3.1 model simulations valid on 01 Oct 2019 at 1600Z. The percentiles y on the vertical axis are transformed to $-\log_{10}(1-y)$, so as to highlight the distribution of extreme updraft values.

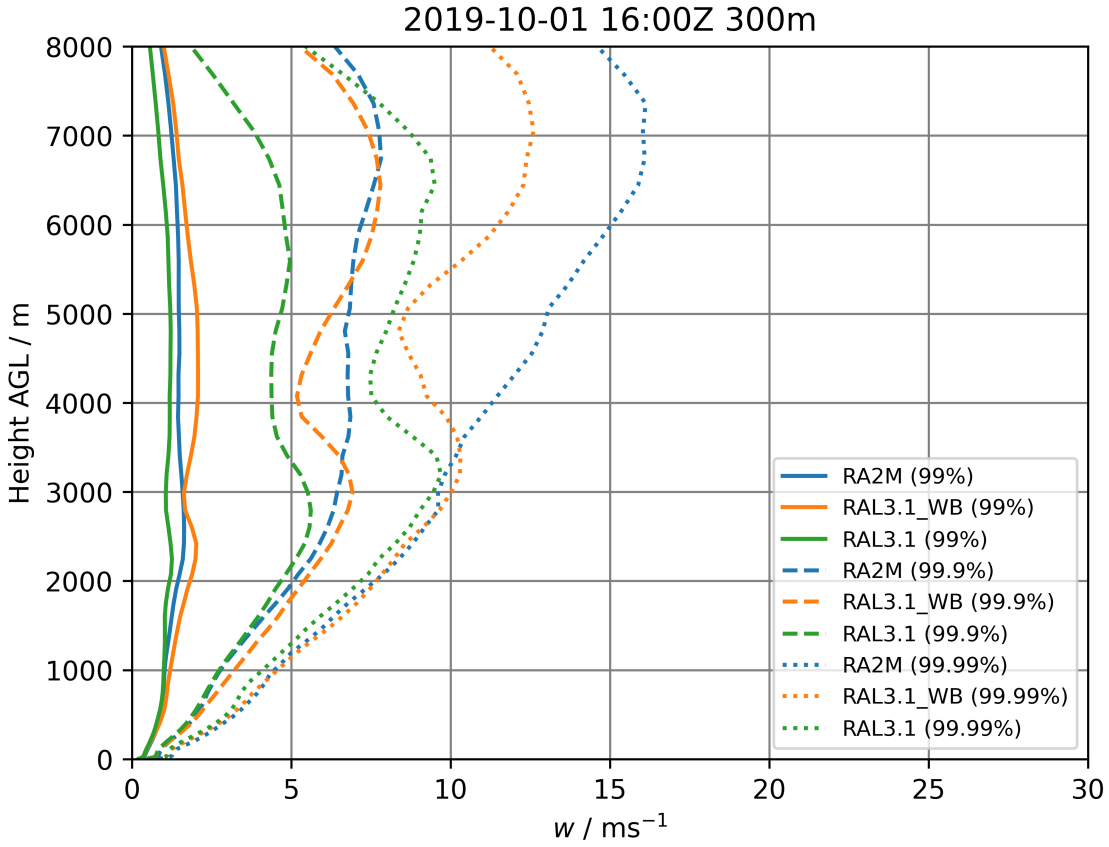

Figure 6.14: Upward air velocity values at 99, 99.9 and 99.99-th percentiles for each model height for RA2M, RAL3.1 (Wilson-Ballard), and RAL3.1 model simulations valid on 01 Oct 2019 at 1600Z.

ing maximum updrafts exceeding $8\,\mathrm{m\,s^{-1}}$ for RA2M, RAL3.1 (Wilson-Ballard) and RAL3.1 respectively. RA2M and RAL3.1WB are similar in that they both contain grid points at 4 km with a rain mass fraction exceeding $1 \times 10^{-3}\,\mathrm{kg\,kg^{-1}}$. Such a value of rain mass fraction is a useful reference comparable to rain mass content within simulated Z_{DR} columns in other modelling studies (e.g. Kumjian et al., 2014). This is in contrast with RAL3.1 CFAD that shows only a few grid points at the same height with a similar rain mass fraction. These rain mass fraction CFADs illustrate the difference in Z_{DR} column presence between using the Wilson-Ballard and CASIM microphysics schemes. A direct comparison cannot be made with radar observations as simulated Z_{DR} in this study is limited to rain.

As mentioned in Chapter 2, one of the biggest differences between rain freezing processes is that Wilson-Ballard does not model the heterogeneous freezing of rain, such that rain is only frozen instantly at $-40\,^{\circ}\mathrm{C}$ or colder, while CASIM introduces immersion freezing based on Bigg (1953) thus allowing for freezing of raindrops into graupel from temperatures lower than $-4\,^{\circ}\mathrm{C}$. Figure 6.15d shows a CFAD for RAL3.1NB. There are no significant changes in the CFAD for large mass fractions of rain compared to RAL3.1, although higher grid point populations are present for small rain mass fraction between 1×10^{-8} and $1 \times 10^{-6}\,\mathrm{kg\,kg^{-1}}$ between 6 and 8 km of height. The latter is expected since less rain mass will freeze into graupel with Bigg freezing inactive at heights where the process should normally become more significant. However, this sensitivity test shows that the Bigg freezing process has little to no effect on the presence of rain mass and their contribution to Z_{DR} just above the freezing level. The difference in rain mass is not compensated for by a difference in graupel mass as seen in the CFADs of Figure 6.16. It seems the signature of the updraft distribution is present here as well, with lower graupel mass reaching further heights in RAL3.1 compared to RAL3.1WB, and greater graupel mass reaching 8 km in RA2M vs RAL3.1WB.

6.7 Summary and conclusions

Simulations have been performed in thge MetUM with 300 m horizontal grid length and with three scientific configurations, namely RA2M running Wilson-Ballard single moment microphysics scheme, RAL3.1 running Wilson-Ballard and RAL3.1 running double moment microphysics scheme CASIM. Although model simulations predicted peak rainfall rates a few hours earlier than the observed peak rainfall rates, all simulations and radar observations showed a prominent line convection feature in the afternoon.

The joint distribution of Z_{DR} and Z_{H} is indicative of the variety of rain rate

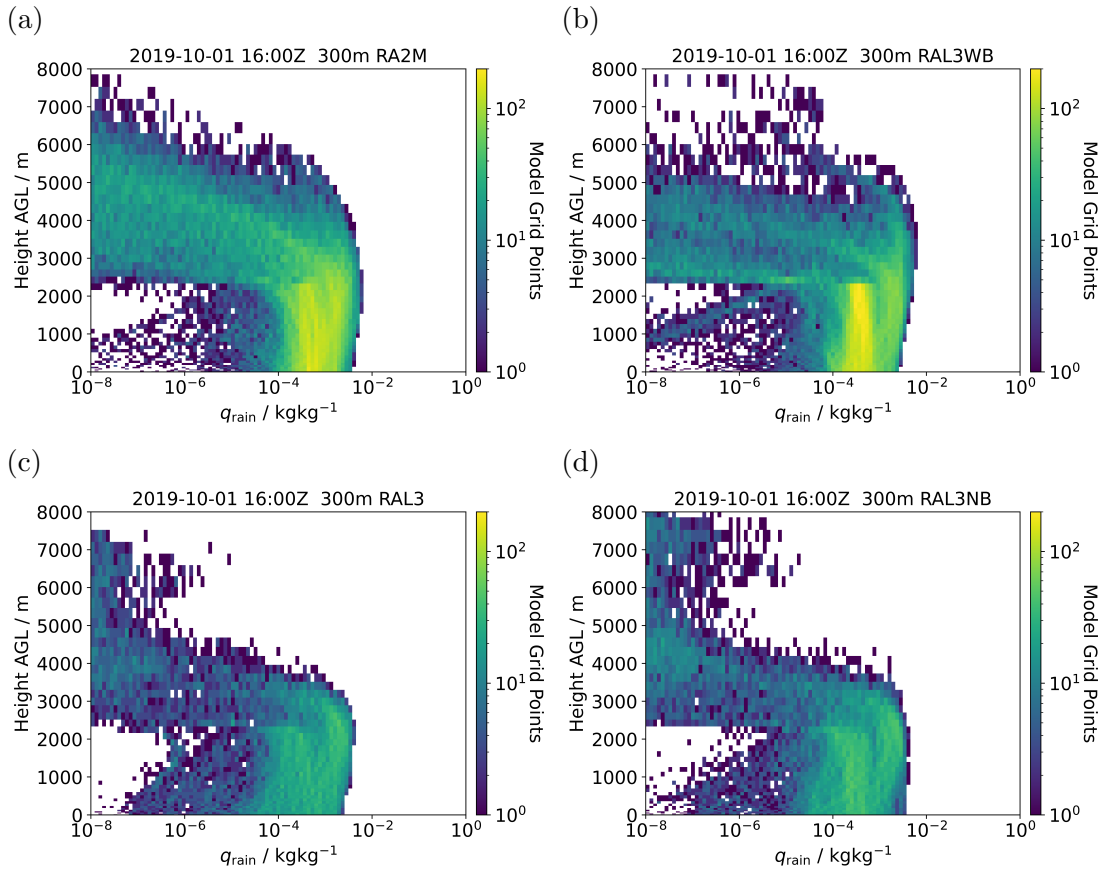

Figure 6.15: Contour altitude by frequency diagrams of rain mass fraction for grid points within columns containing updraft maximum exceeding $8\,\mathrm{m\,s^{-1}}$ for the (a) RA2M, (b) RAL3.1 (Wilson-Ballard), (c) RAL3.1, and (d) RAL3.1 with no Bigg freezing model simulations valid on 01 Oct 2019 at 1600Z.

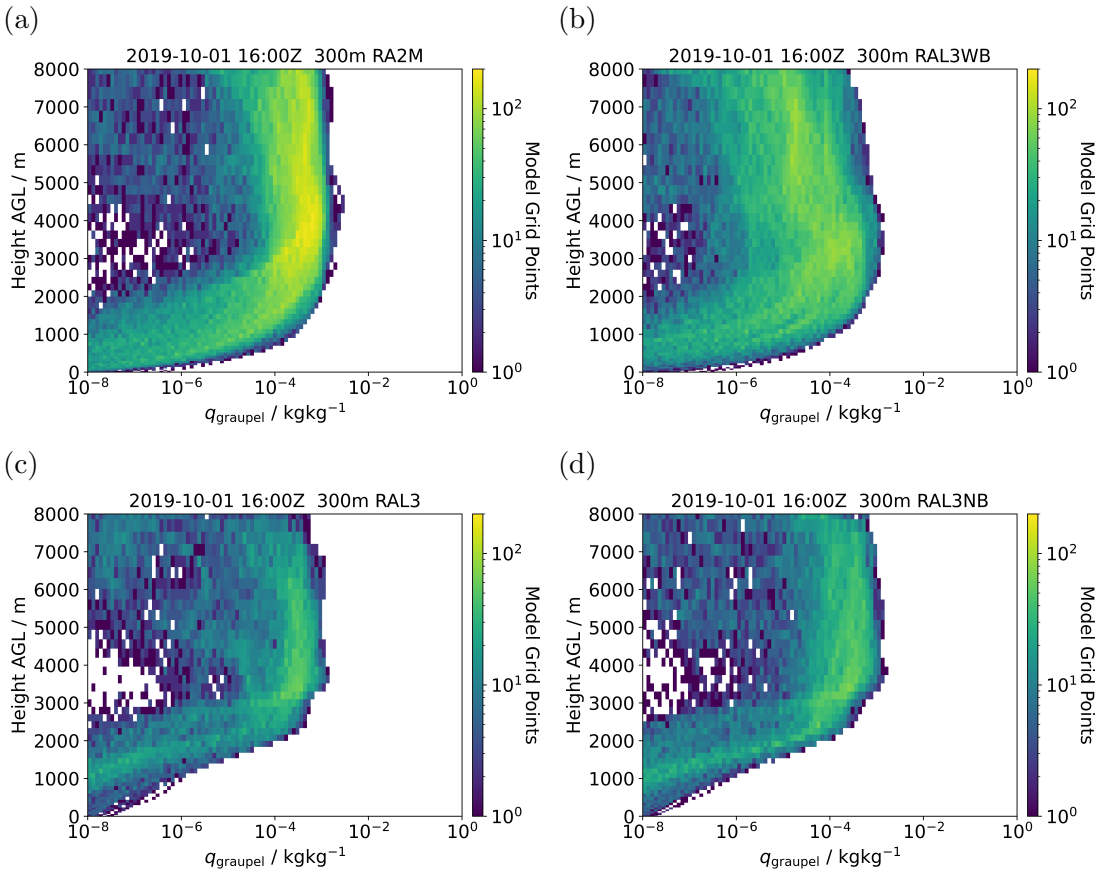

Figure 6.16: Contour altitude by frequency diagrams of graupel mass fraction for grid points within columns containing updraft maximum exceeding 8 m s^{-1} in the vertical for the (a) RA2M, (b) RAL3.1 (Wilson-Ballard), (c) RAL3.1, and (d) RAL3.1 with no Bigg freezing model simulations valid on 01 Oct 2019 at 1600Z.

processes. Unsurprisingly, Wilson-Ballard only considers one prognostic and the distribution follows a one-to-one line. CASIM simulates n and q as separate prognostic variables, allowing a separation between numerous smaller drops and fewer larger drops. This is noted by a greater spread in the Z_{DR} and Z_{H} distribution, which compares better against the observations. Although we are unable to isolate the rain contribution in observations, it is certain there are only raindrops at 1 km in height.

Chosen vertical cross sections of convective cells show wide, deep and intense Z_{DR} columns from rain for simulations using the Wilson-Ballard scheme, whereas CASIM did not produce many Z_{DR} columns from rain. Such results are not limited to the chosen cross sections but are also supported by CFADs of Z_{DR}. Although the Wilson-Ballard CFADs are more similar to the radar composite, it is worth noting that observed Z_{DR} include contributions from frozen hydrometeors as well rather than solely from raindrops. Considering modelled physical processes, differences in rain contribution to Z_{DR} columns between model simulations could be due to contrasting updraft magnitudes and freezing processes that influence the presence of rain mass at heights just above the freezing level.

An investigation into updraft magnitudes revealed differing updraft magnitudes between model runs from the 99.9-th percentile when considering all model grid points with positive upward velocities. The 99.9-th percentile updraft magnitudes for the CASIM simulation and Wilson-Ballard simulations were 4 and 6 $\mathrm{m\,s^{-1}}$ respectively. The most extreme updraft magnitudes reached 22, 16, and 16 $\mathrm{m\,s^{-1}}$ for the RA2M (Wilson-Ballard), RAL3.1 (Wilson-Ballard) and RAL3.1 (CASIM) simulations. This would suggest other model physics playing a role in influencing updraft magnitudes. When stratifying updraft magnitudes by model height, the 99.99-th percentile updraft magnitude at each height deviated between model configurations at or above 3 km in height. Difference in updraft values above the freezing level between microphysical schemes (i.e. RAL3.1WB vs RAL3) suggests thermodynamical feedbacks from different freezing processes in accelerating updrafts aloft. Differences in simulations using the same microphysical scheme but with differences in other model physics (i.e. RAL3.1WB vs RA2M) prompts a closer inspection in how these other physical processes influence updrafts in sub-freezing levels.

Having carried out a sensitivity test by switching off a rain heterogeneous freezing process, it was shown that this process has little direct effect on the sequestration of rain mass just above the freezing level. This preliminary test hints at investigating other microphysical processes such as rain evaporation and graupel accretion which may have a larger control over rain mass near the freezing level. Also, given the likely microphysical feedback on the updraft strength, a further investigation into process rates such as latent heat release would be helpful. Finally, other cases with

widespread presence of strong updrafts would be a useful comparison to see whether RAL3.1 coupled to CASIM can produce Z_{DR} columns at all.

Chapter 7

Summary and future work

7.1 Overview

The contribution of updrafts to severe convective storms are profound and well-researched, but the potential of using Z_{DR} columns as a proxy for such updrafts for operationally predicting severe convection remains poorly understood. A dual-polarisation radar transmits and receives radio waves polarised in both the horizontal and vertical directions, which allows for Z_{DR} to be measured, thus giving information on the phase and oblateness of hydrometeors observed. The UK C-band radars have recently been upgraded to have dual-polarisation capability, enabling the potential use of Z_{DR} for nowcasting severe convection. However, prior to this thesis, Z_{DR} was not included in the Met Office 3D radar composite, and the prevalence of Z_{DR} columns in the UK was yet to be explored.

At hourly to weekly timescales beyond nowcasting, NWP models provide situational awareness to assist in forecasting convective events. The Met Office have developed a double moment microphysical scheme, which simulates hydrometeor number concentration and mass fraction as separate prognostics, allowing a greater range of Z_{H} and Z_{DR} combinations to be represented. At hectometric-scale grid lengths, updrafts can be simulated at the appropriate size and strength to theoretically produce Z_{DR} columns, which would be of further benefit especially when forecasting severe convection. However, prior to this thesis, the radar forward operator available did not simulate non-Rayleigh scattering or polarisation, which are essential for correctly estimating radar variables for the large raindrops that constitute Z_{DR} columns.

To address these points:

1. The radar composite was extended to include Z_{DR} data. Pseudo-RHIs were generated using the compositing process and verified against CAMRa RHI scans in Chapter 3.
2. An automatic Z_{DR} detection algorithm was designed and implemented for

use with outputs from the 3D radar composite. The use of the algorithm for investigating the potential use of Z_{DR} columns in nowcasting severe convection is presented in Chapter 4.

3. A forward operator was developed including non-Rayleigh scattering for simulating Z_{H} and Z_{DR} from C-band radars. The testing and implementation online within the MetUM is described in Chapter 5.

4. Simulated radar variables from various MetUM simulations were compared with radar composite observations in Chapter 6. Other model fields and sensitivity tests were carried out to investigate the reasons behind the presence or lack of simulated Z_{DR} columns.

In the following sections, the results, limitations and potential directions for future work completed within these four work chapters are summarised.

7.2 How reliably are Z_{DR} signatures represented within the 3D radar composite?

7.2.1 Summary

In Section 2.3, the specifications of CAMRa and the scanning strategy used in data collection were discussed to demonstrate the suitability of CAMRa for verifying interpolated radar observations in the 3D radar composite. Specifically, the width of the beam is sufficiently narrow to sample Z_{DR} columns from carrying out RHI scans.

In Chapter 3, a visual comparison between CAMRa RHIs and pseudo-RHIs generated from the radar composite highlighted that an azimuthal correction was needed for the latter. Following this correction, pseudo-RHIs were generated for each corresponding CAMRa RHI scan by interpolating C-band radar data along the CAMRa scan azimuth. Z_{DR} columns shown to be present in the pseudo-RHIs were also in the CAMRa scans, albeit with less intense columns extending to lower heights in CAMRa due to different scanning resolutions between CAMRa and composite.

Joint distributions of Z_{H} and Z_{DR} were found to be similar between CAMRa and composite for grid points lower than the freezing height. The spread of Z_{DR} values is greater in the composite for points higher than the freezing height.

A 3D radar composite can reliably represent Z_{DR} signatures such as enhanced values in Z_{DR} columns.

7.2.2 Limitations and future work

Radar calibration

Despite the implementation of an azimuthal correction fixing dislocations in Z_{H} data, finer Z_{DR} signatures still show some evidence of dislocations. This should prompt further investigations into how the Met Office carries out radar azimuth calibrations, which should then inform appropriate corrections to be made before each radar sampling location is fed into the compositing process.

When the 3D radar composite with data from all UK C-band radars become operational, an evaluation against research radar scans will also be beneficial. This will allow any artefacts arising from other radars to be identified. A wider range of case studies occuring at other locations can also be evaluated, rather than being limited to the coverage of a radar composite generated using only two operational radars.

RHI scan strategy

A Z_{DR} column is a 3D phenomenon, whereas a radar RHI scan is a 2D measurement that does not necessarily capture the centre of a Z_{DR} column. The scans analysed in Chapter 3 are available where RHIs have covered a small range of azimuths, which captures the 3D extent of convective cores. Future work could prepare a composite from multiple CAMRa RHIs to better capture the 3D nature of Z_{DR} columns and allow a fairer comparison with the operational radar composite.

Mie resonance

Further research is required to investiage the Mie resonance effects on Z_{DR} measurements made by the C-band operational radars relative to CAMRa that operates in the S-band. Ryzhkov et al. (2005) illustrated dependencies of Z_{DR} on equivolume diameter of individual raindrops at S, C and X-bands. They showed that resonance effects at C-band could give anomalously high Z_{DR} and pointed out using disdrometer data that the difference in Z_{DR} between S-band and C-band becomes significant when $Z_{\mathrm{DR}}(\text{S-band}) > 2\,\mathrm{dB}$. The median Z_{DR} values in Section 3.3 also show this difference. Hence, the effect of Mie resonance will have to be accounted for if enhanced Z_{DR} values are to be compared between the composite and CAMRa in future works. More scans capturing severe convection where one would likely find high Z_{DR} values would also help.

Met Office composite scan strategy

Scan strategies involving higher elevations could be considered to provide coverage with finer sampling resolution at higher altitudes. This would allow the composite to better capture Z_{DR} columns and provide more reliable information on the height of Z_{DR} columns. In future studies, the height of enhanced Z_{DR} values within the composite could then be compared with CAMRa, rather than just checking for presence of columns.

7.3 How effectively could Z_{DR} columns be used for the early detection of severe convection within the United Kingdom?

7.3.1 Summary

A Z_{DR} column detection algorithm was implemented with primary thresholds in Z_{H} and Z_{DR} that have to be fulfilled by the entire identified object, and secondary thresholds also in both radar observables that have to be exceeded by maxima in the object. By tracking identified cells, the study found a lead time of up to 20 min between an increase in the number of detected column pixels and the tracked cell meeting the criterion for severe convection. Testing a range of thresholds with the use of verification metrics yielded preferred secondary thresholds of 1.4 dB of Z_{DR} and a similar secondary threshold at 30 dBZ of Z_{H}. However, the lead times and the set of secondary thresholds that offer the best algorithm performance vary amongst cases.

7.3.2 Limitations and future work

Scan strategy

The nowcasting study highlights several issues with using Z_{DR} columns to nowcast severe convection. Although the highest PODs in this study are comparable with other studies, a high amount of false alarms could explain for the lower CSIs. Extra criteria pertaining to the height of detected columns could reduce FAR, as higher columns are known to be associated with stronger updrafts. However, the low elevation scan strategy currently adopted by the Met Office does not allow higher parts of Z_{DR} columns to be well resolved. As such, scan strategies involving higher elevations would provide better coverage at higher altitudes. This would permit a more reliable measurement of column heights, which could potentially be exploited

as an additional identification criterion.

Composite by synoptic regime

A variety of optimal thresholds and lead times were found across the cases studied in Chapter 4. The 3D composite can now be obtained with Z_{DR} for any day since 2018 (Chapter 3), so future work could consider whether lead time and optimal thresholds are less variable when considered for a specific synoptic regime (e.g. using regimes classified by Wilkinson and Neal (2021)). A nowcasting algorithm could then be designed with adaptable thresholds and lead-time expectations for warnings. Considering data latency, operational forecasters may have up to 15 minutes of notice between Z_{DR} column detection and the convective cell meeting the radar-based definition of severe convection. This could be used simultaneously with and tested against other radar product outputs such as areas of intense radar reflectivity.

Alternative techniques

Reliance on fixed thresholds could mean that the detection algorithm is not robust against Z_{DR} bias. Krause and Klaus (2024) developed a novel Z_{DR} column detection method that uses the hotspot technique to identify the base of a column at $-10\,^{\circ}\mathrm{C}$. Such a technique computes the difference between the median of the data in a central region and the median of the data in a larger area surrounding the central region. The value of the Z_{DR} hotspot is the central area median minus the background area median. The study claims that the method produces improved performance for areas where differential attenuation is present and allows forecasters to quickly focus on multiple intense updraft areas within a well-organised storm. The application of this technique in the UK 3D radar composite could make detection of Z_{DR} columns more robust across the spatial domain of the radar composite and different case days, thus improving nowcasting metrics of severe convection.

7.4 How could Z_{DR} be simulated within the Met Office Unified Model?

7.4.1 Summary

In Chapter 5, a polarimetric radar forward operator was built to simulate Z_{H} and Z_{DR} of prognostic rain from the MetUM in the C-band using the T-matrix method that accounts for Mie resonance effects. Comparisons between simulated Z_{H} from the MetUM assuming Rayleigh scattering and simulated Z_{H} from the polarimetric radar forward operator showed consistently similar Z_{H} values below 40 dBZ as expected

as this is the regime where Rayleigh scattering dominates. For $Z_{\mathrm{H}} > 40\,\mathrm{dBZ}$, the new operator deviated by $\pm 3.5\,\mathrm{dBZ}$, demonstrating the importance of considering Mie resonance effects particularly for severe convection.

Several raindrop shape parameters are unmodelled in the MetUM but important for the polarimetric radar operator. The choice of aspect ratio model was not sensitive for simulated Z_{DR} values exceeding 1.0 dB. Increasing the canting distribution width from 0 to 20° reduces simulated Z_{DR} by around 2.0 dB. From these sensitivity tests, the Thurai et al. (2007) aspect ratio model was selected with all raindrops having a zero canting angle.

The forward operator was implemented online within the MetUM in the form of lookup tables. A first-order temperature correction was included owing to the changes in hydrometeor dielectric constant with temperature, which will also affect simulated Z_{DR}.

7.4.2 Limitations and future work

Radar viewing angle

The implemented forward operator assumes the radar beam to be horizontally incident on hydrometeors. Such an assumption, although appropriate for low elevation scan strategies performed in the UK, would cause an overestimate for simulated Z_{DR}. In other words, the Z_{DR} signal from an oblate raindrop viewed from the side is the largest, in contrast to the nearly circular projection when a raindrop is viewed directly from below. If the UK Met Office adopts a scan strategy with higher elevation angles as proposed in Sections 7.2.2 and 7.3.2, the effect of a non-horizontal beam will have to be accounted for Z_{DR} values to be accurately simulated. This can be achieved by simulating radar observables assuming specific locations in the MetUM. Alternatively, observed Z_{DR} from single-site radar observations could be corrected as if hydrometeors were observed from a horizontal perspective before being composited.

The implemented forward operator also assumes zero canting angle for all raindrops. Thus, the effect of canting angle could also be explored by carrying out sensitivity tests with a non-zero canting angle distribution width.

Attenuation

Strong attenuation can result in differential attenuation, whereby Z_{H} is attenuated more significantly than Z_{V}, such that observed Z_{DR} is underestimated or negative at the far side of a region of intense rainfall (Smyth and Illingworth, 1998). The current forward operator does not simulate attenuation, which would suggest an

overestimation of simulated Z_{DR} as well as Z_{H}. Future studies could consider including the effects of attenuation in the forward operator (Hogan, 2007) or correct for attenuation in single-site radar observations before interpolating the corrected observations into a composite.

Alternatively, the attenuation of Z_{H} and Z_{DR} could be estimated based on observed radar profiles. The estimates could then be used to weight each radar scan for constructing the 3D radar composite.

Other hydrometeor species

The currently implemented polarimetric radar operator only considers contributions from raindrops for the simulation of Z_{H} and Z_{DR}, which is appropriate for this study considering that the base and core of Z_{DR} columns consist mostly of supercooled raindrops. However, to properly simulate radar observations for the top of Z_{DR} columns and other parts of a convective storm dominated by frozen hydrometeors, any future work building on this study should include other hydrometeor classes modelled in the MetUM and their contributions to simulated polarimetric measurements. The graupel class, which is expected to be prevalent at the tops of Z_{DR} columns, could influence the value of simulated Z_{DR}.

7.5 How is Z_{DR} represented within the Met Office Unified Model coupled to different microphysics schemes?

7.5.1 Summary

For a case study with observed Z_{DR} columns along a convergence line, the MetUM was run at 300 m horizontal grid length in three configurations.

Similarly-sized convective cells containing a Z_{DR} column and along the convective line were identified in observations and model simulations. For the simulation running the single moment microphysics scheme, the vertical cross sections show wide, deep and intense Z_{DR} columns from rain, whereas in the simulation coupled to CASIM, simulated columns are rare. When comparing the vertical distribution of Z_{DR} values using CFADs, Wilson-Ballard simulations were more similar to the radar composite, in terms of intensity and height of enhanced Z_{DR} values. The CASIM simulation had low occurrence of $Z_{\mathrm{DR}} > 1.0\,\mathrm{dB}$ above the freezing height, in line with the visual inspection of cross-sections.

Updraft magnitudes differed between model runs from the 99.9-th percentile,

with the CASIM simulation and Wilson-Ballard simulations modelling 4 and 6 $\mathrm{m\,s^{-1}}$ respectively when considering all model grid points with positive upward velocities. The most extreme updraft magnitudes reached 22 and 16 $\mathrm{m\,s^{-1}}$ for the Wilson-Ballard and CASIM simulations respectively. The 99.99-th percentile updraft magnitude at each model level deviated between model configurations at or above 3 km in height. Difference in updraft values above the freezing level between microphysical schemes, keeping all other parameter choices identical, suggests thermodynamical feedbacks from different freezing processes in accelerating updrafts aloft.

A sensitivity test was done by switching off a heterogeneous freezing process (Bigg, 1953) in CASIM, considering this process is absent from Wilson-Ballard scheme. However, switching this process off had little influence on the presence of Z_{DR} columns within CASIM.

7.5.2 Limitations and future work

This contrast in Z_{DR} column presence between Wilson-Ballard and CASIM within the MetUM simulations remains an open question.

Rain sources and sinks

Regarding the microphysics schemes, other differences in rain source and sink processes between Wilson-Ballard and CASIM could be tested to see if it affects the modelled Z_{DR} columns. For instance, accretion of rain by frozen hydrometeors is a process present in both schemes, but is formulated differently giving different process rates. The effect of having different number of moments in each scheme has yet to be tested. This would require setting up a CASIM simulation omitting number concentration of hydrometeor species as a prognosed variable.

Studies such as Cotton (1972) illustrate how different rates of activation and freezing into the ice phase affect updraft speeds aloft via latent heat release. More model diagnostics would also be requested in the model output including microphysical process rates and latent heat release rates. This would allow an investigation on the contribution of latent heat released by from microphysical processes such as freezing of supercooled rain drops and by accretion of rain by frozen hydrometeors to cloud buoyancy.

The piggybacking approach described in Grabowski (2019) attempts to discriminate the effect of changing model physics having a physical impact from the simulation merely having a different flow realization. The method uses two sets of thermodynamic variables in a single cloud simulation. The two sets differ in a specific element of the model physics to be tested, such as the microphysics parametrisation. One set of thermodynamic variables is coupled to the dynamics and drives

the simulated flow, whereas the other set of thermodynamic variables are carried by the flow but do not affect it, otherwise known as the piggybacking set. In another simulation, the two sets are switched (i.e. the set driving the simulation becomes the piggybacking one, and vice versa). Analysing the differences in driver minus piggybacker between both simulations allows the impact of the physics on the flow dynamics to be investigated.

Higher resolution

The effective resolution of an NWP model is typically a few times greater than its grid length (Skamarock, 2004). Modelled Z_{DR} columns in previous studies have a width of up to 500 m. The 300 m grid length used in this study was a compromise between being able to simulate Z_{DR} column signatures and the computational resources available. Future simulations should be run at a resolution of 100 m to more accurately simulate updrafts and Z_{DR} columns in the MetUM.

The coarse temporal resolution of hourly ouputs from this work is a significant limiation, considering the lead time of Z_{DR} columns is on the order of 20 minutes. A study on the evolution of Z_{DR} columns within tracked convective cells would require outputs at a much finer temporal resolution (e.g. 5 minutes) that is comparable with that of the 3D radar composite.

7.6 Concluding remarks

This thesis has demonstrated the various uses of Z_{DR} in understanding severe convection. It has introduced a number of methods in which Z_{DR} observed from the UK radars can already be applied to nowcasting and model evaluation to good effect.

Some of these findings are relevant for other modelling and radar communities, especially as we find some conflicting messages about Z_{DR} column thresholds important for flexible nowcasting and perhaps surprising issues with multi-moment microphysics. Several angles for follow-up research were introduced, with advice to modellers and radar operations.

The potential impact of Z_{DR} on the skill and timing of forecasting severe convection makes this an area worthy of further investment.

Bibliography

Abel, S. J. and I. A. Boutle (2012). "An improved representation of the raindrop size distribution for single-moment microphysics schemes". *Quarterly Journal of the Royal Meteorological Society* 138.669, pp. 2151–2162. DOI: https://doi.org/10.1002/qj.1949 (cit. on pp. 35, 78).

"Chapter 6 - Vertical structure of the moist atmosphere" (2020). In: *Thermal Physics of the Atmosphere*. Ed. by M. H. P. Ambaum. Developments in Weather and Climate Science Series. Elsevier, pp. 115–132 (cit. on p. 4).

Andsager, K., K. V. Beard, and N. F. Laird (1999). "Laboratory Measurements of Axis Ratios for Large Raindrops". *Journal of the Atmospheric Sciences* 56.15, pp. 2673–2683. DOI: 10.1175/1520-0469(1999)056<2673:LMOARF>2.0.CO;2 (cit. on pp. 83, 84).

Aydin, K., T. A. Seliga, and V. Balaji (1986). "Remote sensing of hail with a dual linear polarization radar." *Journal of Climate and Applied Meteorology* 25.10, pp. 1475–1484. DOI: 10.1175/1520-0450(1986)025<1475:RSOHWA>2.0.CO;2 (cit. on pp. 44, 68, 70).

Balakrishnan, N. and D. S. Zrnić (1990). "Estimation of Rain and Hail Rates in Mixed-Phase Precipitation". *Journal of Atmospheric Sciences* 47.5, pp. 565–583. DOI: 10.1175/1520-0469(1990)047<0565:EORAHR>2.0.CO;2 (cit. on p. 11).

Beard, K. V. (1976). "Terminal Velocity and Shape of Cloud and Precipitation Drops Aloft". *Journal of Atmospheric Sciences* 33.5, pp. 851–864. DOI: https://doi.org/10.1175/1520-0469(1976)033<0851:TVASOC>2.0.CO;2 (cit. on p. 104).

Beard, K. V. and A. R. Jameson (1983). "Raindrop Canting". *Journal of Atmospheric Sciences* 40.2, pp. 448–454. DOI: https://doi.org/10.1175/1520-0469(1983)040<0448:RC>2.0.CO;2 (cit. on p. 84).

Bennett, L. J. et al. (2006). "A review of the initiation of precipitating convection in the United Kingdom". *Quarterly Journal of the Royal Meteorological Society* 132.617, pp. 1001–1020. DOI: https://doi.org/10.1256/qj.05.54 (cit. on p. 4).

Best, M. J. et al. (2011). "The Joint UK Land Environment Simulator (JULES), model description - Part 1: Energy and water fluxes". *Geoscientific Model Development* 4.3, pp. 677–699. DOI: 10.5194/gmd-4-677-2011 (cit. on p. 25).

Bigg, E. K. (1953). "The Supercooling of Water". *Proceedings of the Physical Society. Section B* 66.8, p. 688. DOI: 10.1088/0370-1301/66/8/309 (cit. on pp. 93, 111, 124).

Bousquet, O. and P. Tabary (2014). "Development of a nationwide real-time 3-D wind and reflectivity radar composite in France". *Quarterly Journal of the Royal Meteorological*

Society 140.679, pp. 611–625. DOI: https://doi.org/10.1002/qj.2163 (cit. on p. 21).

Boutle, I. A., J. E. J. Eyre, and A. P. Lock (2014a). "Seamless Stratocumulus Simulation across the Turbulent Gray Zone". *Monthly Weather Review* 142.4, pp. 1655–1668. DOI: https://doi.org/10.1175/MWR-D-13-00229.1 (cit. on p. 25).

Boutle, I. A. et al. (2014b). "Spatial variability of liquid cloud and rain: observations and microphysical effects". *Quarterly Journal of the Royal Meteorological Society* 140.679, pp. 583–594. DOI: https://doi.org/10.1002/qj.2140 (cit. on pp. 31, 32).

Brandes, E. A. et al. (1995). "A Study of Thunderstorm Microphysics with Multiparameter Radar and Aircraft Observations". *Monthly Weather Review* 123.11, pp. 3129–3143. DOI: 10.1175/1520-0493(1995)123<3129:asotmw>2.0.co;2 (cit. on pp. 12, 50).

Brandes, E. A., G. Zhang, and J. Vivekanandan (2002). "Experiments in Rainfall Estimation with a Polarimetric Radar in a Subtropical Environment". *Journal of Applied Meteorology* 41.6, pp. 674–685. DOI: https://doi.org/10.1175/1520-0450(2002)041<0674:EIREWA>2.0.CO;2 (cit. on pp. 82, 83).

Bringi, V. N., D. A. Burrows, and S. M. Menon (1991). "Multiparameter Radar and Aircraft Study of Raindrop Spectral Evolution in Warm-based Clouds". *Journal of Applied Meteorology and Climatology* 30.6, pp. 853–880. DOI: 10.1175/1520-0450(1991)030<0853:MRAASO>2.0.CO;2 (cit. on pp. 11, 12).

Bringi, V. N. et al. (1996). "Dual multiparameter radar observations of intense convective storms: The 24 June 1992 case study". *Meteorology and Atmospheric Physics* 59.1, pp. 3–31. DOI: 10.1007/BF01031999 (cit. on p. 12).

Bringi, V. N. et al. (1997). "Evolution of a Florida Thunderstorm during the Convection and Precipitation/Electrification Experiment: The Case of 9 August 1991". *Monthly Weather Review* 125.9, pp. 2131–2160. DOI: 10.1175/1520-0493(1997)125<2131:EOAFTD>2.0.CO;2 (cit. on p. 12).

Broeke, M. S. V. D. (2017). "Polarimetric Radar Metrics Related to Tornado Life Cycles and Intensity in Supercell Storms". *Monthly Weather Review* 145.9, pp. 3671–3686. DOI: 10.1175/MWR-D-16-0453.1 (cit. on p. 13).

Bruning, E. C. et al. (2007). "Electrical and Polarimetric Radar Observations of a Multicell Storm in TELEX". *Monthly Weather Review* 135.7, pp. 2525–2544. DOI: 10.1175/MWR3421.1 (cit. on p. 12).

Brunkow, D. (2008). "Measurements and inferences of raindrop canting angles". English. *Electronics Letters* 44 (24), 1425–1426(1) (cit. on p. 84).

Carey, L. D. and S. A. Rutledge (2000). "The Relationship between Precipitation and Lightning in Tropical Island Convection: A C-Band Polarimetric Radar Study". *Monthly Weather Review* 128.8, pp. 2687–2710. DOI: 10.1175/1520-0493(2000)128<2687:TRBPAL>2.0.CO;2 (cit. on p. 12).

Carlin, J. T. et al. (2017). "Assimilation of ZDR Columns for Improving the Spinup and Forecast of Convective Storms in Storm-Scale Models: Proof-of-Concept Experiments".

Monthly Weather Review 145.12, pp. 5033–5057. DOI: 10.1175/MWR-D-17-0103.1 (cit. on p. 50).

Caylor, I. J. and A. J. Illingworth (1987). "Radar Observations and Modelling of Warm Rain Initiation". *Quarterly Journal of the Royal Meteorological Society* 113.478, pp. 1171–1191. DOI: https://doi.org/10.1002/qj.49711347806 (cit. on p. 11).

Charney, J. G. and N. A. Phillips (1953). "NUMERICAL INTEGRATION OF THE QUASI-GEOSTROPHIC EQUATIONS FOR BAROTROPIC AND SIMPLE BAROCLINIC FLOWS". *Journal of Atmospheric Sciences* 10.2, pp. 71–99. DOI: https://doi.org/10.1175/1520-0469(1953)010<0071:NIOTQG>2.0.CO;2 (cit. on p. 25).

Chisholm, A. J. (1973). "Alberta Hailstorms Part I: Radar Case Studies and Airflow Models". In: *Alberta Hailstorms*. Boston, MA: American Meteorological Society, pp. 1–36. DOI: 10.1007/978-1-935704-32-4_1 (cit. on p. 13).

Cifelli, R. et al. (2002). "Radar observations of the kinematic, microphysical, and precipitation characteristics of two MCSs in TRMM LBA". *Journal of Geophysical Research: Atmospheres* 107.D20, LBA 44-1-LBA 44–16. DOI: https://doi.org/10.1029/2000JD000264 (cit. on p. 12).

Conway, J. W. and D. S. Zrnić (1993). "A Study of Embryo Production and Hail Growth Using Dual-Doppler and Multiparameter Radars". *Monthly Weather Review* 121.9, pp. 2511–2528. DOI: 10.1175/1520-0493(1993)121<2511:ASOEPA>2.0.CO;2 (cit. on p. 12).

Cotton, W. R. (1972). "Numerical Simulation of Precipitation Development in Supercooled Cumuli—Part II". *Monthly Weather Review* 100.11, pp. 764–784. DOI: 10.1175/1520-0493(1972)100<0764:NSOPDI>2.3.CO;2 (cit. on p. 124).

Cotton, W. R., G. Bryan, and S. C. van den Heever (2011). "Chapter 8 - Cumulonimbus Clouds and Severe Convective Storms". In: *Storm and Cloud Dynamics*. Ed. by W. Cotton, G. Bryan, and S. van den Heever. Vol. 99. International Geophysics. Academic Press, pp. 315–454. DOI: https://doi.org/10.1016/S0074-6142(10)09914-6 (cit. on pp. 3, 4, 6, 7).

Cullen, M. J. et al. (1997). "An Overview of Numerical Methods for the Next Generation U.K. NWP and Climate Model". *Atmosphere-Ocean* 35.sup1, pp. 425–444. DOI: 10.1080/07055900.1997.9687359 (cit. on p. 24).

Davies, T. et al. (2005). "A new dynamical core for the Met Office's global and regional modelling of the atmosphere". *Quarterly Journal of the Royal Meteorological Society* 131.608, pp. 1759–1782. DOI: https://doi.org/10.1256/qj.04.101 (cit. on p. 24).

Debye, P. (1909). "Der Lichtdruk auf Kugeln von beliebigem Material". *Annalen der Physik* 30, pp. 57–136 (cit. on p. 81).

Depue, T. K., P. C. Kennedy, and S. A. Rutledge (2007). "Performance of the hail differential reflectivity (HDR) polarimetric radar hail indicator". *Journal of Applied Meteorology and Climatology* 46.8, pp. 1290–1301. DOI: 10.1175/JAM2529.1 (cit. on p. 68).

Dotzek, N. et al. (2009). "Overview of ESSL's severe convective storms research using the European Severe Weather Database ESWD". *Atmospheric Research* 93.1-3, pp. 575–586. DOI: 10.1016/j.atmosres.2008.10.020 (cit. on pp. 53, 59).

Doviak, R. J. and D. S. Zrnić (1993). "2 - Electromagnetic Waves and Propagation". In: *Doppler Radar and Weather Observations (Second Edition)*. Ed. by R. J. Doviak and D. S. Zrnić. Second Edition. San Diego: Academic Press, pp. 10–29. DOI: https://doi.org/10.1016/B978-0-12-221422-6.50007-3 (cit. on p. 39).

Edwards, J. M. and A. Slingo (1996). "Studies with a flexible new radiation code. I: Choosing a configuration for a large-scale model". *Quarterly Journal of the Royal Meteorological Society* 122.531, pp. 689–719. DOI: https://doi.org/10.1002/qj.49712253107 (cit. on p. 25).

Evaristo, R. et al. (2010). "Polarimetric signatures and hydrometeor classification of West African squall lines". *Quarterly Journal of the Royal Meteorological Society* 136.S1, pp. 272–288. DOI: https://doi.org/10.1002/qj.561 (cit. on p. 12).

Fabry, F. (2015). "The added value of dual polarization". In: *Radar Meteorology: Principles and Practice*. Cambridge University Press, pp. 92–114 (cit. on p. 9).

Field, P. et al. (2023). "Implementation of a double moment cloud microphysics scheme in the UK met office regional numerical weather prediction model". *Quarterly Journal of the Royal Meteorological Society* 149.752, pp. 703–739. DOI: https://doi.org/10.1002/qj.4414 (cit. on pp. 29, 32, 33, 79, 88).

Gans, R. (1912). "Über die Form ultramikroskopischer Goldteilehen". *Annalen der Physik* 37, pp. 881–900 (cit. on p. 81).

Gaussiat, N. (2008). *Comparisons of radar reflectivities with synthesised observations from NWP model output*. Tech. rep. (cit. on p. 77).

Goddard, J., M. Thurai, and J. Eastment (1994). "The Chilbolton Advanced Meteorological Radar: a tool for multidisciplinary atmospheric research". *Electronics & Communication Engineering Journal* 6.2, pp. 77–86. DOI: 10.1049/ecej:19940205 (cit. on p. 24).

Goodman, S. J. et al. (1988). "Lightning and precipitation history of a microburst-producing storm". *Geophysical Research Letters* 15.11, pp. 1185–1188. DOI: https://doi.org/10.1029/GL015i011p01185 (cit. on p. 12).

Grabowski, W. W. (2019). "Separating physical impacts from natural variability using piggybacking technique". *Advances in Geosciences* 49, pp. 105–111 (cit. on p. 124).

Green, A. W. (1975). "An Approximation for the Shapes of Large Raindrops". *Journal of Applied Meteorology and Climatology* 14.8, pp. 1578–1583. DOI: https://doi.org/10.1175/1520-0450(1975)014<1578:AAFTSO>2.0.CO;2 (cit. on pp. 82, 83).

Gregory, D. and P. R. Rowntree (1990). "A Mass Flux Convection Scheme with Representation of Cloud Ensemble Characteristics and Stability-Dependent Closure". *Monthly Weather Review* 118.7, pp. 1483–1506. DOI: https://doi.org/10.1175/1520-0493(1990)118<1483:AMFCSW>2.0.CO;2 (cit. on p. 26).

Groenemeijer, P., A.-J. Punkka, and J. Teittinen (2005). *Forecasting Severe Convective Storms* (cit. on p. 4).

Hall, M. P. M. et al. (1980). "Rain drop sizes and rainfall rate measured by dual-polarization radar". *Nature* 285.5762, pp. 195–198. DOI: 10.1038/285195a0 (cit. on p. 10).

Hall, M. P. M., J. W. F. Goddard, and S. M. Cherry (1984). "Identification of hydrometeors and other targets by dual-polarization radar". *Radio Sci.* 19.1, pp. 132–140. DOI: 10.1029/RS019i001p00132 (cit. on pp. 10, 11).

Hanley, K. et al. (2019). "Modifications to the representation of subgrid mixing in kilometre-scale versions of the Unified Model". *Quarterly Journal of the Royal Meteorological Society* 145.725, pp. 3361–3375. DOI: https://doi.org/10.1002/qj.3624 (cit. on p. 26).

Harrison, D. L., R. W. Scovell, and M. Kitchen (2009). "High-resolution precipitation estimates for hydrological uses". *Proceedings of the Institution of Civil Engineers - Water Management* 162.2, pp. 125–135. DOI: 10.1680/wama.2009.162.2.125 (cit. on p. 51).

Hendry, A., Y. M. M. Antar, and G. C. McCormick (1987). "On the relationship between the degree of preferred orientation in precipitation and dual-polarization radar echo characteristics". *Radio Science* 22.1, pp. 37–50. DOI: https://doi.org/10.1029/RS022i001p00037 (cit. on p. 85).

Herzegh, P. H. and A. R. Jameson (1992). "Observing precipitation through dual-polarization radar measurements". *Bulletin - American Meteorological Society* 73.9, pp. 1365–1374. DOI: 10.1175/1520-0477(1992)073<1365:OPTDPR>2.0.CO;2 (cit. on pp. 12, 51).

Hogan, R. J. et al. (2002). "Properties of embedded convection in warm-frontal mixed-phase cloud from aircraft and polarimetric radar". *Quarterly Journal of the Royal Meteorological Society* 128.580, pp. 451–476. DOI: 10.1256/003590002321042054 (cit. on p. 50).

Hogan, R. J. et al. (2003). "Characteristics of mixed-phase clouds. I: Lidar, radar and aircraft observations from CLARE'98". *Quarterly Journal of the Royal Meteorological Society* 129.592, pp. 2089–2116. DOI: 10.1256/rj.01.208 (cit. on p. 50).

Hogan, R. J. (2007). "A Variational Scheme for Retrieving Rainfall Rate and Hail Reflectivity Fraction from Polarization Radar". *Journal of Applied Meteorology and Climatology* 46.10, pp. 1544–1564. DOI: 10.1175/JAM2550.1 (cit. on p. 123).

Höller, H. et al. (1994). "Life Cycle and Precipitation Formation in a Hybrid-Type Hailstorm Revealed by Polarimetric and Doppler Radar Measurements". *Journal of Atmospheric Sciences* 51.17, pp. 2500–2522. DOI: 10.1175/1520-0469(1994)051<2500:LCAPFI>2.0.CO;2 (cit. on p. 12).

Homeyer, C. R. and M. R. Kumjian (2015). "Microphysical Characteristics of Overshooting Convection from Polarimetric Radar Observations". *Journal of the Atmospheric Sciences* 72.2, pp. 870–891. DOI: 10.1175/JAS-D-13-0388.1 (cit. on pp. 12, 13).

Hubbert, J. et al. (1998). “CSU-CHILL Polarimetric Radar Measurements from a Severe Hail Storm in Eastern Colorado”. *Journal of Applied Meteorology* 37.8, pp. 749–775. DOI: 10.1175/1520-0450(1998)037<0749:CCPRMF>2.0.CO;2 (cit. on p. 12).

Illingworth, A. J., J. W. F. Goddard, and S. M. Cherry (1987). “Polarization radar studies of precipitation development in convective storms”. *Quarterly Journal of the Royal Meteorological Society* 113.476, pp. 469–489. DOI: https://doi.org/10.1002/qj.49711347604 (cit. on pp. 11, 12, 50, 76).

Illingworth, A. J. (1988). “The formation of rain in convective clouds”. *Nature* 336.6201, pp. 754–756. DOI: 10.1038/336754a0 (cit. on p. 11).

Jameson, A. R., M. J. Murphy, and E. P. Krider (1996). “Multiple-Parameter Radar Observations of Isolated Florida Thunderstorms during the Onset of Electrification”. *Journal of Applied Meteorology and Climatology* 35.3, pp. 343–354. DOI: 10.1175/1520-0450(1996)035<0343:MPROOI>2.0.CO;2 (cit. on p. 12).

Jung, Y., M. Xue, and G. Zhang (2010). “Simulations of Polarimetric Radar Signatures of a Supercell Storm Using a Two-Moment Bulk Microphysics Scheme”. *Journal of Applied Meteorology and Climatology* 49.1, pp. 146–163. DOI: 10.1175/2009JAMC2178.1 (cit. on p. 15).

Kaltenboeck, R. and A. V. Ryzhkov (2013). “Comparison of polarimetric signatures of hail at S and C bands for different hail sizes”. *Atmospheric Research* 123. 6th European Conference on Severe Storms 2011. Palma de Mallorca, Spain, pp. 323–336. DOI: https://doi.org/10.1016/j.atmosres.2012.05.013 (cit. on p. 12).

Kennedy, P. C. et al. (2001). “Polarimetric radar observations of hail formation”. *Journal of Applied Meteorology* 40.8, pp. 1347–1366. DOI: 10.1175/1520-0450(2001)040<1347:PROOHF>2.0.CO;2 (cit. on pp. 12, 56).

Khairoutdinov, M. and Y. Kogan (2000). “A New Cloud Physics Parameterization in a Large-Eddy Simulation Model of Marine Stratocumulus”. *Monthly Weather Review* 128.1, pp. 229–243. DOI: https://doi.org/10.1175/1520-0493(2000)128<0229:ANCPPI>2.0.CO;2 (cit. on pp. 31, 32).

Knight, C. A. (2006). “Very Early Formation of Big, Liquid Drops Revealed by ZDR in Continental Cumulus”. *Journal of the Atmospheric Sciences* 63.7, pp. 1939–1953. DOI: 10.1175/JAS3721.1 (cit. on pp. 12, 64).

Knight, C. A., L. J. Miller, and W. D. Hall (2004). “Deep Convection and “First Echoes” within Anvil Precipitation”. *Monthly Weather Review* 132.7, pp. 1877–1890. DOI: 10.1175/1520-0493(2004)132<1877:DCAFEW>2.0.CO;2 (cit. on p. 12).

Knight, C. A., J. Vivekanandan, and S. G. Lasher-Trapp (2002). “First Radar Echoes and the Early ZDR History of Florida Cumulus”. *Journal of the Atmospheric Sciences* 59.9, pp. 1454–1472. DOI: 10.1175/1520-0469(2002)059<1454:FREATE>2.0.CO;2 (cit. on p. 12).

Krause, J. and V. Klaus (2024). “Identifying ZDR Columns in Radar Data with the Hotspot Technique”. *Weather and Forecasting*. DOI: 10.1175/WAF-D-23-0146.1 (cit. on p. 121).

Kumjian, M. R. (2013). "Principles and applications of dual-polarization weather radar. Part II: Warm- and cold-season applications". *Journal of Operational Meteorology* 1.20, pp. 243–264. DOI: 10.15191/nwajom.2013.0120 (cit. on pp. 10, 50).

Kumjian, M. R. and A. V. Ryzhkov (2008). "Polarimetric signatures in supercell thunderstorms". *Journal of Applied Meteorology and Climatology* 47.7, pp. 1940–1961. DOI: 10.1175/2007JAMC1874.1 (cit. on pp. 12, 50).

Kumjian, M. R. et al. (2014). "The anatomy and physics of ZDR columns: Investigating a polarimetric radar signature with a spectral bin microphysical model". *Journal of Applied Meteorology and Climatology* 53.7, pp. 1820–1843. DOI: 10.1175/JAMC-D-13-0354.1 (cit. on pp. 10, 15, 50, 51, 62, 64, 111).

Kumjian, M. R. et al. (2010). "Rapid-Scan Super-Resolution Observations of a Cyclic Supercell with a Dual-Polarization WSR-88D". *Monthly Weather Review* 138.10, pp. 3762–3786. DOI: 10.1175/2010MWR3322.1 (cit. on p. 12).

Kuster, C. M. et al. (2019). "Rapid-update radar observations of ZDR column depth and its use in the warning decision process". *Weather and Forecasting* 34.4, pp. 1173–1188. DOI: 10.1175/WAF-D-19-0024.1 (cit. on pp. 13, 51).

Kuster, C. M. et al. (2020). "Using ZDR Columns in Forecaster Conceptual Models and Warning Decision Making". *Weather and Forecasting*, pp. 1–43. DOI: 10.1175/WAF-D-20-0083.1 (cit. on pp. 13, 14, 51, 62, 71).

Kuster, C. M., P. L. Heinselman, and T. J. Schuur (2016). "Rapid-Update Radar Observations of Downbursts Occurring within an Intense Multicell Thunderstorm on 14 June 2011". *Weather and Forecasting* 31.3, pp. 827–851. DOI: 10.1175/WAF-D-15-0081.1 (cit. on p. 12).

Leinonen, J. (2014). "High-level interface to T-matrix scattering calculations: architecture, capabilities and limitations". *Opt. Express* 22.2, pp. 1655–1660. DOI: 10.1364/OE.22.001655 (cit. on p. 81).

Lock, A. P. et al. (2000). "A New Boundary Layer Mixing Scheme. Part I: Scheme Description and Single-Column Model Tests". *Monthly Weather Review* 128.9, pp. 3187–3199. DOI: https://doi.org/10.1175/1520-0493(2000)128<3187:ANBLMS>2.0.CO;2 (cit. on p. 25).

Loney, M. L. et al. (2002). "Enhanced Polarimetric Radar Signatures above the Melting Level in a Supercell Storm". *Journal of Applied Meteorology* 41.12, pp. 1179–1194. DOI: 10.1175/1520-0450(2002)041<1179:EPRSAT>2.0.CO;2 (cit. on p. 12).

Lorenz, L. (1890). "Lysbevægelsen i og uden for en af plane Lysbølger belyst Kugle". *Det Kongelige Danske Videnskabernes Selskabs Skrifter* 6.6 (cit. on p. 81).

MacGorman, D. R. et al. (2008). "TELEX The Thunderstorm Electrification and Lightning Experiment". *Bulletin of the American Meteorological Society* 89.7, pp. 997–1014. DOI: 10.1175/2007BAMS2352.1 (cit. on p. 12).

Manners, J. et al. (2018). *Socrates technical guide suite of community radiative transfer codes based on edwards and slingo*. Tech. rep. (cit. on p. 25).

Marshall, J. S. and W. M. K. Palmer (1948). "THE DISTRIBUTION OF RAINDROPS WITH SIZE". *Journal of Atmospheric Sciences* 5.4, pp. 165–166. DOI: https://doi.org/10.1175/1520-0469(1948)005<0165:TDORWS>2.0.CO;2 (cit. on pp. 53, 78).

Martin, G. M., D. W. Johnson, and A. Spice (1994). "The Measurement and Parameterization of Effective Radius of Droplets in Warm Stratocumulus Clouds". *Journal of Atmospheric Sciences* 51.13, pp. 1823–1842. DOI: https://doi.org/10.1175/1520-0469(1994)051<1823:TMAPOE>2.0.CO;2 (cit. on p. 31).

Mattos, E. V. et al. (2016). "Polarimetric radar characteristics of storms with and without lightning activity". *Journal of Geophysical Research: Atmospheres* 121.23, pp. 14, 201–14, 220. DOI: https://doi.org/10.1002/2016JD025142 (cit. on p. 12).

Mattos, E. V. et al. (2017). "Electrification life cycle of incipient thunderstorms". *Journal of Geophysical Research: Atmospheres* 122.8, pp. 4670–4697. DOI: https://doi.org/10.1002/2016JD025772 (cit. on p. 12).

May, P. T. et al. (2001). "A Comparison between Polarimetric Radar and Wind Profiler Observations of Precipitation in Tropical Showers". *Journal of Applied Meteorology* 40.10, pp. 1702–1717. DOI: 10.1175/1520-0450(2001)040<1702:ACBPRA>2.0.CO;2 (cit. on p. 12).

McBeath, K., P. Field, and R. J. Cotton (2014). "Using operational weather radar to assess high-resolution numerical weather prediction over the British Isles for a cold air outbreak case-study". *Quarterly Journal of the Royal Meteorological Society* 140.678, pp. 225–239. DOI: https://doi.org/10.1002/qj.2123 (cit. on p. 77).

McConnell, E. (2021). *Kent weather: Thunderstorms and flooding hit parts of county* (cit. on p. 59).

Meischner, P. F. et al. (1991). "A Squall Line in Southern Germany: Kinematics and Precipitation Formation as Deduced by Advanced Polarimetric and Doppler Radar Measurements". *Monthly Weather Review* 119.3, pp. 678–701. DOI: 10.1175/1520-0493(1991)119<0678:ASLISG>2.0.CO;2 (cit. on p. 11).

Met Office (2016). *NWP-Global: Operational Numerical Weather Prediction (NWP) output from the UK Met Office Global Atmospheric Unified Model (UM)*. Accessed: 2023-09-26 (cit. on p. 26).

Mie, G. (1908). "Beiträge zur Optik trüber Medien, speziell kolloidaler Metallösungen". *Annalen der Physik* 25, pp. 377–445 (cit. on p. 81).

Mishchenko, M. I. (2000). "Calculation of the amplitude matrix for a nonspherical particle in a fixed orientation". *Appl. Opt.* 39.6, pp. 1026–1031. DOI: 10.1364/AO.39.001026 (cit. on p. 81).

Mittermaier, M. P. and A. J. Illingworth (2003). "Comparison of model-derived and radar-observed freezing-level heights: Implications for vertical reflectivity profile-correction schemes". *Quarterly Journal of the Royal Meteorological Society* 129.587, pp. 83–95. DOI: https://doi.org/10.1256/qj.02.19 (cit. on pp. 26, 58).

National Weather Service (2017). *Severe Thunderstorms Definitions* (cit. on pp. 3, 53).

Ordnance Survey (2018). *A Guide to Coordinate Systems in Great Britain*. Accessed: 16-1-2024 (cit. on p. 39).

Otsu, N. (1979). "A Threshold Selection Method from Gray-Level Histograms". *IEEE Transactions on Systems, Man, and Cybernetics* 9.1, pp. 62–66. DOI: 10.1109/TSMC.1979.4310076 (cit. on p. 56).

Petty, G. W. (2006). "Scattering and Absorption By Particles". In: *A first course in atmospheric radiation*. Sundog Pub., pp. 343–386 (cit. on p. 76).

Picca, J., M. R. Kumjian, and A. V. Ryzhkov (2010). "ZDR Columns As a Predictive Tool for Hail Growth". In: *25th Conference on Severe Local Storms*. Denver, Colorado: American Meteorological Society, p. 11.3 (cit. on pp. 13, 64).

Plummer, D. M. et al. (2018). "Radar-Derived Structural and Precipitation Characteristics of ZDR Columns within Warm-Season Convection over the United Kingdom". *Journal of Applied Meteorology and Climatology* 57.11, pp. 2485–2505. DOI: 10.1175/JAMC-D-17-0134.1 (cit. on pp. 10, 12, 23, 45, 52, 58, 59, 71).

Pruppacher, H. R. and K. V. Beard (1970). "A wind tunnel investigation of the internal circulation and shape of water drops falling at terminal velocity in air". *Quarterly Journal of the Royal Meteorological Society* 96.408, pp. 247–256. DOI: https://doi.org/10.1002/qj.49709640807 (cit. on pp. 44, 76, 81).

Raghavan, R. and V. Chandrasekar (1994). "Multiparameter Radar Study of Rainfall: Potential Application to Area Time Integral Studies". *Journal of Applied Meteorology and Climatology* 33.12, pp. 1636–1645. DOI: 10.1175/1520-0450(1994)033<1636:MRSORP>2.0.CO;2 (cit. on p. 12).

Rowe, A. K., S. A. Rutledge, and T. J. Lang (2012). "Investigation of Microphysical Processes Occurring in Organized Convection during NAME". *Monthly Weather Review* 140.7, pp. 2168–2187. DOI: 10.1175/MWR-D-11-00124.1 (cit. on p. 12).

Ryzhkov, A. V. (2007). "The Impact of Beam Broadening on the Quality of Radar Polarimetric Data". *Journal of Atmospheric and Oceanic Technology* 24.5, pp. 729–744. DOI: https://doi.org/10.1175/JTECH2003.1 (cit. on pp. 45, 95).

Ryzhkov, A. V., V. B. Zhuravlyov, and N. A. Rybakova (1994). "Preliminary Results of X-Band Polarization Radar Studies of Clouds and Precipitation". *Journal of Atmospheric and Oceanic Technology* 11.1, pp. 132–139. DOI: 10.1175/1520-0426(1994)011<0132:PROXBP>2.0.CO;2 (cit. on p. 12).

Ryzhkov, A. V. and D. Zrnic (2005). "Comparative analysis and operational implications". In: *32nd Conference on Radar Meteorology*. American Meteorological Society, 9R.3 (cit. on p. 45).

Ryzhkov, A. V. et al. (2005). "Polarimetric Tornado Detection". *Journal of Applied Meteorology* 44.5, pp. 557–570. DOI: 10.1175/JAM2235.1 (cit. on pp. 12, 119).

Ryzhkov, A. V. et al. (2011). "Polarimetric Radar Observation Operator for a Cloud Model with Spectral Microphysics". *Journal of Applied Meteorology and Climatology* 50.4, pp. 873–894. DOI: https://doi.org/10.1175/2010JAMC2363.1 (cit. on p. 13).

Al-Sakka, H. et al. (2013). "A New Fuzzy Logic Hydrometeor Classification Scheme Applied to the French X-, C-, and S-Band Polarimetric Radars". *Journal of Applied Meteorology and Climatology* 52.10, pp. 2328–2344. DOI: https://doi.org/10.1175/JAMC-D-12-0236.1 (cit. on p. 21).

Scharfenberg, K. A. et al. (2005). "The Joint Polarization Experiment: Polarimetric Radar in Forecasting and Warning Decision Making". *Weather and Forecasting* 20.5, pp. 775–788. DOI: 10.1175/WAF881.1 (cit. on pp. 12, 13).

Scovell, R. and H. al-Sakka (2016). "A Point Cloud Method for Retrieval of High-Resolution 3D Gridded Reflectivity from Weather Radar Networks for Air Traffic Management". *Journal of Atmospheric and Oceanic Technology* 33.3, pp. 461–479. DOI: https://doi.org/10.1175/JTECH-D-15-0051.1 (cit. on pp. 8, 21, 51, 56).

Seliga, T. A. and V. N. Bringi (1976). "Potential Use of Radar Differential Reflectivity Measurements at Orthogonal Polarizations for Measuring Precipitation". *Journal of Applied Meteorology and Climatology* 15.1, pp. 69–76. DOI: https://doi.org/10.1175/1520-0450(1976)015<0069:PUORDR>2.0.CO;2 (cit. on pp. 9, 81, 82).

Seroka, G. N., R. E. Orville, and C. Schumacher (2012). "Radar nowcasting of total lightning over the Kennedy space center". *Weather and Forecasting* 27.1, pp. 189–204. DOI: 10.1175/WAF-D-11-00035.1 (cit. on p. 68).

Shrestha, P. et al. (2022). "Evaluation of modelled summertime convective storms using polarimetric radar observations". *Atmospheric Chemistry and Physics* 22.11, pp. 7593–7618. DOI: 10.5194/acp-22-7593-2022 (cit. on p. 16).

Shupyatsky, A. B. et al. (1990). "Use of polarization measurements in Cb for the analysis of their stage of development (in Russian)". *Meteor. Hydrol.* 12, pp. 57–66 (cit. on p. 11).

Skamarock, W. C. (2004). "Evaluating Mesoscale NWP Models Using Kinetic Energy Spectra". *Monthly Weather Review* 132.12, pp. 3019–3032. DOI: 10.1175/MWR2830.1 (cit. on p. 125).

Smith, P. L. (n.d.). "Lyrics composed on a train from Zurich to Locarno following 22nd Conf. on Radar Meteorology." ().

Smith, P. L. et al. (1999). "Observations of Mixed-Phase Precipitation within a CaPE Thunderstorm". *Journal of Applied Meteorology* 38.2, pp. 145–155. DOI: 10.1175/1520-0450(1999)038<0145:OOMPPW>2.0.CO;2 (cit. on p. 12).

Smith, R. N. B. (1990). "A scheme for predicting layer clouds and their water content in a general circulation model". *Quarterly Journal of the Royal Meteorological Society* 116.492, pp. 435–460. DOI: https://doi.org/10.1002/qj.49711649210 (cit. on p. 28).

Smyth, T. J. and A. J. Illingworth (1998). "Correction for attenuation of radar reflectivity using polarization data". *Quarterly Journal of the Royal Meteorological Society* 124.551, pp. 2393–2415. DOI: https://doi.org/10.1002/qj.49712455111 (cit. on p. 122).

Snyder, J. C. et al. (2010). *The structure and time evolution of polarimetric signatures in severe convective storms based on high-resolution numerical simulations and data from a mobile, dual-polarized, X-band Doppler radar* (cit. on p. 15).

Snyder, J. C. et al. (2015). "A ZDR column detection algorithm to examine convective storm updrafts". *Weather and Forecasting* 30.6, pp. 1819–1844. DOI: 10.1175/WAF-D-15-0068.1 (cit. on pp. 10, 13, 50, 58, 62, 71).

Snyder, J. C. et al. (2013). "Observations of Polarimetric Signatures in Supercells by an X-Band Mobile Doppler Radar". *Monthly Weather Review* 141.1, pp. 3–29. DOI: 10.1175/MWR-D-12-00068.1 (cit. on p. 13).

Stein, T. H. M. et al. (2015). "The DYMECS Project: A Statistical Approach for the Evaluation of Convective Storms in High-Resolution NWP Models". *Bulletin of the American Meteorological Society* 96.6, pp. 939–951. DOI: 10.1175/BAMS-D-13-00279.1 (cit. on pp. 16, 56).

Stein, T. H. M. et al. (2020). "The potential use of operational radar network data to evaluate the representation of convective storms in NWP models". *Quarterly Journal of the Royal Meteorological Society* 146.730, pp. 2315–2331. DOI: https://doi.org/10.1002/qj.3793 (cit. on pp. 22, 23, 37, 52, 62, 71).

Stein, T. H. M. et al. (2014). "The Three-Dimensional Morphology of Simulated and Observed Convective Storms over Southern England". *Monthly Weather Review* 142.9, pp. 3264–3283. DOI: https://doi.org/10.1175/MWR-D-13-00372.1 (cit. on p. 77).

Suri, D. and P. A. Davies (2021). "A decade of impact-based NSWWS warnings at the Met Office". *The European Forecaster* 26, pp. 30–36 (cit. on p. 3).

Tanamachi, R. L. et al. (2012). "Mobile, X-band, Polarimetric Doppler Radar Observations of the 4 May 2007 Greensburg, Kansas, Tornadic Supercell". *Monthly Weather Review* 140.7, pp. 2103–2125. DOI: 10.1175/MWR-D-11-00142.1 (cit. on p. 12).

Tessendorf, S. A. et al. (2005). "The 29 June 2000 Supercell Observed during STEPS. Part I: Kinematics and Microphysics". *Journal of the Atmospheric Sciences* 62.12, pp. 4127–4150. DOI: 10.1175/JAS3585.1 (cit. on p. 12).

Thurai, M. et al. (2007). "Drop Shapes, Model Comparisons, and Calculations of Polarimetric Radar Parameters in Rain". *Journal of Atmospheric and Oceanic Technology* 24.6, pp. 1019–1032. DOI: https://doi.org/10.1175/JTECH2051.1 (cit. on pp. 83–86, 91, 107, 122).

Tong, H. et al. (1998). "Multiparameter Radar Observations of Time Evolution of Convective Storms: Evaluation of Water Budgets and Latent Heating Rates". *Journal of Atmospheric and Oceanic Technology* 15.5, pp. 1097–1109. DOI: 10.1175/1520-0426(1998)015<1097:MROOTE>2.0.CO;2 (cit. on p. 12).

Turner, D. D., S. Kneifel, and M. P. Cadeddu (2016). "An Improved Liquid Water Absorption Model at Microwave Frequencies for Supercooled Liquid Water Clouds". *Journal of Atmospheric and Oceanic Technology* 33.1, pp. 33–44. DOI: 10.1175/JTECH-D-15-0074.1 (cit. on p. 81).

Tuttle, J. D. et al. (1989). "Multiparameter Radar Study of a Microburst: Comparison with Model Results". *Journal of Atmospheric Sciences* 46.5, pp. 601–620. DOI: 10.1175/1520-0469(1989)046<0601:MRSOAM>2.0.CO;2 (cit. on p. 11).

Vivekanandan, J. et al. (1990). "Microwave Radiative Transfer Studies Using Combined Multiparameter Radar and Radiometer Measurements during COHMEX". *Journal of Applied Meteorology and Climatology* 29.7, pp. 561–585. DOI: 10.1175/1520-0450(1990)029<0561:MRTSUC>2.0.CO;2 (cit. on p. 11).

Wakimoto, R. M. and V. N. Bringi (1988). "Dual-Polarization observations of Microbursts Associated with Intense Convection: The 20 July Storm during the MIST Project". *Monthly Weather Review* 116.8, pp. 1521–1539. DOI: 10.1175/1520-0493(1988)116<1521:DPOOMA>2.0.CO;2 (cit. on p. 11).

Warren, R. A. and A. Protat (2019). "Should Interpolation of Radar Reflectivity be Performed in Z or dBZ?" *Journal of Atmospheric and Oceanic Technology* 36.6, pp. 1143–1156. DOI: https://doi.org/10.1175/JTECH-D-18-0183.1 (cit. on p. 23).

Weisman, M. L. and J. B. Klemp (1982). "The Dependence of Numerically Simulated Convective Storms on Vertical Wind Shear and Buoyancy". *Monthly Weather Review* 110.6, pp. 504–520. DOI: 10.1175/1520-0493(1982)110<0504:TDONSC>2.0.CO;2 (cit. on p. 54).

Westbrook, C. D. et al. (2010). "Doppler lidar measurements of oriented planar ice crystals falling from supercooled and glaciated layer clouds". *Quarterly Journal of the Royal Meteorological Society* 136.646, pp. 260–276. DOI: 10.1002/qj.528 (cit. on p. 50).

Wilkinson, J. M. and R. Neal (2021). "Exploring relationships between weather patterns and observed lightning activity for Britain and Ireland". *Quarterly Journal of the Royal Meteorological Society* 147.738, pp. 2772–2795. DOI: 10.1002/qj.4099 (cit. on pp. 72, 121).

Williams, E. R. et al. (2011). "Dual polarization radar winter storm studies supporting development of NEXRAD-based aviation hazard products". In: *Proceedings of the 35th Conference on Radar Meteorology*. American Meteorological Society, P13.202 (cit. on p. 21).

Wilson, D. R. and S. P. Ballard (1999). "A microphysically based precipitation scheme for the UK meteorological office unified model". *Quarterly Journal of the Royal Meteorological Society* 125.557, pp. 1607–1636. DOI: https://doi.org/10.1002/qj.49712555707 (cit. on pp. 25, 81, 88).

Woodard, C. J. et al. (2012). "Operational utility of dual-polarization variables in lightning initiation forecasting". *Electron. J. Oper. Meteor.* 13, pp. 79–102 (cit. on p. 12).

Yuter, S. E. and R. A. Houze (1995). "Three-Dimensional Kinematic and Microphysical Evolution of Florida Cumulonimbus. Part II: Frequency Distributions of Vertical Velocity, Reflectivity, and Differential Reflectivity". *Monthly Weather Review* 123.7, pp. 1941–1963. DOI: https://doi.org/10.1175/1520-0493(1995)123<1941:TDKAME>2.0.CO;2 (cit. on pp. 12, 104).

Zeng, Z. et al. (2001). "Microphysics of the Rapid Development of Heavy Convective Precipitation". *Monthly Weather Review* 129.8, pp. 1882–1904. DOI: 10.1175/1520-0493(2001)129<1882:MOTRDO>2.0.CO;2 (cit. on p. 12).

Zhang, J., K. Howard, and J. J. Gourley (2005). "Constructing Three-Dimensional Multiple-Radar Reflectivity Mosaics: Examples of Convective Storms and Stratiform Rain Echoes". *Journal of Atmospheric and Oceanic Technology* 22.1, pp. 30–42. DOI: https://doi.org/10.1175/JTECH-1689.1 (cit. on pp. 23, 56).

Zhang, J. et al. (2011). "National Mosaic and Multi-Sensor QPE (NMQ) System: Description, Results, and Future Plans". *Bulletin of the American Meteorological Society* 92.10, pp. 1321–1338. DOI: https://doi.org/10.1175/2011BAMS-D-11-00047.1 (cit. on p. 21).